8-2007

# THE THERMOELECTRIC PROPERTIES INVESTIGATION OF $Ir_3Ge_7$ TYPED REPRESENTATIVES

Huqin Zhang
*Clemson University*, huqinz@clemson.edu

# THE THERMOELECTRIC PROPERTIES INVESTIGATION OF $Ir_3Ge_7$ TYPED REPRESENTATIVES

---

A Thesis
Presented to
the Graduate School of
Clemson University

---

In Partial Fulfillment
of the Requirements for the Degree
Master of Science
Physics

---

by
Huqin Zhang
August 2007

---

Accepted by:
Dr. Terry M. Tritt, Committee Chair
Dr. Apparao M. Rao
Dr. Chad E. Sosolik

# ABSTRACT

Energy conversion is employed to power generation utilizing the Seebeck effect or cooling utilizing the Peltier effect. Herein, we study several $Ir_3Ge_7$ typed semiconductor materials for potential thermoelectric energy conversion. $Mo_3Sb_7$, crystallizing in $Ir_3Ge_7$ type, can be rendered semiconducting by a partial Sb-Te substitution without noticeable structure changes, resulting in $Mo_3Sb_5Te_2$ with 55 valence electrons per formula unit. Meanwhile, large cubic voids in the $Mo_3Sb_5Te_2$ crystal structure provide the possibility of filling the voids with small cations to decrease the thermal conductivity by the so-called rattling effect. To verify this idea, the thermal and electrical transport properties of $Mo_3Sb_{5.4}Te_{1.6}$ and $Ni_{0.06}Mo_3Sb_{5.4}Te_{1.6}$ are studied. The material, $Nb_3Sb_2Te_5$, is isoelectronic with $Mo_3Sb_5Te_2$ and crystallizes in the $Ir_3Ge_7$ type like $Mo_3Sb_5Te_2$. Its thermoelectric properties are studied. $Re_3(GeAs)_7$ also crystallizes in the cubic $Ir_3Ge_7$ type and different doping levels can be achieved by adjusting the ratio of Ge and As. Here we study the $Re_3GeAs_6$ and $Re_3Ge_{0.6}A_{s6.4}$ materials. Like $Mo_3Sb_5Te_2$, its crystal structure contains large voids, making it also possible to fill in small cations as rattler. Co is attempted to insert in the crystal to get $Co_{0.05}Re_3Ge_{0.4}As_{6.6}$. The resulting thermoelectric properties are discussed in this document.

# DEDICATION

I dedicate this work to my husband and my parents. Without their continuous support, love and encouragement, I could not achieve this.

# ACKNOWLEDGMENTS

I would like to express my heartfelt gratitude to my advisor Dr. Terry Tritt for his support and guidance in my research. His attitude for research and life is always inspiring me. It is a pleasure to be his student.

I hereby express my appreciation to my committee member, Dr. Apparao M. Rao and Dr. Chad E. Sosolik for the precious suggestion.

I am also very thankful for the great assistance from the group members at the Complex and Advanced Materials Laboratory. Special thanks go to Paola Alboni for the help in high-temp thermal conductivity measurements, Dr. V. Ponnambalam for the help in high-temp resistivity measurements and Zhe Su for the help in heat capacity and Hall effect measurements. Also I need to give special thanks to Dr. Jian He and Dr. Xing Gao for very helpful discussion.

I am so grateful for the opportunity of working in the Complex and Advanced Materials Laboratory for my master degree. The experience here is the most precious treasure in my life. I learn from my advisor Dr. Tritt not only academically, but also spiritually. His attitude toward life is always inspiring me. He always looks at the bright side of the life. The friendship from the group members makes the group like a family, in which I feel comfortable and am inspired.

The deepest thanks go to my husband, also my group member, Bo Zhang for his continuous encouragement and support. Without his unconditional love and support, I cannot achieve this. He is someone who is always standing beside me.

Finally, special thanks and consideration go to my family, especially to my parents, whose support and love is always motivating me to achieve more.

TABLE OF CONTENTS

Page

LIST OF TABLES

LIST OF FIGURES

List of Figures (Continued)

Figure Page

List of Figures (Continued)

List of Figures (Continued)

Figure Page

# I INTRODUCTION

## Thermoelectric Effect

### Seebeck Effect

The Seebeck effect was discovered in 1821 by Thomas Johann Seebeck,[1] who found that a voltage existed between two ends of a metal bar when a temperature gradient ΔT existed in the bar. The effect is that a voltage, the thermoelectric EMF, is created in the presence of a temperature difference between two different metals or semiconductors.[2] This causes a continuous current to flow in the conductors if they form a complete loop. The temperature gradient across the material leads to an unequal distribution of charge carriers. Free carriers will have more energy at the "hot" end of the sample than the "cold" end and will diffuse further through the material. As a result of this unequal distribution of charge, a voltage proportional to the temperature gradient is established. In equilibrium, this new distribution of charge will establish an opposing electric field to prevent further charge diffusion. Suppose we have two materials A and B. We use A and B material to form a differential thermocouple as shown in Figure 1.1. If the two junctions are held at different temperatures, a voltage $V_{ab}$ will be generated and it is proportional to the temperature gradient $\Delta T$. The Seebeck coefficient is defined by

$$\alpha_{AB} = \frac{V_{AB}}{\Delta T} = \alpha_A - \alpha_B, \tag{1.1}$$

where $\alpha_{AB}$ is the relative Seebeck coefficient, and $\alpha_A$ and $\alpha_B$ are the absolute Seebeck coefficients for the individual conductors.[3] The sign of the Seebeck coefficient is usually indicates the type of carriers present in the material. A positive Seebeck coefficient indicates that the primary carriers are holes. On the contrary, a negative one shows that electrons are dominant carriers.

Peltier Effect

This effect was observed in 1834 by Jean Peltier.[1,4] The Peltier effect is the reverse of the Seebeck effect. It is the reversible exchange of heat from a junction of dissimilar materials in the presence of a current passing through the junction, which is held at a constant temperature. The Peltier coefficient, Π, is defined as the ratio of the rate of heating or cooling to the electrical current passing through the junction, as

$$\Pi = \frac{1}{I}\frac{dQ}{dt} = \alpha T , \qquad (1.2)$$

where $\frac{dQ}{dt}$ is the heat flow per unit time. $I$ is the electrical current. Depending on the direction of the current, heat can be absorbed or released at the junction of two dissimilar conductors as in Figure 1.2. The Fermi energies of the two conductors can be used to describe this phenomenon. In Figure 2, Heat is released at the junction if the Fermi energy of material A is larger than that of material B. On the contrary, if the Fermi energy of material B is larger than that of material A, heat is absorbed.

Thomson Effect

In 1851, Thomson (Lord Kelvin) predicted the cooling or heating of a homogeneous conductor resulting from the flow of an electrical current in the presence of a temperature gradient.[1,5,6]' This is know as the Thomson effect. And the Thomson coefficient, $\beta$, is defined as the rate of heat transferred per unit of temperature gradient per unit of current. The rate of heat transferred, known as Thomson heat, $Q_\beta$, in a uniform conductor is proportional to the electrical current given as:

$$dQ_\beta = \left(\int \beta dT\right) I dt \,. \tag{1.3}$$

The Thomson effect leads to a direct relationship between the Seebeck and Piltier coefficients:

$$\alpha = \frac{\Pi}{T} \,. \tag{1.4}$$

Thermoelectric Refrigeration and Power Generation

Based on the Seebeck effect and Peltier effect, there are two possible application of thermoelectric material: refrigeration and power generation.[7] Figure 1.3 shows the thermoelectric energy conversion couple. In the refrigeration mode, in which the Peltier effect is utilized, an external battery forces the electrons and holes away from the cold side of the device, resulting in cooling. In the power generation mode, in which the

Seebeck effect is used, heat is applied to the one side of the device, as a result, a voltage develops across the *n* and *p* legs that can be used to convert part of the heat into electrical power.

## Thermoelectric Figure-of-Merit

The efficiency of the thermoelectric material is evaluated by the dimensionless figure of merit, ZT,[8] given by

$$ZT = \frac{\alpha^2 \sigma}{\kappa} T , \tag{1.5}$$

where, $\alpha$ is Seebeck coefficient, also called thermopower, $\kappa$ is thermal conductivity and $\sigma$ is electrical resistivity, equal to the reciporical of resistivity $\rho$ . The numerator part is defined as power factor

$$P.F. = \alpha^2 \sigma T . \tag{1.6}$$

The thermal conductivity is from two parts: electrical contribution $\kappa_e$ and lattice contribution $\kappa_l$, so it can be represented as

$$\kappa = \kappa_e + \kappa_l . \tag{1.7}$$

The electrical conductivity (σ) and electronic thermal conductivity ($\kappa_e$) are correlated via the Wiedemann-Franz relationship $\kappa_e = L_0 T\sigma$, where the Lorentz number $L_0 = 2.45 \cdot 10^{-8} V^2 K^{-2}$. The most common route to improve ZT is to minimize $\kappa_l$ while preserving electrical conductivity and thermopower.

Materials are classified into metal, semiconductor and insulator by the electrical conductivity, which is a reflection of charge carrier concentration. And all three parameters in the figure-of-merit ZT are dependent on the carrier concentration.[9] Figure 1.4 shows the relationship and indicates that the electrical power factor reaches its maximum at a carrier concentration of around $10^{19}/cm^3$. The electrical contribution to the thermal conductivity is also increasing with carrier concentration. Consequently, the figure-of-merit optimizes at a specific carrier concentration which corresponds to that of doped narrow gap semiconductors.

## Material Introduction

$Ir_3Ge_7$ typed $Mo_3Sb_5Te_2$, $Nb_3Sb_2Te_5$, and $Re_3GeAs_6$ share the same structure as shown in Figure 1.5. In this type, the cationic atoms (M = Ir, Mo, Nb, Re ) are surrounded by eight anionic atoms (E = Ge; Sb, Te; Sb, Te; Ge, As) in form of a distorted square antiprism. Two such antiprisms share a common face leading to an M–M contact. Moreover, the faces opposed to the shared one are connected to the next pair of antiprism via secondary E–E bonds. This interconnection results in the formation of infinite linear chains comprising alternatingly empty E8 cubes and M2E12 double antiprisms. Parallel running chains are bonded to each other via short E–E bonds (Figure 1.6). The three-dimensional interconnection of these chains occurs at the E8 cubes, wherein each face is

part of a ME8 square antiprism, i.e. three linear chains interpenetrate each other at each cube.

$Mo_3Sb_7$ can be rendered semiconducting by a partial substitution of Sb with Te, resulting in $Mo_3Sb_5Te_2$ with 55 valence electrons per formula unit. This material complies to all the basic criteria for enhanced thermoelectrics such as high symmetry crystal structure with heavy elements and the possibility of rattling to further reduce the lattice thermal conductivity. $Nb_3Sb_2Te_5$ is isostructural and isoelectronic with $Mo_3Sb_5Te_2$. This material is an *n*-type semiconductor, with comparable Seebeck coefficients and smaller electrical conductivity compared to $Mo_3Sb_5Te_2$. $Re_3As_7$, was characterized as metallic with 56 valence electrons. The calculations by Dr. Kleinke's group at University of Waterloo show that its ternary, hitherto unknown variant $Re_3GeAs_6$ is semiconducting as well, and our preliminary measurements indicate that it exhibits *n*-type semiconducting character with better power factors than $Mo_3Sb_5Te_2$. Its Seebeck coefficients exceed -100μV/K at room temperature, and increase with increasing temperature.

In this document, the experimental procedure and results of the above materials will be discussed.

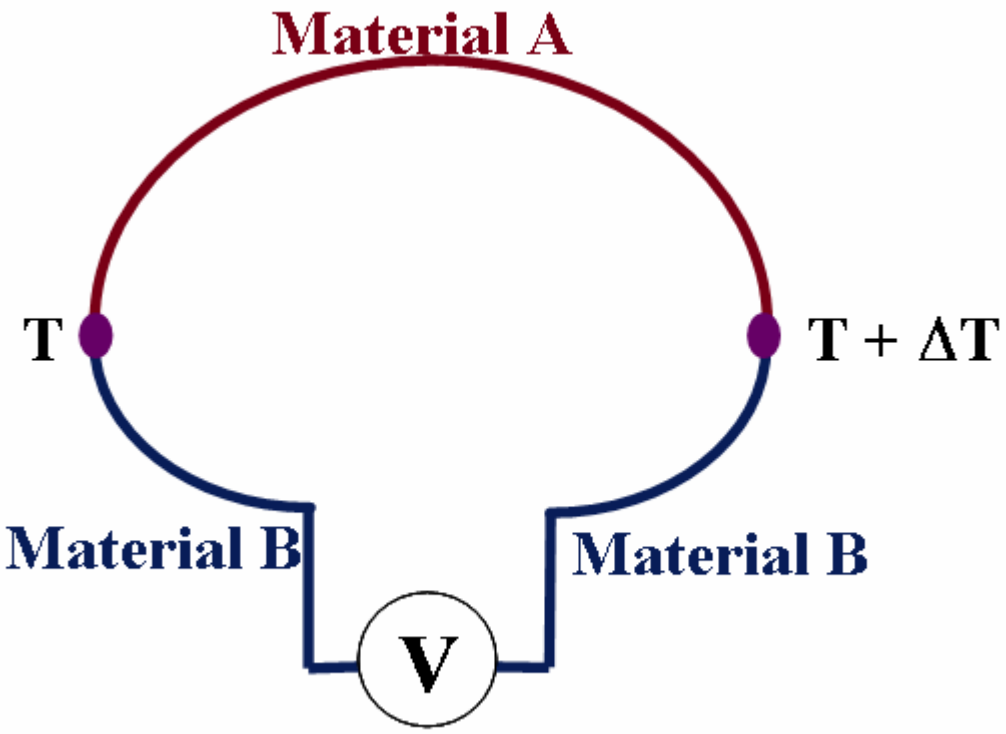


Figure 1.1: A Differential Thermocouple Illustration: an example of Seebeck effect

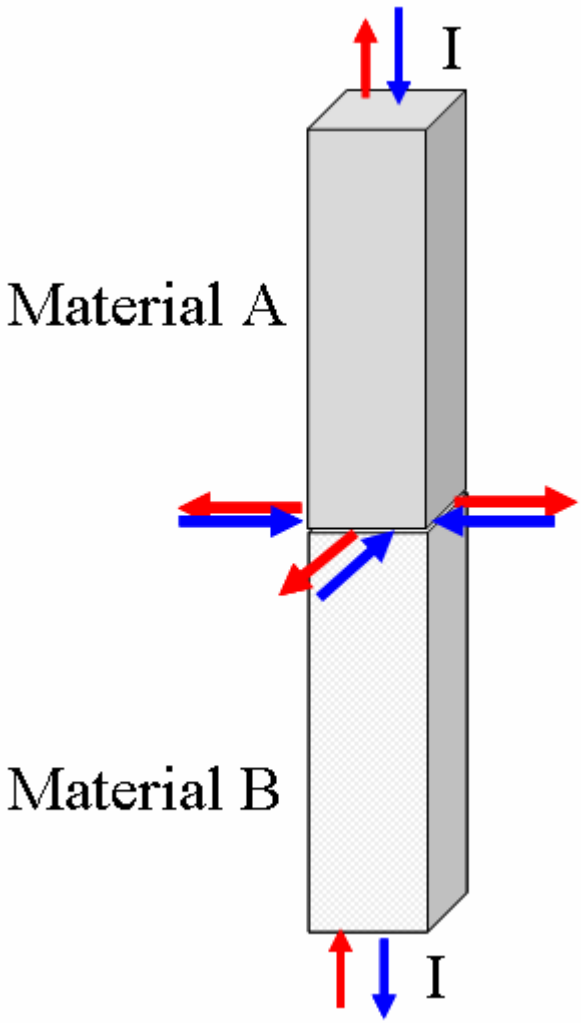


Figure 1.2: Peltier Effect Illustration (Red: release heat; Blue: absorb heat)

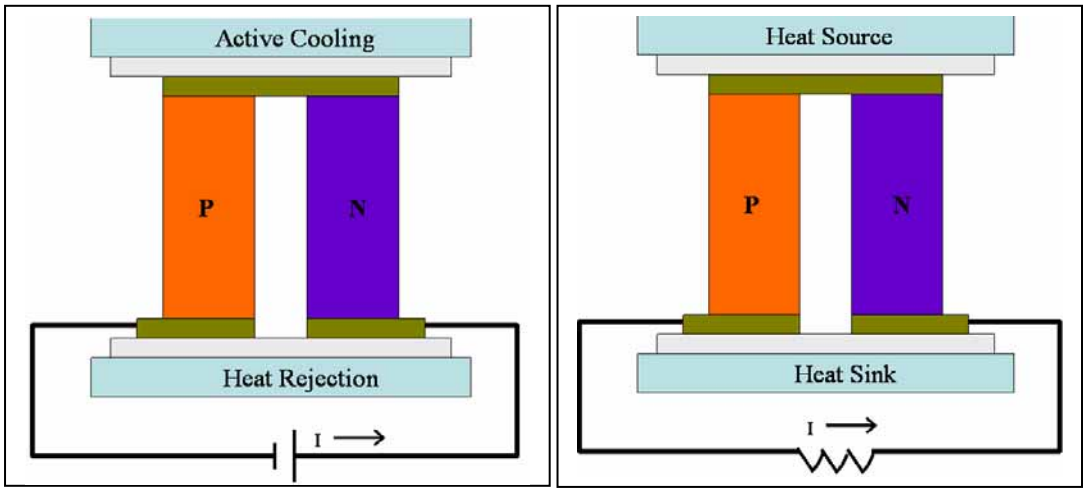


Figure 1.3: Thermoelectric Refrigeration (left) and Power Generation (right)

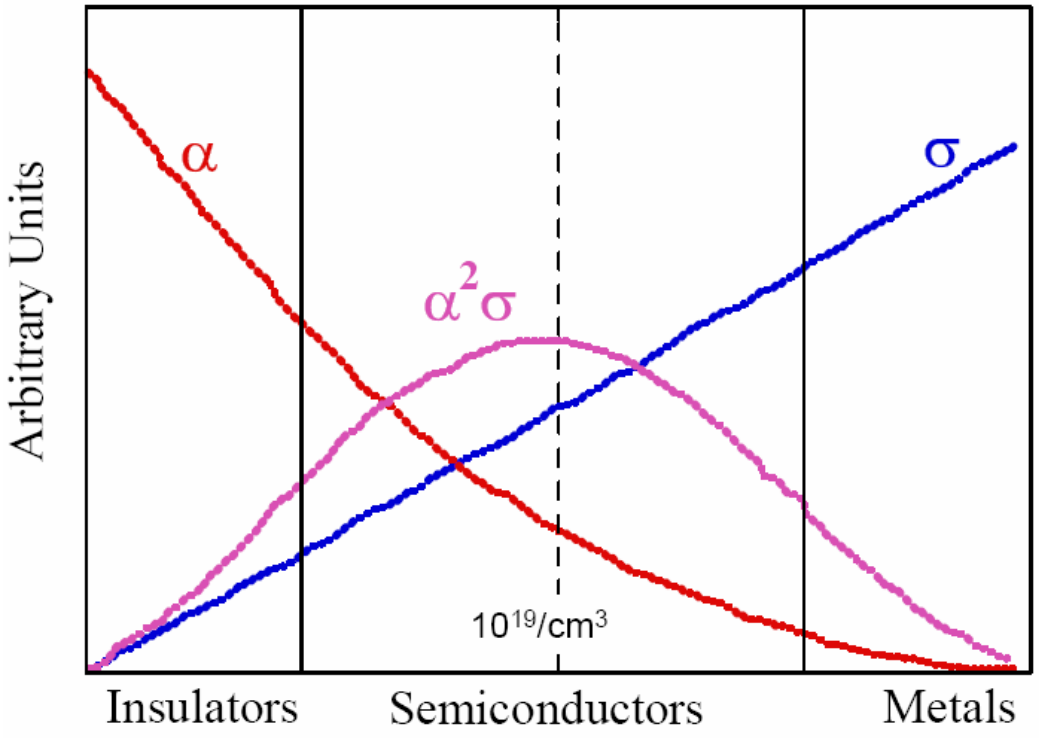


Figure 1.4: Power Factor As a Function of Carrier Concentration [9]

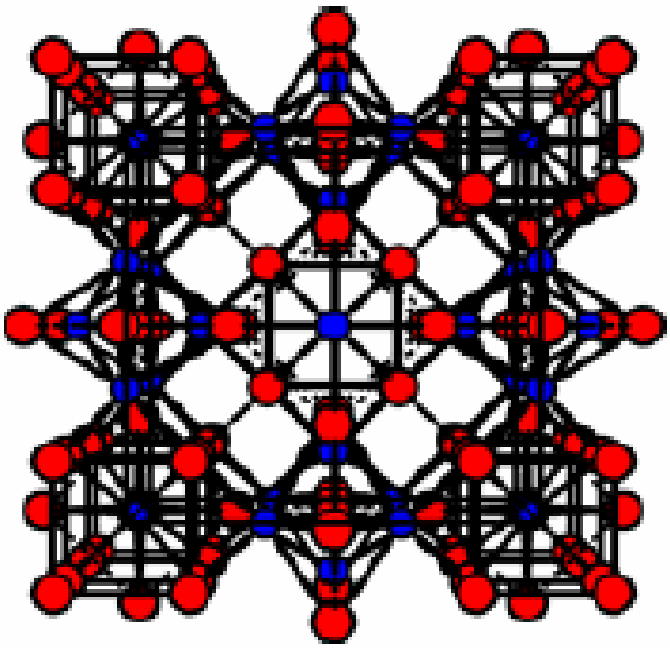

Figure 1.5: Crystal Structure of $Ir_3Ge_7$ typed material [10](Blue: M = Ir, Mo, Nb, Re; Red: E = Ge; Sb, Te; Sb, Te; Ge, As)

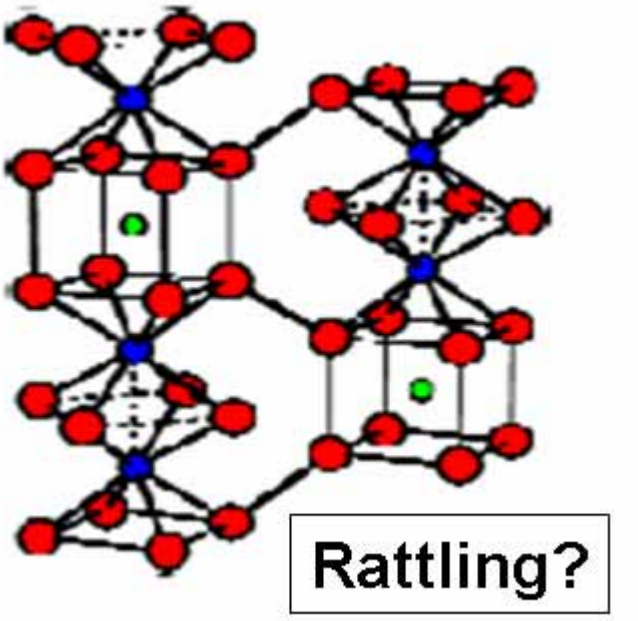


Figure 1.6: Two Parallel Chains of square antiprisms [10] (Blue: M = Ir, Mo, Nb, Re; Red: E = Ge; Sb, Te; Sb, Te; Ge, As; Green: rattling atom)

# II EXPERIMENTAL PROCEDURE AND APPARATUS

## Synthesis

All the Synthesis of the powder samples were performed in Dr. Kleinke's lab at University of Waterloo.

### The Synthesis of $Mo_3Sb_{7-\delta}Te_\delta$ and $Ni_{0.06}Mo_3Sb_{7-\delta}Te_\delta$

The Synthesis of the powder was performed in Dr. Kleinke's lab at University of Waterloo. All reactions were carried out in evacuated fused silica tubes, starting from the elements (Mo: powder, 3–7 mm, 99.95%, Alfa Aesar; Sb: powder, 2100 mesh, 99.5%, Alfa Aesar; Te: powder, 2200 mesh, 99.8%, Sigma Aldrich).[10,11] We always used 1.5 mmol Mo per reaction, and added the main group elements in the stoichiometric ratios, according to the general reaction equation:

$$3Mo + (7 - \delta)\ Sb + \delta Te \rightarrow Mo_3Sb_{7-\delta}Te_\delta \qquad (2.1)$$

$$(\text{with } 0 \leq \delta \leq 2.3)$$

The evacuated and sealed tubes were placed into a resistance furnace and heated up to the final reaction and annealing temperature of 750 °C. This reaction temperature ensures mobility of the main group elements, for it is above both the melting points of tellurium (450 °C) and antimony (630 °C), but well below the melting point of molybdenum(2620°C).The formation of $Mo_3Sb_{7-\delta}Te_\delta$ is thus a solid/liquid reaction.

Homogeneity was achieved by (i) applying a long reaction time of at least 10 days and (ii) grinding the samples, followed by reannealing at 750 °C for another 4–10 days. The title compound $Ni_{0.06}Mo_3Sb_{7-\delta}Te_\delta$ was prepared by annealing prepared $Mo_3Sb_{7-\delta}Te_\delta$ with Ni in powder form between 500 and 750 °C.

The Synthesis of $Re_3(GeAs)_7$

The reaction elements from ALFA AESAR (rhenium, powder, -325 mesh, 99.99%; germanium, powder, -100 mesh, 99.999%, arsenic, lump, 99.999%) were heated in the desired ratios in evacuated silica tubes at temperatures between 600°C and 800°C over a period of 7 – 14 days.[12] Phase pure samples of $Re_3Ge_\delta As_{7-\delta}$ could be prepared with $\delta$ = 1.0, 0.6, and 0.4, as analyzed by means of X-ray powder diffraction using the INEL powder diffractometer with position sensitive detector. The three samples of nominal composition $Re_3GeAs_7$, $Re_3Ge_{0.6}As_{6.4}$ and $Re_3Ge_{0.4}As_{6.6}$ were analyzed by means of standardless energy dispersive spectroscopy (EDS, LEO 1530, with integrated EDAX Pegasus 1200) using an acceleration voltage of 21 kV. The distribution of Re, Ge and As appeared to be homogeneous throughout each sample; and no additional peaks, hence no heteroelements were detected.

The Synthesis of $Nb_3Sb_2Te_5$

All reactions commenced from the elements (Nb: powder, -325 mesh, 99.8%, Alfa Aesar; Sb: powder, -100 mesh, 99.5%, Alfa Aesar; Te: powder, -200 mesh, 99.8%, Sigma–Aldrich), which were stored in argon filled glove box.[13] Different reactions were carried out, starting from the general Nb:Sb:Te ratio of $3:2-\delta:5+\delta$, with $-1/2 \leq \delta \leq 1/2$

($\delta$ was varied in steps of 0.1). The reaction mixtures were put into fused silica tubes, which were then evacuated and sealed. The tubes were placed into a resistance furnace, heated up gradually to 600 °C within 24 h, and kept at that temperature for 1 week. At that point, each tube was shaken vigorously to improve homogeneity. The final step was re-heating at 600 °C for a second week.

Each sample was analyzed by means of X-ray powder diffraction using the INEL diffractometer with Cu $K\alpha_1$ radiation and position-sensitive detector.[13] Only in case of $\delta = 0$, the powder diagram exhibited exclusively the reflections of $Nb_3Sb_2Te_5$; in all other cases, traces of $NbSb_2$ (when $\delta < 0$) or NbTe2 (when $\delta > 0$) were also found. As re-heating these samples at different temperatures between 500 and 800 °C did never yield phase pure $Nb_3Sb_2Te_5$, it is concluded that the phase range of $Nb_3Sb_{2-\delta}Te_{5+\delta}$, must be negligible, i.e. it is certainly smaller than $-0.1 \leq \delta \leq 0.1$. The sample of the nominal composition of $Nb_3Sb_2Te_5$ was analyzed by means of standardless energy dispersive spectroscopy (EDS, LEO 1530, with integrated EDAX Pegasus 1200) using an acceleration voltage of 21 kV. The distribution of Nb, Sb, and Te appeared to be homogeneous throughout the sample; and no additional peaks, hence no heteroelements were detected.

## Crystal Structure Determination

The crystal structure determination was done by Dr. Kleinke's group at University of Waterloo. A BRUKER Smart APEX CCD diffractometer with graphite-monochromatized Mo $K\alpha_1$ radiation was used for the data collection, performed by scans

of 0.3° in ω in two groups of 606 frames (each with an exposure time of 60 s) at $\phi$ = 0° and 60°.[10,12,13] The data were corrected for Lorentz and polarization effects. Absorption corrections were based on fitting a function to the empirical transmission surface as sampled by multiple equivalentmeasurements using SADABS. The structure solution and refinements were carried out with the SHELXTL program package. Details of the crystallographic data are listed in appendix part.

## Hot-press

The hot-press procedure was performed in our CAML lab at Clemson University. The powder samples were hot-pressed and densified using a hot-press procedure (Thermal Technology® HP20-4560-20 as shown in Figure 2.1). In practice, the sample powder is first cold-pressed into a pellet, which is then put into the graphite die to be heated by a furnace and pressed by two Mo rods as shown in Figure 2.1. The temperature, pressure, duration and density are listed in the Table 3.

## Electronic Structure Calculation

The LMTO method (LMTO, linear muffin tin orbitals) was utilized with the atomic spheres approximation (ASA) for the electronic structure calculations. In the LMTO approach, the density functional theory is used with the local density approximation (LDA) to treat correlation effects.[10,12,13] This part of work was done at University of Waterloo.

## Electrical Transport Properties Measurement

All the electrical transport properties measurements were done at Clemson.

### Resistivity and Thermopower Cryocooler System

The resistivity and thermopower are measured simultaneously from ~ 8 K to 310 K using a custom-designed cryocooler system.[14] Samples are mounted on a custom designed mounting chip as shown in Figure 2.2, which can be directly plugged into and removed from the cold finger on the system. Resistivity is measured by the standard four-probe method. During the measurement, the current is injected through one pair of leads ($I^+$, $I^-$) and voltage is measured using the other pair ($V^+$, $V^-$). The direction of the current is then reversed to subtract off the thermal voltage.

$$\rho = \frac{R_S A}{L} = \left(\frac{V_S}{I}\right)\frac{A}{L} = \left(\frac{V^+ + V^-}{2I}\right)\frac{A}{L} = \left(\frac{\left(R_S I^+ + V_{TE}\right) - \left(R_S I^+ + V_{TE}\right)}{2I}\right)\frac{A}{L} \quad . \tag{2.2}$$

For the thermopower measurement, according to the Seebeck effect $\alpha_{ab} = -V_{ab}/\Delta T$, the potential difference due to a temperature gradient needs to be measured. In the cryocooler system, the temperature gradient is measured by a 3-mil Chromel-Au-Fe (0.7 at % Fe)-Chromel differential thermocouple. The junctions of the thermocouple are permanently embedded in two copper blocks soldered to the two ends of the sample. The thermoelectric voltage ($V_{TE}$) is measured by a different set of voltage leads attached to the Cu blocks when the current is set to zero.

Seebeck Coefficient/Electric Resistance Measuring System

The high temperature resistivity and thermopower are measured on a Model ZEM-2 Seebeck Coefficient/Electric Resistance Measuring System.[15] The system can measure the thermopower and resistivity from room temperature to 800°C. Figure 2.3 shows the conceptual diagram illustrating the measurement of thermopower and electrical resistance. To improve the accuracy of measurement, samples should be prepared in the shape of prism or cylinder, of which one side or diameter is 2 to 4mm and length is 13 to 18mm. The both end surfaces of the sample should be parallel to each other. The samples mentioned in this document are in prism shape with dimension about $2\times2\times(6\text{-}8)mm^3$. Two probes A and B are attached to the sample to measure the voltage across A and B as $V_1$. At the meantime, the temperature is measured on point A and B as $T_A$ and $T_B$. In this way, the measuring temperature would be

$$T_{measure} = \frac{T_A + T_B}{2} \quad . \tag{2.3}$$

The voltage across a reference resistance *R*, which is connected in parallel with the sample, is measured as $V_2$. The sample resistance would be

$$R_{sample} = \frac{V_1}{V_2} \times R \quad . \tag{2.4}$$

During the measurement, the current applied to the sample is reversed in order to eliminate the influence of the thermopower at the contact point between the probe and the sample.

The resistivity can be derived by measuring the resistance value of the sample and taking the dimensions into account as following:

$$\rho = R\frac{A}{L}, \tag{2.5}$$

where, R is the sample resistance, A is cross-sectional area of the sample and L is the distance between the two probes.

Hall Effect Quantum Design Physical Property Measurement System

Hall effect measurements are made in the standard 5-probe technique (Figure 2.4) using the Physical Property Measurement System. [16] The sample is mounted on a Quantum Design® AC Transport puck. The current and voltage leads are soldered to the sample as in Figure 10 to provide the electrical contact. An excitation current of 100mA is sent through the sample. When a current is passing through a sample transverse to an applied magnetic field, a potential difference is developed perpendicular to both electric and the magnetic field. This is known as the Hall effect. The potential difference generated is called Hall voltage. The Hall voltage comes from the movement of the charge carriers in the sample under the Lorenz force ( $F = qv \times B$ ). The measurement of

the Hall effect, using the ACT option, requires the measurement of the Hall voltage as shown:

$$V_H = \frac{IB}{net} \tag{2.6}$$

where, $B$ is the magnetic field, $I$ is the current through the sample in the perpendicular direction, $\rho_H$ is the transverse Hall resistivity, $n$ is the carrier concentration, $e$ is the electronic charge and $t$ is the width or thickness of the sample. The carrier concentration is calculated from (2.6) as

$$n = \frac{IB}{V_H et} = \frac{B}{\rho_H e} \ . \tag{2.7}$$

Herein, a single carrier model is assumed.

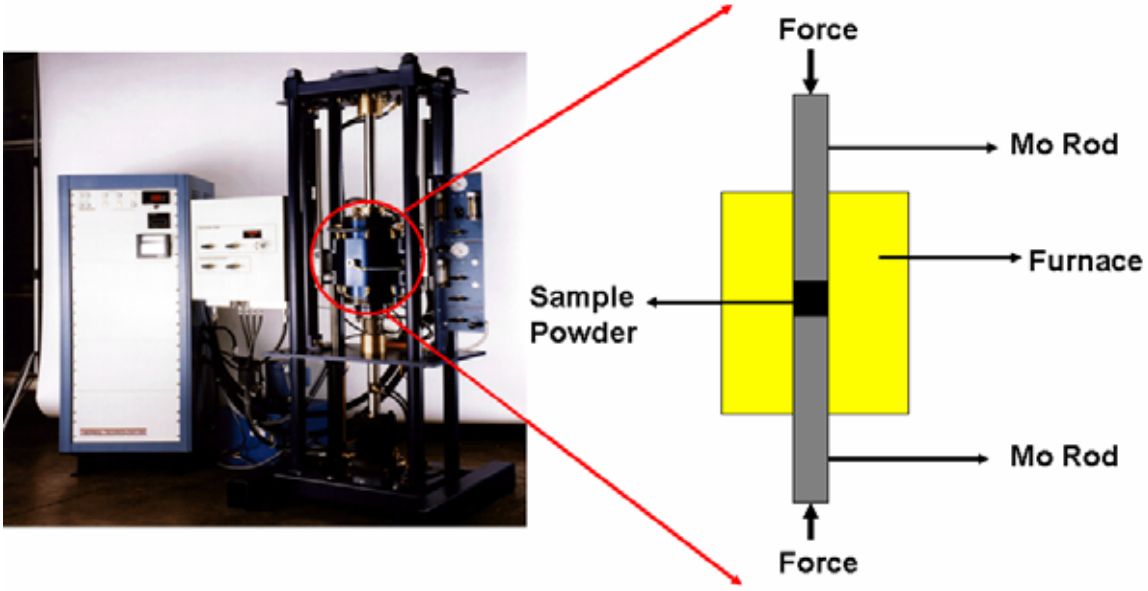


Figure 2.1: The Hot-press Equipment and Procedure Illustration

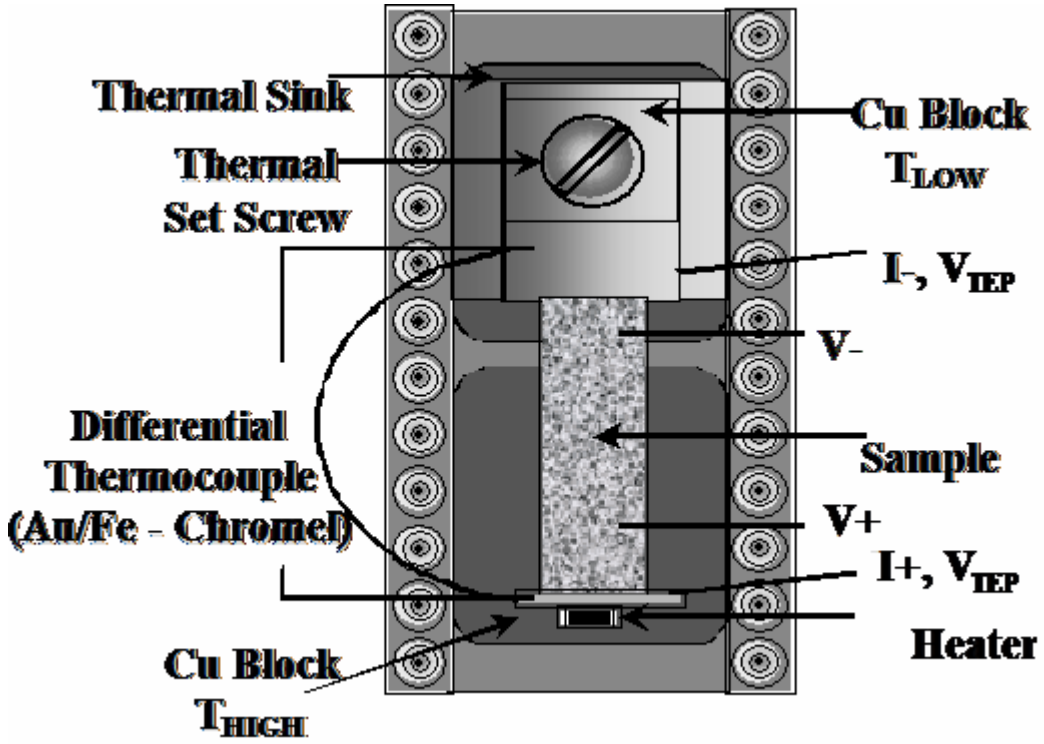


Figure 2.2: Resistivity and Thermopower Measurement Mounting Configuration

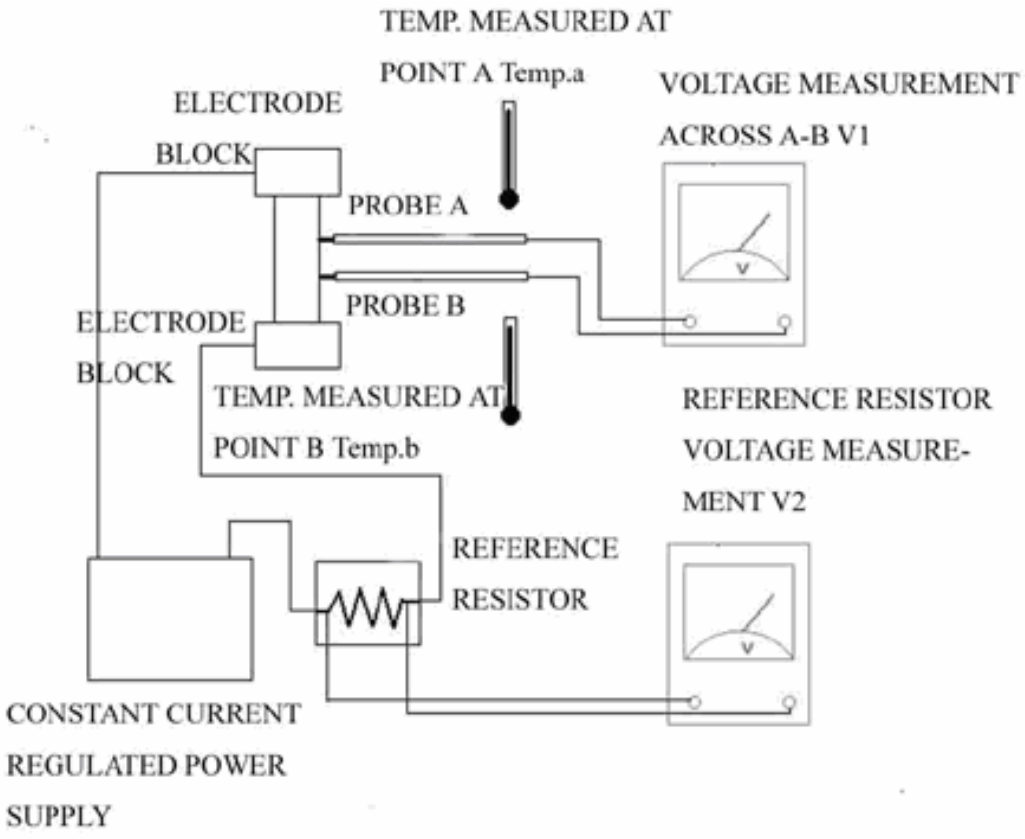


Figure 2.3: Conceptual Graph of High temperature Resistance/Seebeck Measurement[15]

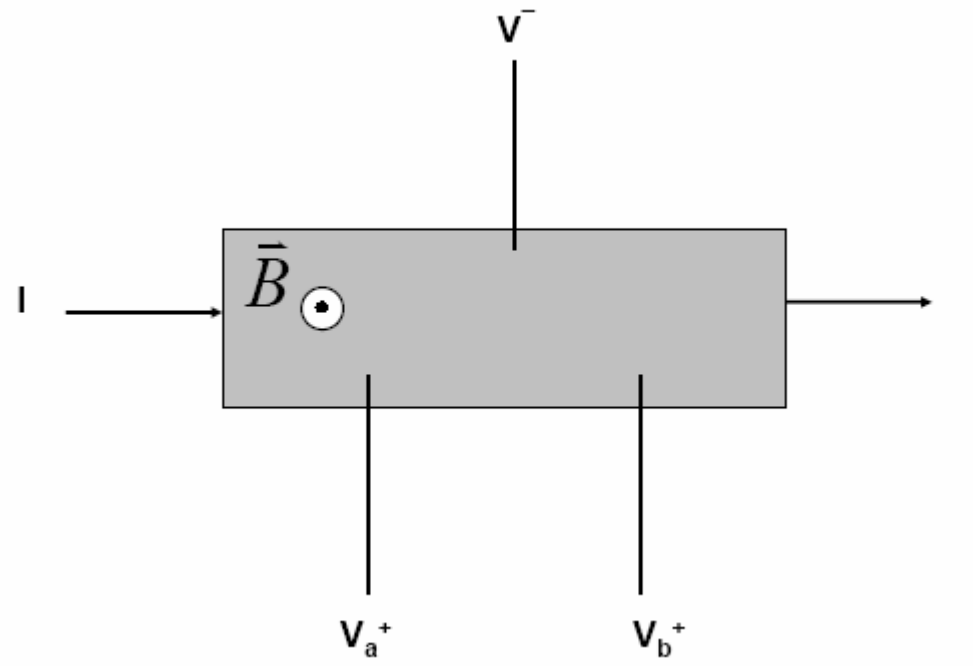


Figure 2.4: Hall Effect Measurement

## Thermal Tansport Properties Measurement

All the thermal transport properties measurements were done at Clemson.

### Steady State Thermal Conductivity Measurement System

When it comes to the measurement of the steady thermal conductance ($K$), a constant temperature difference ($\Delta T$) is required to be maintained. Here we use a stead state technique in which the sample reaches the complete thermal equilibrium (≈± 50mK). The determination of the thermal conductance is dividing the power input ( $P_R = I^2 R$ ) by the temperature gradient ($\Delta T$) caused by the heat flow through the sample. Thermal conductivity ($\kappa$) is calculated from thermal conductance by taking dimensions into account,

$$\kappa = KL/A, \tag{2.8}$$

where $L$ is the length between the thermocouples, $A$ is the cross-sectional area of the sample.

There are several factors affecting the heat flowing through the sample by heat loss via conduction, convection or radiation. A challenge to the steady state measurement is determining the various heat loss. In order to minimize the heat loss, we use small diameter wires with low thermal conductance to reduce conduction, high vacuum to reduce convection and gas reduction, and various designs to reduce radiation losses.

A Quantum Design puck is modified to accommodate two samples for the measurement of the thermal conductivity from ~10K to 300K.[17] A small copper plate is attached to

the puck with Stycast®. Two small copper blocks are adhered to the copper plate with screws. The samples are attached to small copper blocks with solder or Stycast®. In this way, the sample is thermally connected to the puck, so is to the system. A 120Ω strain gauge (heater) is attached to the top of the sample using a very thin layer of 5 min epoxy as a resistive heater. The mounting configuration and a picture of a mounted sample are shown in Figure 2.5. Since the thermal conductivity of the epoxy is low, it provides excellent thermal contact. The small size of the strain gauge (120Ω heater) is helpful for better thermal contact and less radiation loss. By replacing the existing leads of the strain gauge with phosphor-bronze wires, the heat loss is minimized. Two #38 Copper insulated wires are attached to the sample parallel to each other and perpendicular to the length of the sample with Stycast®. The coating on the top of the wires is scraped to provide a surface on which a 1-mil Cn-Cromega-Cn thermocouple is soldered. Using the copper wires helps to achieve good thermal contact, and also helps to avoid the thermocouple shorting to the sample. 1-mil Cn-Cromega-Cn thermocouple is used due to its low thermal conductivity, which leads to less conductive loss.

The data is collected by using graphical programming language Labview® by National Instruments. The temperature is stabilized to within +/-50mK throughout the ρ vs ΔT run. Although several ways are employed to minimize the heat loss, there are still some radiation losses above 150K. In the experiment, the power through the sample is

$$P_R = P_{Input} - P_{Loss} . \tag{2.9}$$

According to Stefan-Boltzman law[18], the heat transferred by radiation is given by the formula

$$P_{RAD} = A\sigma^2\varepsilon\left(T^4 - T_S^4\right), \tag{2.10}$$

where $P_{RAD}$ is the radiated power, $A$ is the cross sectional area of the sample, $\sigma$ is the Stephan-Boltzmann constant( $\sigma = 5.7\times10^{-8} Wm^{-2}K^{-4}$ ), $\varepsilon$ ( $0 < \varepsilon < 1$ )is the emissivity, $T$ is the temperature of the sample, and $T_S$ is the temperature of the system given by

$$T_S = T + \Delta T\,. \tag{2.11}$$

Taylor expansion of $T_S$ and assuming $\Delta T$ to be small gives

$$T_S^4 = \left(T + \Delta T\right)^4 = T^4 - T^3\Delta T + HigherOrderTerms\,,$$

which, when substituted into Equ(2.8), gives

$$P_{RAD} = A\sigma^2\varepsilon\left(T^3\Delta T\right). \tag{2.12}$$

When the thermal conductivity is measured, we use the Wiedemann-Franz relationship ( $\kappa_E = L_0 T/\rho$ ) to calculate the electronic contribution. By subtracting it from the total thermal conductivity ( $\kappa_t$ ), we get the lattice contribution $\kappa_L = \kappa_t - \kappa_E$ . By plotting the lattice thermal conductivity ( $\kappa_L$ ) and the lattice thermal conductivity

extrapolated ($\kappa_L$) from the lower temperature (<200K), the difference between the two is determined as $\Delta = \kappa_L - \kappa_{LE}$, which is assumed to be caused by radiation. If plotting $\Delta$ vs $T^3$ generates a linear relationship, it is likely that the difference is due to the radiation. Consequently, the total thermal conductivity can be corrected by the formula $\kappa_t = \kappa_E + \kappa_{LE}$.

Laser Flash and DSC Measurement of the High Temperature Thermal Conductivity

For high temperature thermal conductivity, we use laser flash thermal diffusivity (LFTD) method. The LFTD method measures the thermal diffusivity (*d*) and the specific heat ($C_p$) of the sample. The thermal conductivity is determined by

$$\kappa = dDC_V, \tag{2.13}$$

where *D* is the density of the sample, $C_V \approx C_P$ for solid.

*Diffusivity Measurement*

Thermal diffusivity is measured by a standard laser flash system (NETZSCH LFA 457)[19]. Figure 2.6 shows a conceptual graph of the laser flash system. The front surface of the cylindrically shaped sample piece (~0.1mm to 3mm) is homogeneously heated by a unfocused laser pulse as shown in Figure 2.7. The temperature rise on the rear surface is measured versus time using an infrared IR detector, which is cooled by liquid nitrogen. A thermocouple, which is mounted on the sample holder and located at the height of the

sample, measures the absolute temperature of the sample. The mathematical analysis of this temperature/time function (Figure 2.8) allows the determination of the thermal diffusivity *d*. For adiabatic conditions, *d* is determined by the equation

$$d = 0.1388 \frac{l^2}{t_{0.5}}, \tag{2.14}$$

where, *d* is the diffusivity in $cm^2/s$, *l* is the thickness of the sample piece, and $t_{0.5}$ is the time at 50% of the temperature increase, measured at the rear of the sample piece[19]. The sample chamber can be evacuated up to a vacuum of approx. $10^{-2}$ mbar via the software. The heat loss is corrected via integrated software. The samples are usually coated with a graphite film before the measurement.

*Specific heat measurement*

The thermal analysis method Differential Scanning Calorimetry (DSC) is a technique in which the heat flow rate to the sample is monitored.[20] In practice, the difference in heat flow rate to the sample compared to a reference material is monitored as in Figure 2.9.

Because of the thermal resistances at the sensor (red, shaded sections, figure on the right), small temperature gradients proportional to this heat flow differences are built up. The differential thermocouple measures these gradients with high precision and without any disturbance from the influences, which are common to the sample and reference (these are automatically filtered out by the differential arrangement). With temperature

depending changes of the specific heat and during transitions of the sample material (glass transition, melting, crystallization, structural changes, chemical reactions), the heat flow to the sample is different from the one to the reference side. The temperature difference caused by the difference in heat flow to the sample and the reference is measured. Specific heat (Cp) is measured by comparing the temperature rise of the test material with that of a material of known specific heat.

Heat Capacity Quantum Design Physical Property Measurement System

Heat capacity is also measured by the commercial Quantum Design Physical Properties measurement system (PPMS) from 2K to 300K at constant pressure[16]. In order to reduce conduction and convection heat losses, the measurement is performed under high vacuum. The sample is mounted by thermal grease to the platform of a removable Quantum Design Heat Capacity Puck as shown in Figure 2.10. A platform heater and platform thermometer are attached to the bottom of the sample platform. Eight delicate wires connected to the sample platform provide the electrical connection to the platform heater and the platform thermometer. A relaxation method is used to obtain the addendum and the heat capacity of the sample. In this method, a $\Delta T$ is established by controlling the injected heat to the sample. Then after turning off the heater, a relaxation curve is obtained and the relaxation time is determined. The whole measurements include two parts: addendum measurement and heat capacity measurement. In the addendum measurement, the puck with certain amount of N grease on the sample platform is measured[16]. Then the sample is mounted on the sample platform and the heat capacity is measured again. By subtracting the addendum from the heat capacity of the puck with

sample, the heat capacity of the sample is obtained. The suggested sample mass for the measurement is 1-200mg. The masses of the samples measured here are usually between 10-20mg. To get accurate data, it is very important to have a sample with a rather smooth surface which helps to make good thermal contact to the sample platform.

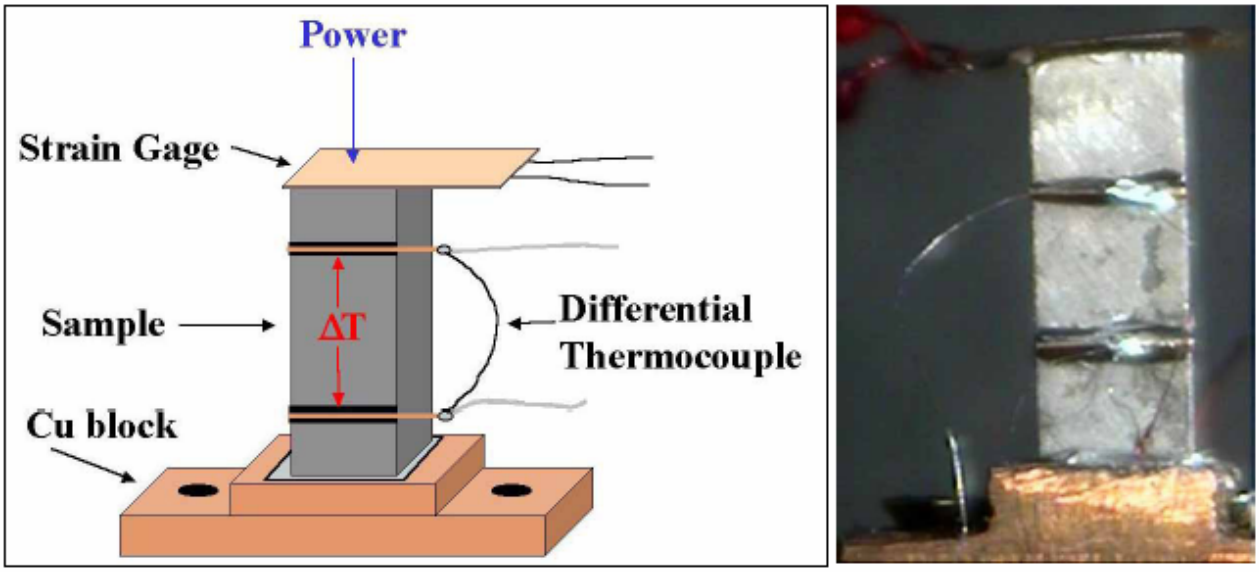


Figure 2.5: Thermal Conductivity Mounting Configuration and a mounted sample

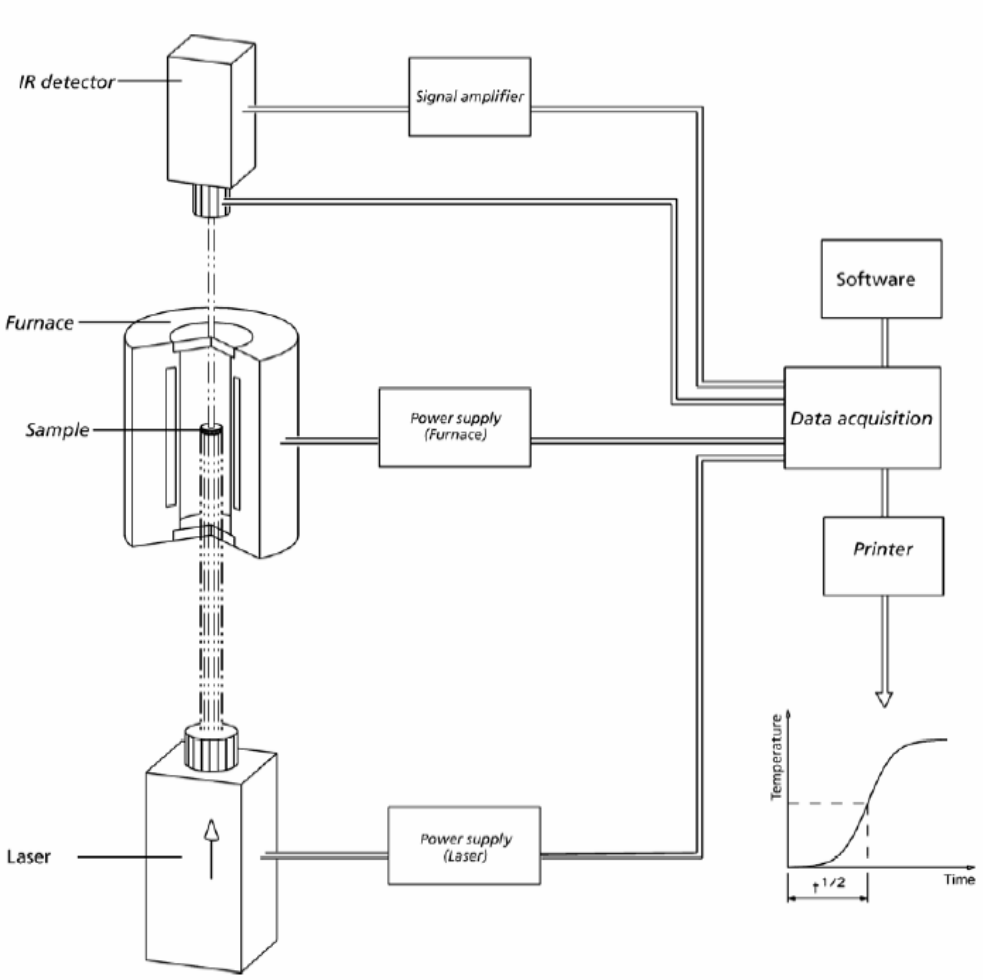


Figure 2.6: Laser Flash Principle [19]

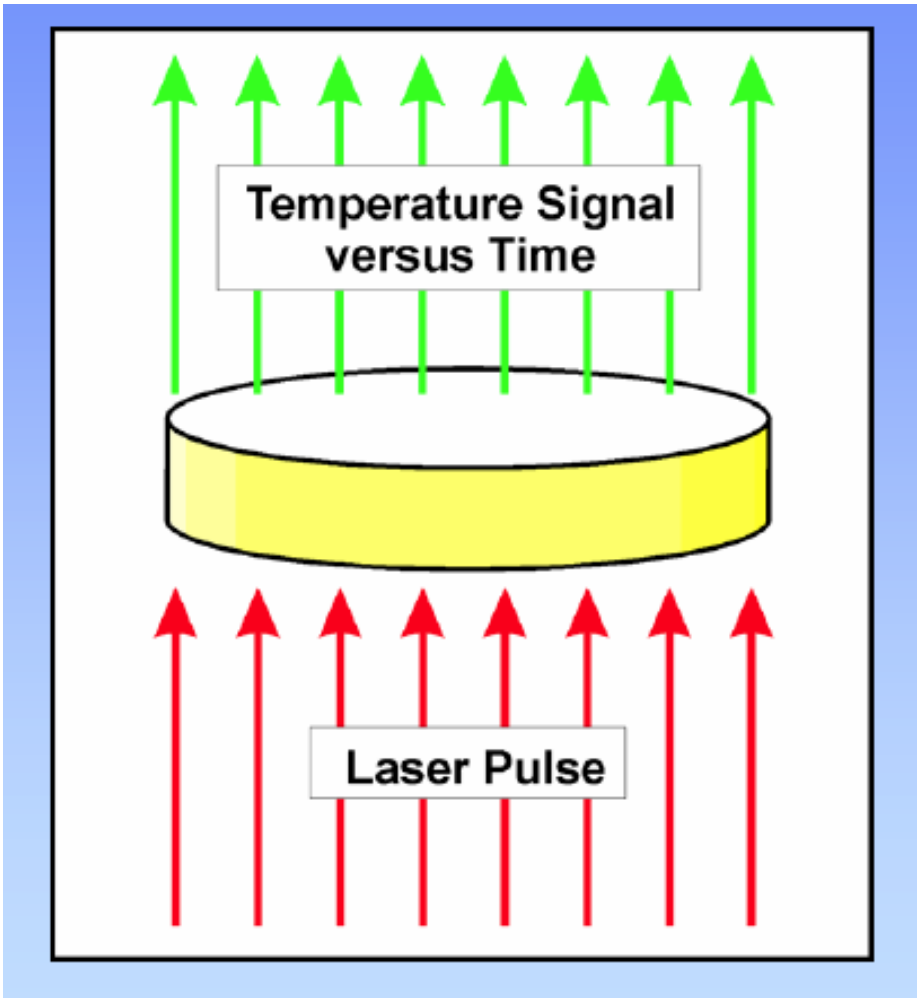


Figure 2.7: Laser Pulse [19]

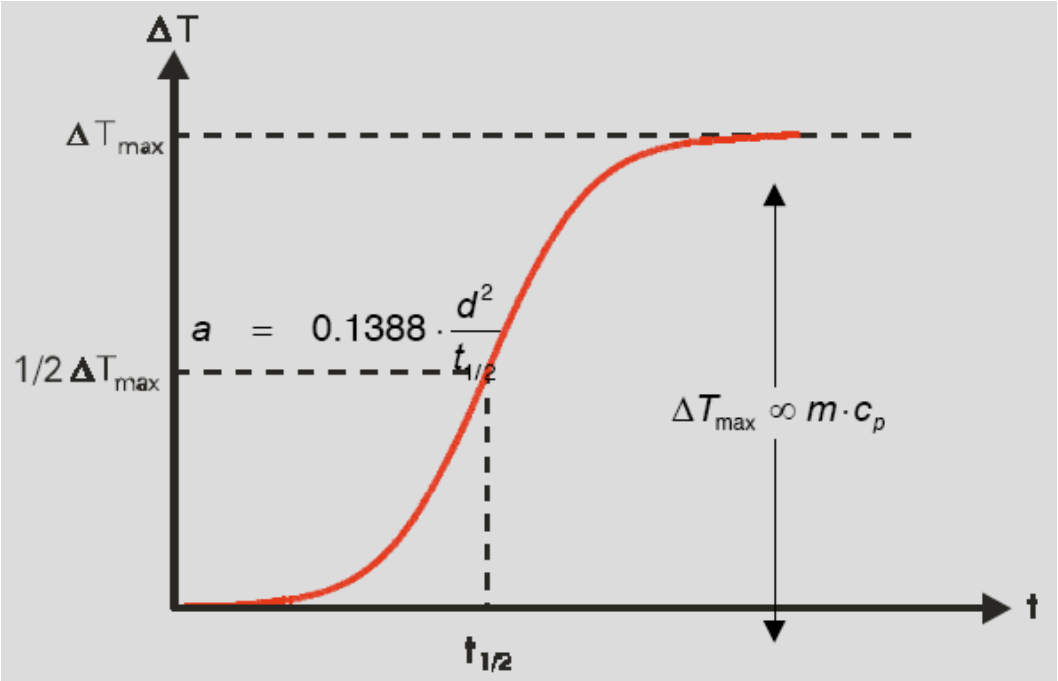


Figure 2.8: Temperature Increase as A Function of Temperature [19]

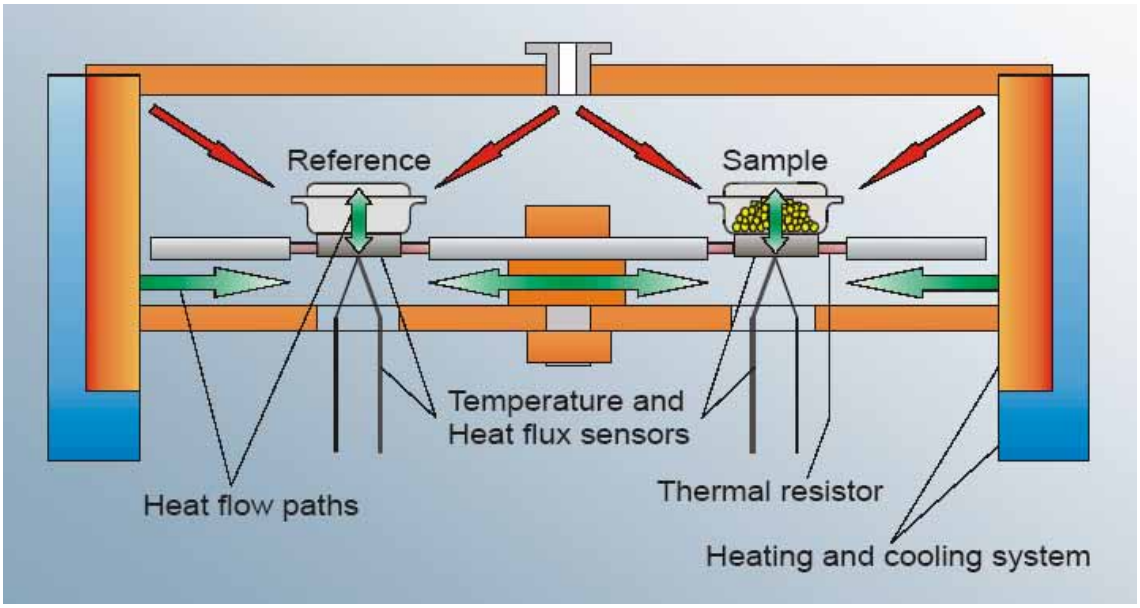


Figure 2.9: DSC Principle [20]

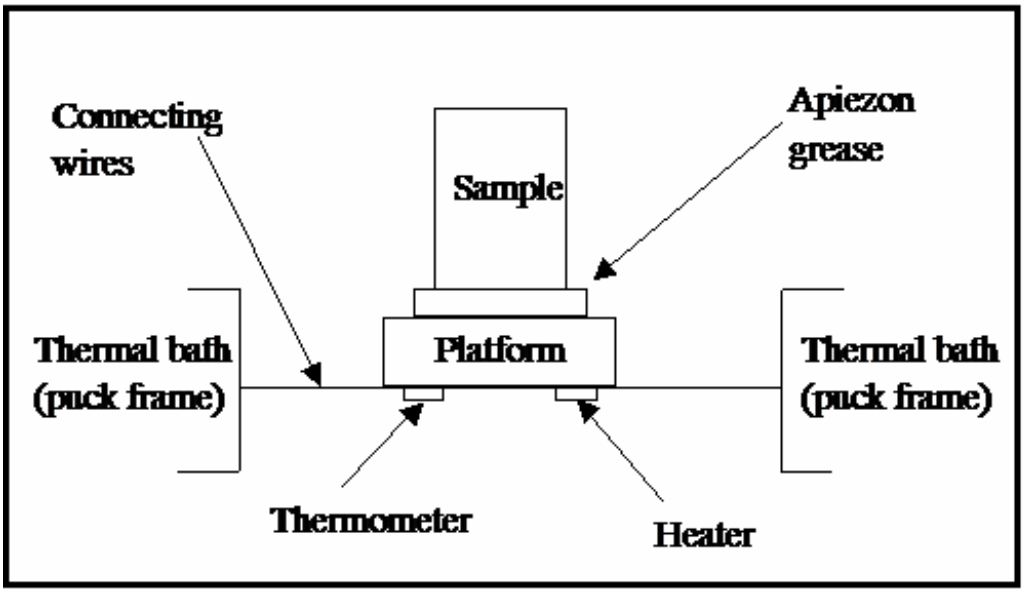


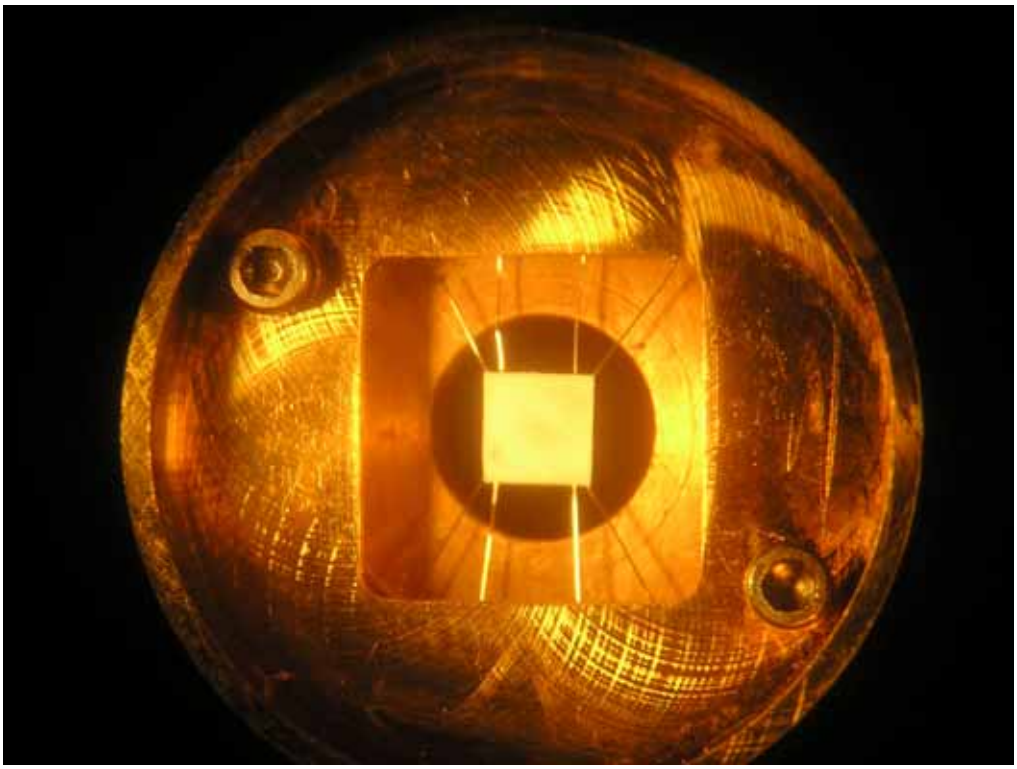

Figure 2.10: Specific Heat Measurement

# III EXPERIMENTAL RESULTS AND DISCUSSION

## $Mo_3Sb_{5.4}Te_{1.6}$ and $Ni_{0.06}Mo_3Sb_{5.4}Te_{1.6}$

### X-ray Diffraction

After the hot-pressing procedure, X-ray diffraction was taken for each sample with Rigaku MiniFlex X-ray machine. The identical diffraction patterns (Figure 3.1) of the $Mo_3Sb_{5.4}Te_{1.6}$ and $Ni_{0.06}Mo_3Sb_{5.4}Te_{1.6}$ samples, indicate that adding Ni does not change the crystal structure. The sharp shape of those peaks demonstrates that the two samples are excellently crystalline and no impurity peaks are identified.

### Electronic Band Structure

The band structure was calculated by Dr. Kleinke's group at University of Waterloo. The band structure of $Mo_3Sb_7$, shown in Figure 3.2, demonstrates a band gap above the Fermi level (fixed at 0 eV)[11], which may be reached by adding two valence electrons. Since several bands cross the Fermi level, $E_F$, along all symmetry lines selected, $Mo_3Sb_7$ will exhibit three-dimensional metallic properties. The bands with mostly Sb *p* orbital character are emphasized via the fat band representation. The band gap is located two valence-electrons per formula unit above $E_F$. The presence of numerous flat bands in the area around $E_F$ indicates high effective band masses that favor high thermopower. A band gap of ~0.9 eV occurs above the Fermi level. A smaller gap, namely of the size of 100-300meV (i.e., 6 - 10 $k_BT$ with $k_B$ = Boltzman constant, T = temperature) is recommended

for enhanced thermoelectric energy conversion. The region around $E_F$ is dominated by Mo *d* states, while most of Sb contributions are located well below and partly above $E_F$. Two major differences of the band structure of $Mo_3Sb_5Te_2$ (Figure 3.3), compared to the $Mo_3Sb_7$ band structure are: (i) the Fermi level falls right into the band gap, as anticipated; and (ii) the size of the band gap decreased from 0.9 eV to 0.5 eV.[10]

Low Temperature Resistivity and Thermopower

Figure 3.3 and Figure 3.4 shows the temperature dependence of the electrical resistivity and thermopower respectively for both $Mo_3Sb_{5.4}Te_{1.6}$ and $Ni_{0.06}Mo_3Sb_{5.4}Te_{1.6}$ samples[21]. For each of these materials, $Mo_3Sb_{5.4}Te_{1.6}$ and $Ni_{0.06}Mo_3Sb_{5.4}Te_{1.6}$, the electrical resistivity increases with the temperature, exhibiting a degenerate semiconductor type behavior; the signs of the thermopower are consistent with a p-type material (i.e. positive). This is in agreement with the previous band structure calculations. At 300K, the electrical conductivity values for each sample are respectively $1786\Omega^{-1}\cdot cm^{-1}$, $1852\Omega^{-1}\cdot cm^{-1}$; and the thermopower values are 49μV/K, 65 μV/K, for $Mo_3Sb_{5.4}Te_{1.6}$ and $Ni_{0.06}Mo_3Sb_{5.4}Te_{1.6}$, respectively. With respect to the comparison of electronic conductivity and thermopower data between the $Mo_3Sb_{5.4}Te_{1.6}$ and $Ni_{0.06}Mo_3Sb_{5.4}Te_{1.6}$, it is noticeable that for Ni-doping sample, the electrical resistivity is slightly decreased, indicating that the electrical conductivity is increased, but the thermopower is enhanced, too, thus improving power factor (P.F.= $\alpha^2\sigma T$) from 0.13 W-$m^{-1}K^{-1}$ to 0.23 W-$m^{-1}K^{-1}$ at 300K. In most cases, adding cations will increase the carrier concentration, as the result, the electrical conductivity is increasing and the thermopower is decreasing. Surprisingly, in our case, both electrical conductivity and thermopower are

enhanced by adding Ni cations. One possible scenario is that, the added Ni introduce more carriers and upshift the chemical potential such that it gets further away from the electron band, which is the minority band. Such a chemical potential shift makes the hole carrier more dominating, diminishing the offset of the thermopower by two different types of carriers.

Carrier Concentration and Hall Mobility

To verify this point, we measured the Hall coefficient between 15 K and 310 K, and calculated the corresponding Hall mobility. As shown in Figure 3.5 and Figure 3.6, adding Ni indeed introduces more carriers[21]. At room temperature, the virtual carrier concentration is increased from 4.0 x $10^{21}$/cm$^3$ in $Mo_3Sb_{5.4}Te_{1.6}$ to 4.9 x $10^{21}$/cm$^3$ in $Ni_{0.06}Mo_3Sb_{5.4}Te_{1.6}$. If we assume the added Ni adopt 3+ valence, the resultant carrier concentration increase is ~ 0.8 x $10^{21}$/cm$^3$, which is close to the improvement of the real carrier concentration at 15K which is 2.3 x $10^{21}$/cm$^3$. If Ni exists as $Ni^{2+}$, the increase of the carrier concentration is ~ 0.5 x $10^{21}$/cm$^3$. Adding Ni significantly alters the band structure, by simply adding 2 or 3 electrons per Ni to the system. Interestingly, while the carrier concentration $Mo_3Sb_{5.4}Te_{1.6}$ increases as the temperature decreases, the situation in $Ni_{0.06}Mo_3Sb_{5.4}Te_{1.6}$ is contrary to this. Meanwhile, the mobility has a value of a few cm$^2$/sec-V, typical of a degenerate semiconductor. The temperature dependences of mobility in both systems increase slowly with lowering temperatures, as expected from the scattering from the acoustic phonon modes.

High Temperature Resistivity and Thermopower

The high-temp resistivity and thermopower data are plotted together with the low-temp data in Figure 3.7 and Figure 3.8. In the high temperature range, both the resistivity and thermopower continue the low temperature trend: the thermopower of $Ni_{0.06}Mo_3Sb_{5.4}Te_{1.6}$ is keeping higher than that of $Mo_3Sb_{5.4}Te_{1.6}$, meanwhile, the resistivity of $Ni_{0.06}Mo_3Sb_{5.4}Te_{1.6}$ is lower than that of $Mo_3Sb_{5.4}Te_{1.6}$. The power factor reaches $1.43 Wm^{-1}K^{-1}$ and $1.64 Wm^{-1}K^{-1}$ at 800K for $Mo_3Sb_{5.4}Te_{1.6}$ and $Ni_{0.06}Mo_3Sb_{5.4}Te_{1.6}$, separately.

Low Temperature Thermal Conductivity

Figure 3.9 and Figure 3.10 shows the comparison of the thermal conductivity and lattice thermal conductivity of $Mo_3Sb_{5.4}Te_{1.6}$ and $Ni_{0.06}Mo_3Sb_{5.4}Te_{1.6}$. The lattice thermal conductivity is calculated by total thermal conductivity subtracting the electronic contribution. The Wiedemann-Franz relationship is employed for calculating carrier thermal conductivity. From the graph, it is apparent that the lattice thermal conductivity shows a crystal-like behavior[21]. From $Mo_3Sb_{5.4}Te_{1.6}$ to $Ni_{0.06}Mo_3Sb_{5.4}Te_{1.6}$, the lattice thermal conductivity increased from 3.1 $W\text{-}m^{-1}K^{-1}$ to 4.3 $W\text{-}m^{-1}K^{-1}$ at 300K, not as we expected for reducing thermal conductivity by rattling effect. Based on the crystal structure (see Figure 1.5 and Figure 1.6), the maximum occupancy of Ni per formula is 0.5. Accordingly, 12% of the Sb(2)-Sb(2) cubic voids, which is marked by a circle in Fig.4, are filled with our 0.06 Ni per $Mo_3Sb_{5.4}Te_{1.6}$ formula unit. As for this 12% occupancy, the thermal conductivity is expected to have an appreciable drop, if Ni indeed works as a “rattler”. However, we observed the opposite in that the lattice thermal

conductivity increased, which stimulates us to reconsider the possibility of a rattling effect in these materials.

In skutterudites, there are two necessary conditions in order to have the rattling effect. The first one is that the filler atom needs to be small and heavy such that it is loosely bonded to the "cage" and gives rises to some localized low frequency phonon modes (Einstein modes). The second one is more subtle, it requires the filler atom to have multiple meta-stable positions in the "cage". Our case qualifies the first criterion well. The radius of Ni atom, 0.124nm,[11] is small enough for the cubic "cage" which, revealed by the crystal structure analysis, is formed by the 0.310nm long Sb(2)-Sb(2) bonds. Furthermore, according to our evaluation, if the intercalated cation Ni locates in the center of this "cage", there would be a 0.269nm long distance from Sb(2) atom and 0.328nm from Mo atom[1], suggesting that the cation is small enough to be potential rattlers. Nevertheless, not all fillers in large voids work as rattlers. In our case, our thermal conductivity data suggests that, very likely, the Ni atoms work just like space-fillers which help densify the materials and thus enhance the thermal conductivity. Although, at the present stage, it is still unknown why, in the "$Ir_3Ge_7$"crystal structure, filling Ni into the large voids is not creating rattling effect; it is noted that the thermal conductivity for unfilled skutterudite materials is much higher than the unfilled $Mo_3Sb_{5.4}Te_{1.6}$.

Specific Heat

Debye's theory, one of the earliest quantum theories of lattice specific heats, gives an excellent explanation of the specific heat in solid based on crude approximations to the

normal-mode dispersion relations. The Debye model considers that there are only three branches of vibrational spectrum and each has the same linear dispersion relation.[22] These simplifications result in

$$c_v = 9nk_B\left(\frac{T}{\theta_D}\right)^3 \int_0^{\theta_D/T} \frac{x^4 e^x dx}{\left(e^x - 1\right)^2} \quad , \tag{3.1}$$

where, $\theta_D$ is Debye temperature. The way to pick $\theta_D$ is by making (3.1) equal to the experimental result at low temperatures (≤5K). Thus, the lattice contribution for the specific heat at low temperature results in

$$c_v = \frac{12\pi^4}{5} nk_B\left(\frac{T}{\theta_D}\right)^3 = 234\left(\frac{T}{\theta_D}\right)^3 nk_B \cong 1944\left(\frac{T}{\theta_D}\right)^3 \quad . \tag{3.2}$$

It can be determined by fitting the $T^3$ term in the specific heat at very low temperatures. The total specific heat is from the electronic and the lattice contribution as shown by

$$c_v = \gamma T + \beta T^3 \quad . \tag{3.3}$$

By plotting a graph of $c_v / T$ vs. $T^2$ at very low temperature, $\beta$ and $\gamma$ are determined by the slope and the intercept. The Debye temperature can be calculated by

$$\theta_D = \left(\frac{1944}{\beta}\right)^{1/3}. \tag{3.4}$$

The Figure 3.11 and Figure 3.13 show the heat capacity of $Mo_3Sb_{5.4}Te_{1.6}$ and $Ni_{0.06}Mo_3Sb_{5.4}Te_{1.6}$. The calculated Debye temperatures of the two samples, as shown in Figure 3.12 and Figure 3.14, are 311K for $Mo_3Sb_{5.4}Te_{1.6}$ and 297K for $Ni_{0.06}Mo_3Sb_{5.4}Te_{1.6}$. The Debye temperatures of the two samples are much higher than other good thermoelectric materials such as PbTe(150K) and $Bi_2Te_3$(162K). Since the Debye temperature is corresponding to the highest frequency of the phonon, this can partially explain that the thermal conductivity of the two samples are higher than PbTe and $Bi_2Te_3$. The Debye temperatures of all the samples are summarized in Table 2.

High Temperature Thermal Diffusivity

The high temperature thermal conductivity is measured by the laser flash thermal diffusivity method (LFTD). The thermal conductivity is determined by the thermal diffusivity and the specific heat of the sample through Equation (2.11). In the experiment, the thermal diffusivity and the specific heat are measured separately. The thermal diffusivity of the two samples is shown in Figure 3.15. According to Equation (2.11), the thermal conductivity is dependent on the thermal diffusivity, the specific heat and the density of the sample. For a specified sample, the density is a constant and the specific heat is weakly dependent on temperature after room temperature. So the diffusivity dominately reveals the thermal conductivity. From Figure 3.16, we see the diffusivity of the sample with Ni is higher than that of the sample without Ni, indicating most likely the

thermal conductivity increased by adding Ni. This is in agreement with the low temperature result.

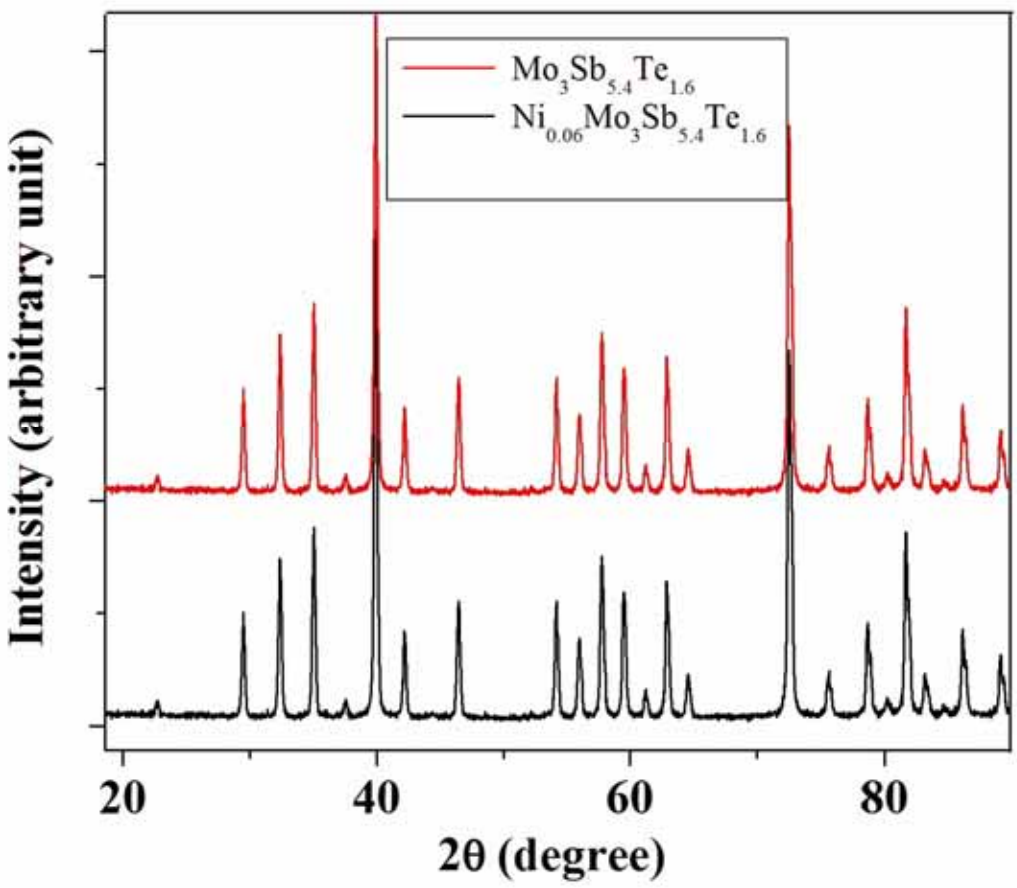


Figure 3.1: X-ray Diffraction Pattern of $Mo_3Sb_{5.4}Te_{1.6}$ and $Ni_{0.06}Mo_3Sb_{5.4}Te_{1.6}$

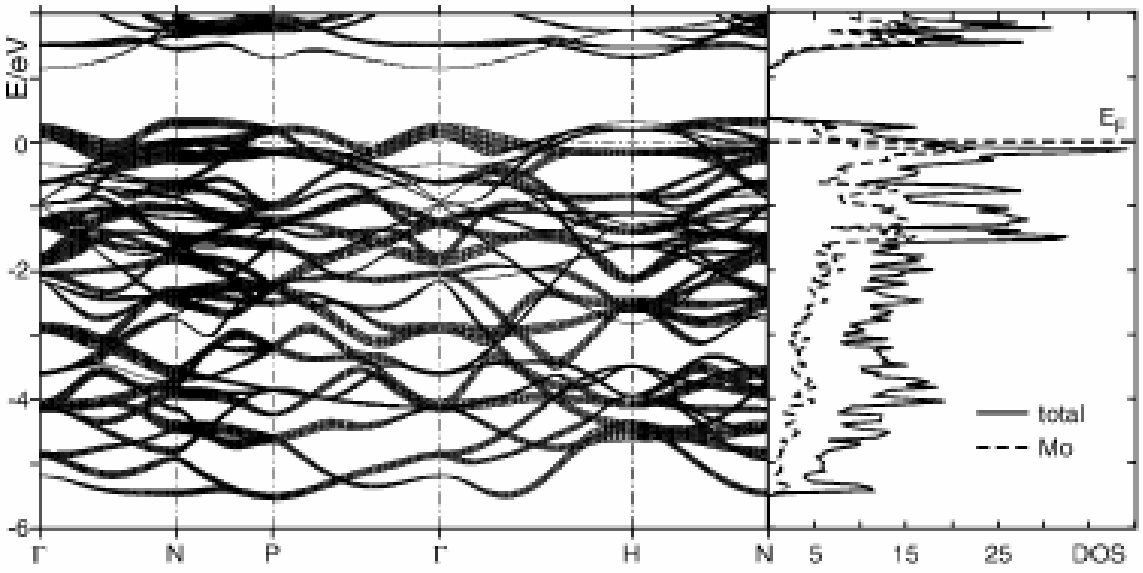


Figure 3.2: Band Structure and Density of States (DOS) of $Mo_3Sb_7$

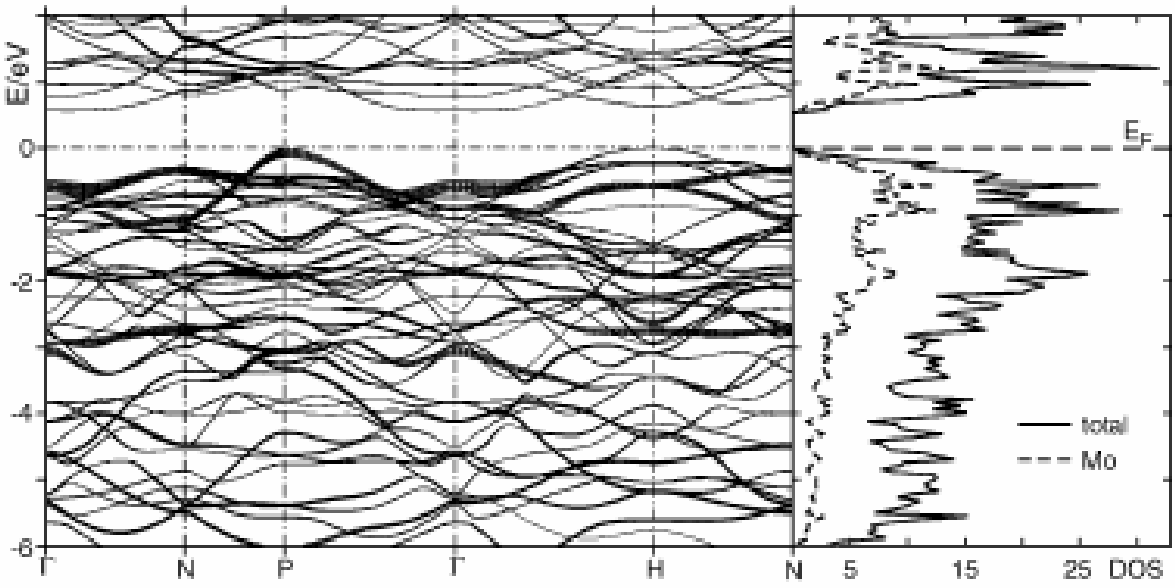


Figure 3.3: Band Structure and Density of States (DOS) of $Mo_3Sb_5Te_2$

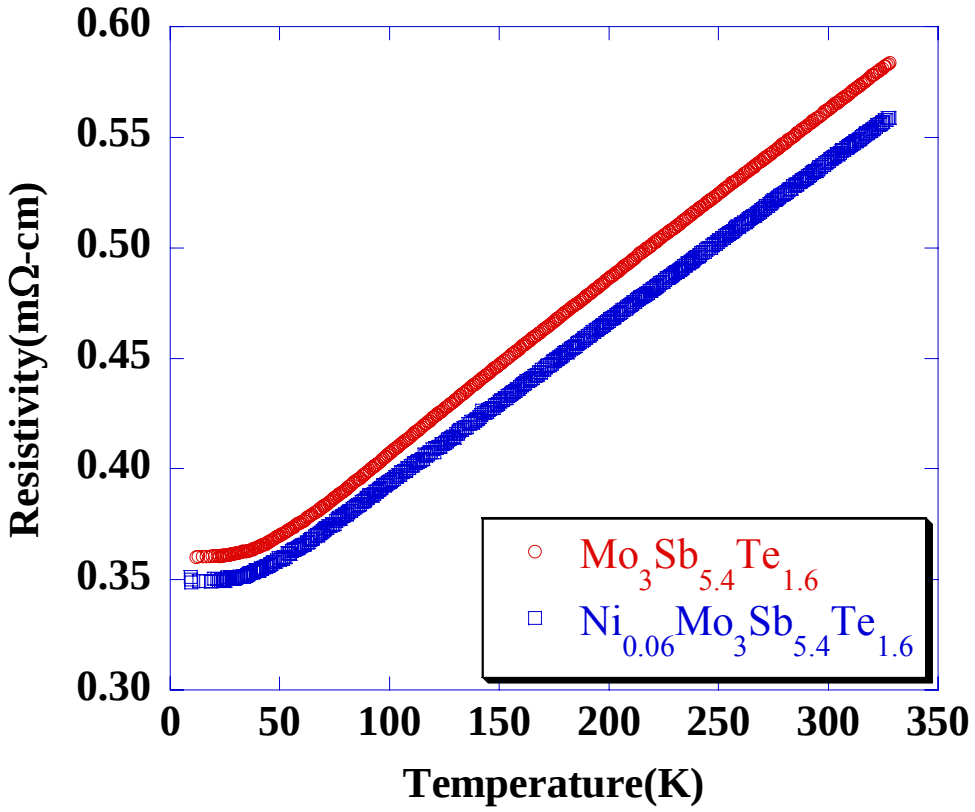


Figure 3.4: Low Temperature Electrical Resistivity of $Mo_3Sb_{5.4}Te_{1.6}$ and $Ni_{0.06}Mo_3Sb_{5.4}Te_{1.6}$

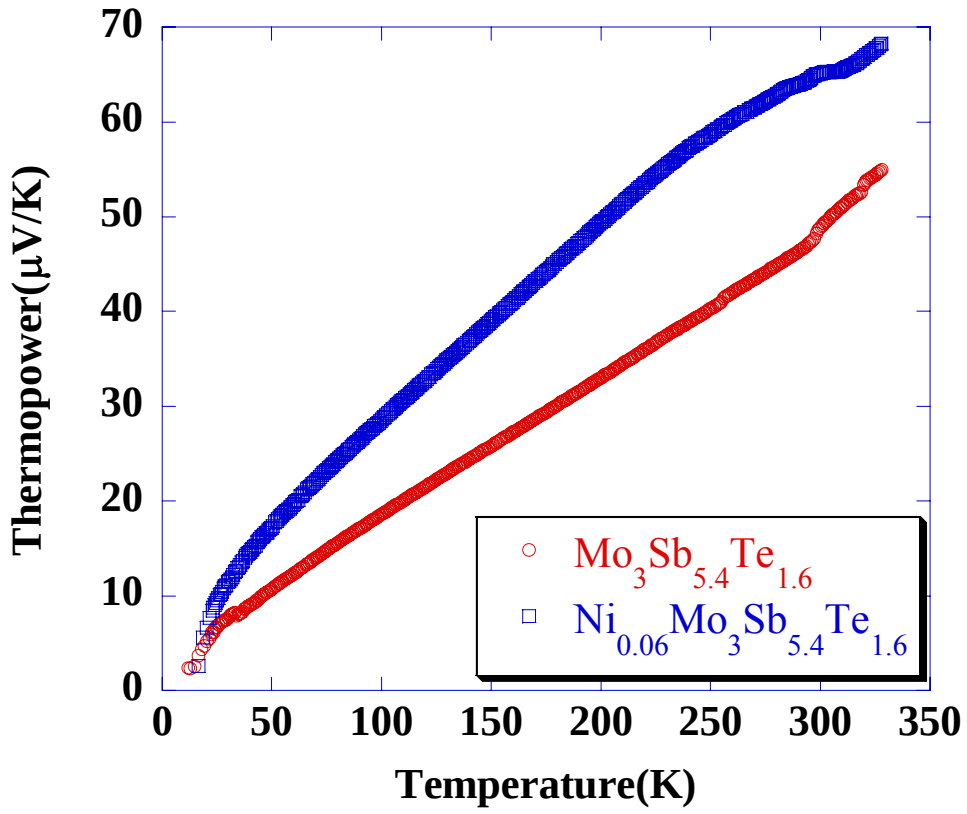


Figure 3.5: Low Temperature Thermopower of $Mo_3Sb_{5.4}Te_{1.6}$ and $Ni_{0.06}Mo_3Sb_{5.4}Te_{1.6}$

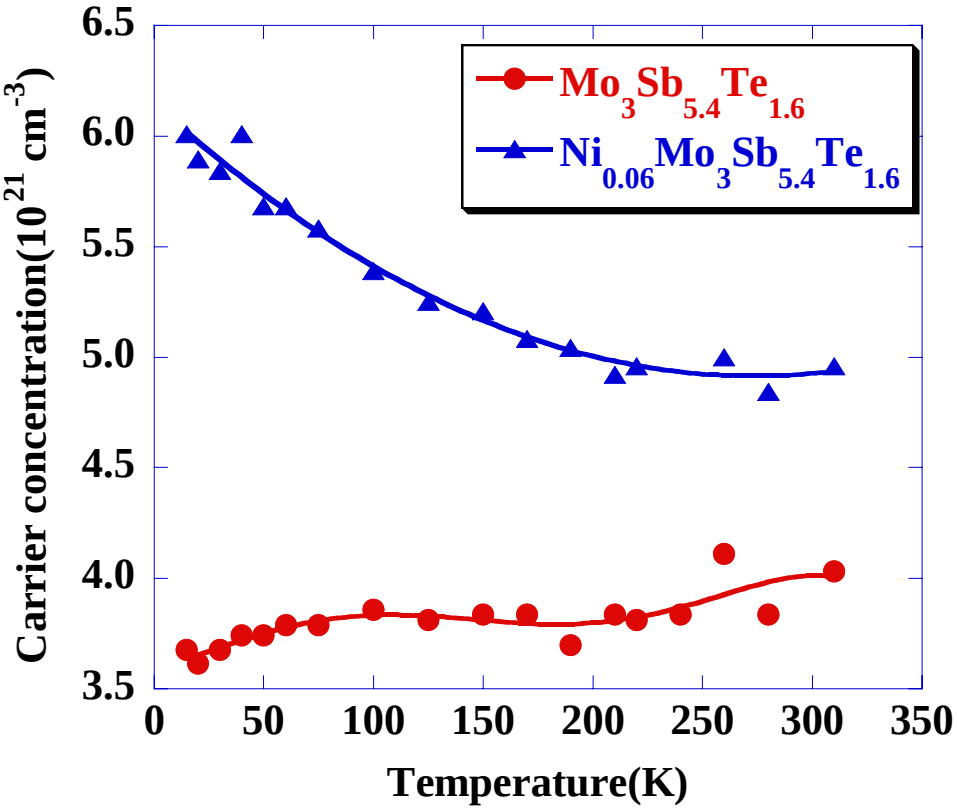


Figure 3.6: Carrier Concentration of $Mo_3Sb_{5.4}Te_{1.6}$ and $Ni_{0.06}Mo_3Sb_{5.4}Te_{1.6}$

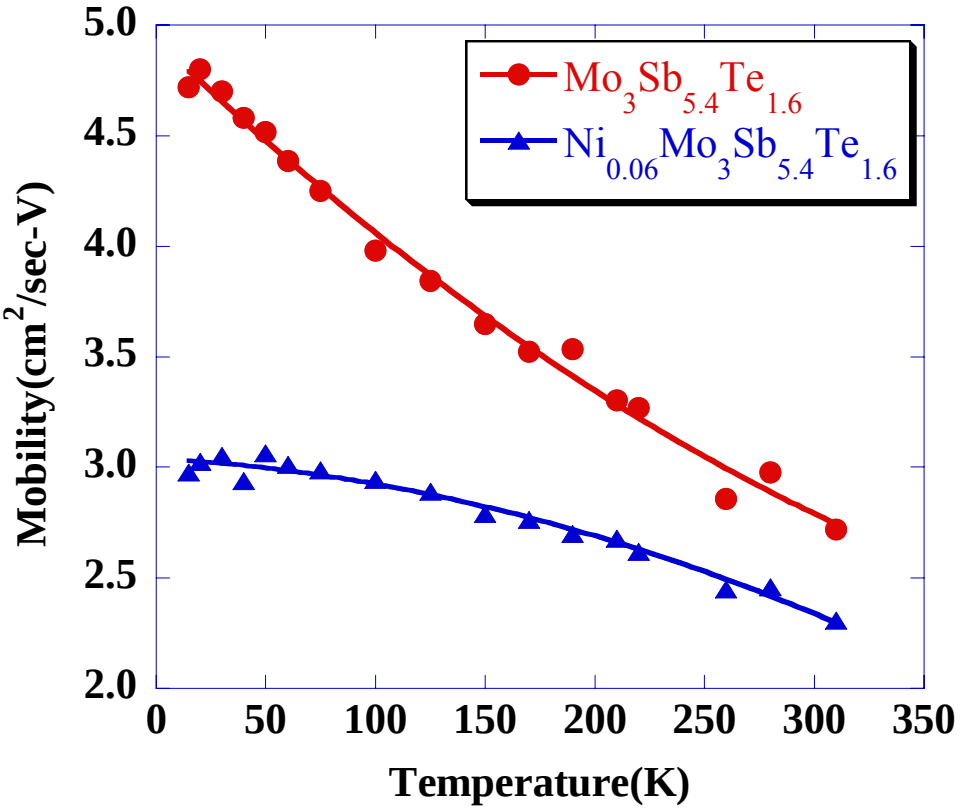


Figure 3.7: Mobility of $Mo_3Sb_{5.4}Te_{1.6}$ and $Ni_{0.06}Mo_3Sb_{5.4}Te_{1.6}$

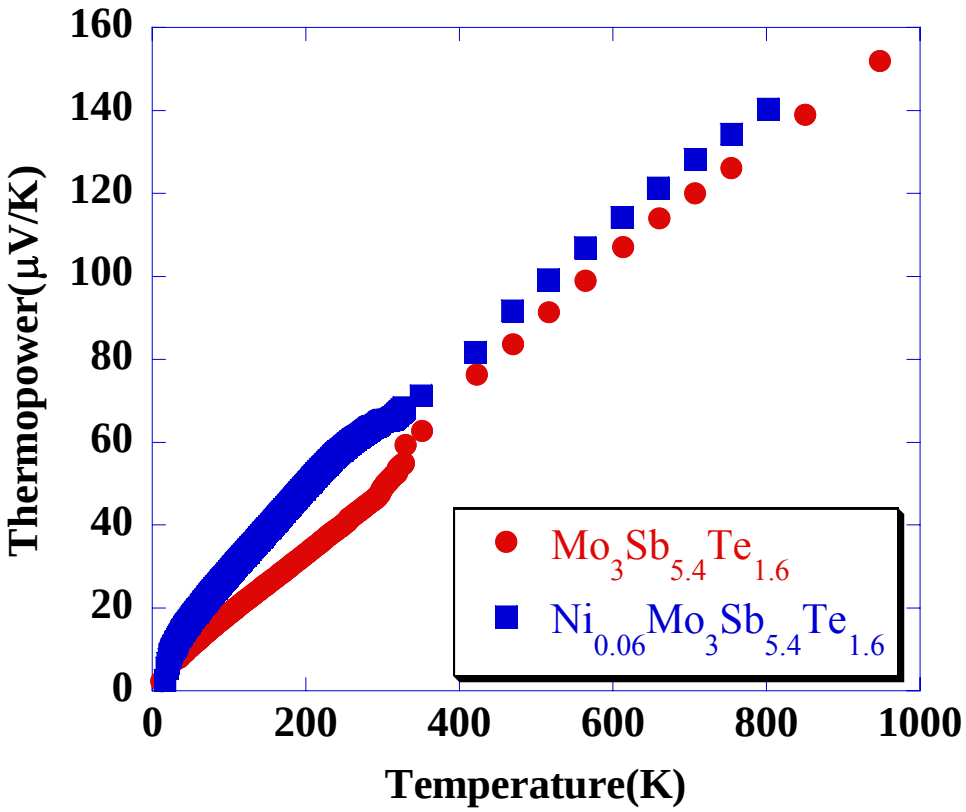


Figure 3.8: High Temperature Thermopower of $Mo_3Sb_{5.4}Te_{1.6}$ and $Ni_{0.06}Mo_3Sb_{5.4}Te_{1.6}$

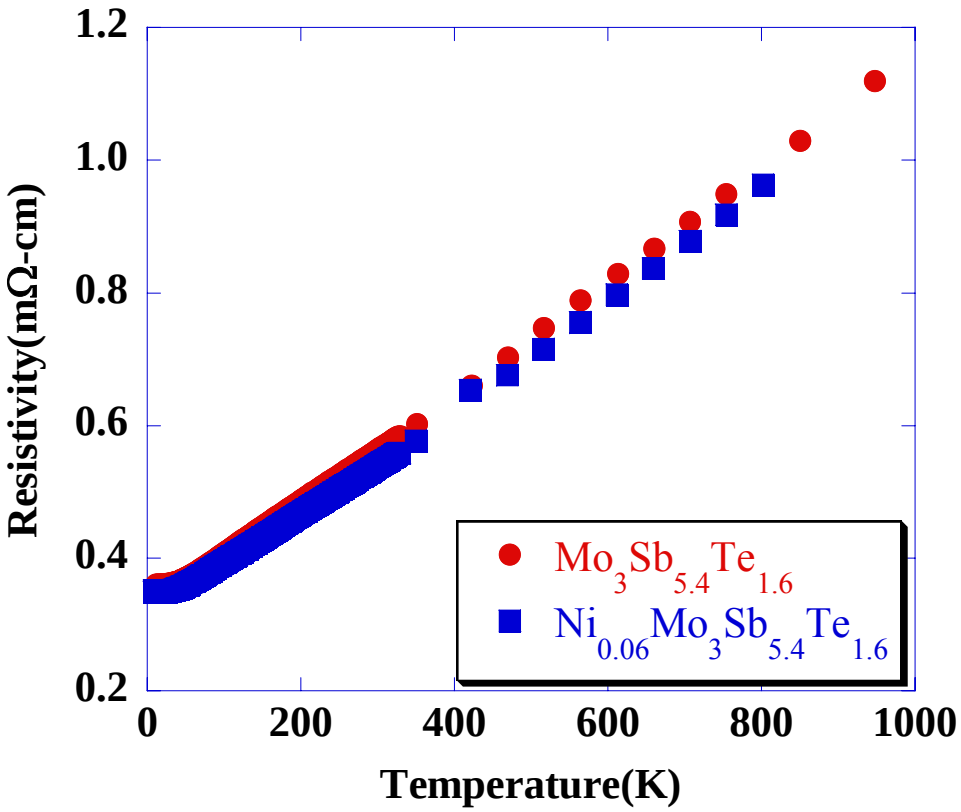


Figure 3.9: High Temperature Resistivity of $Mo_3Sb_{5.4}Te_{1.6}$ and $Ni_{0.06}Mo_3Sb_{5.4}Te_{1.6}$

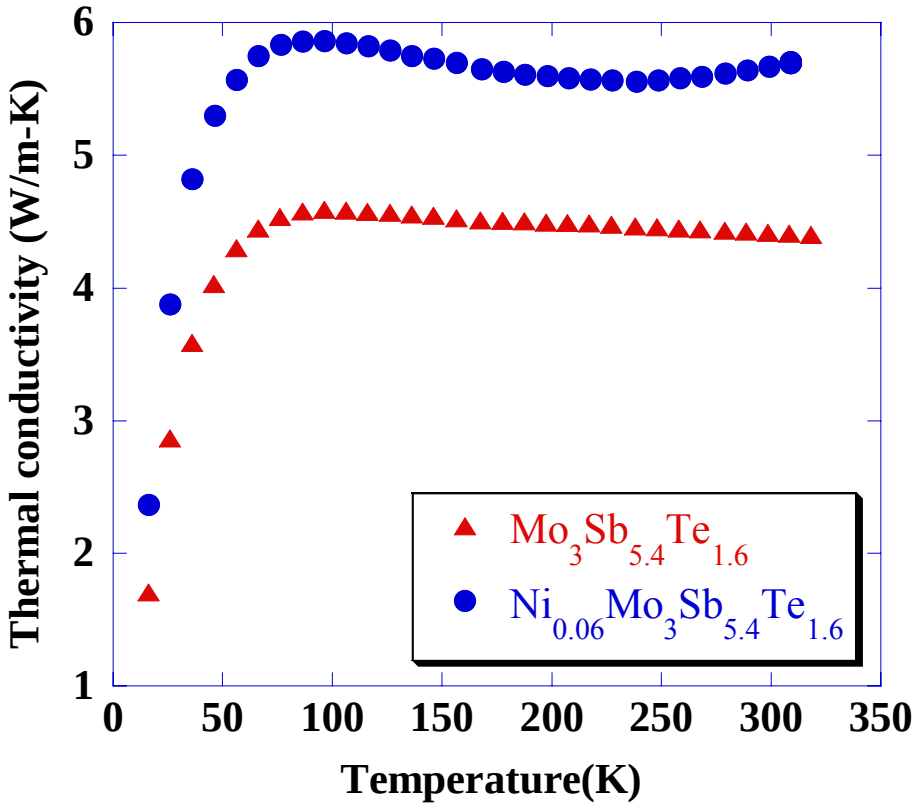


Figure 3.10: Thermal Conductivity of $Mo_3Sb_{5.4}Te_{1.6}$ and $Ni_{0.06}Mo_3Sb_{5.4}Te_{1.6}$

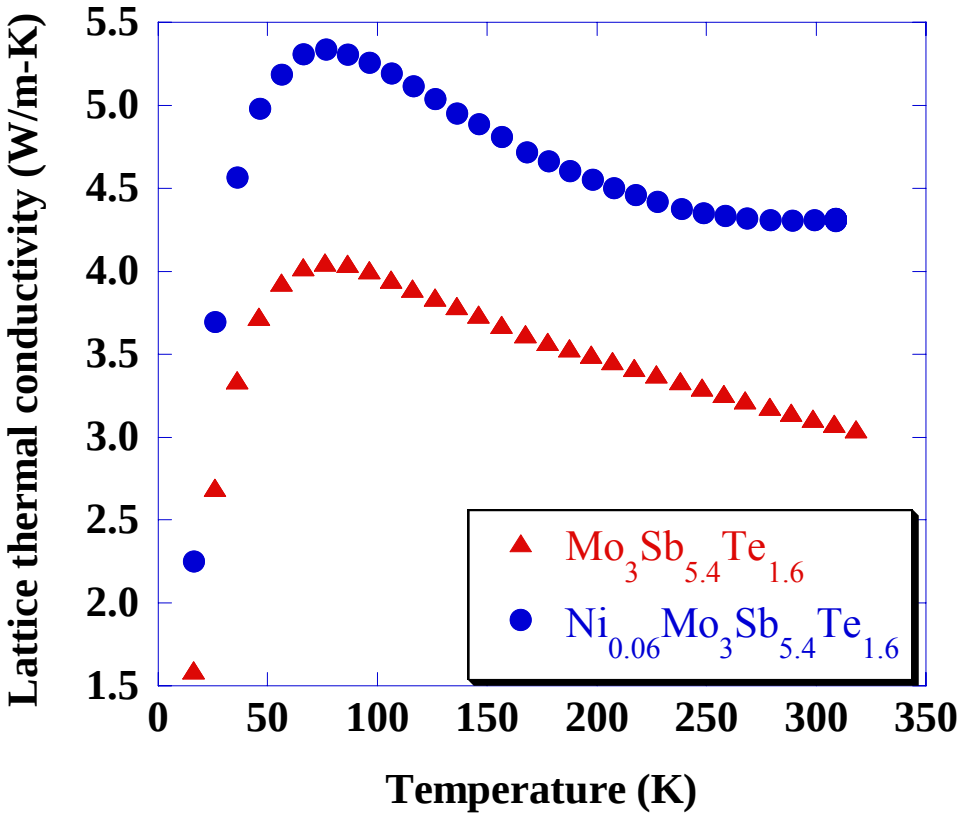


Figure 3.11: Lattice Thermal Conductivity of $Mo_3Sb_{5.4}Te_{1.6}$ and $Ni_{0.06}Mo_3Sb_{5.4}Te_{1.6}$

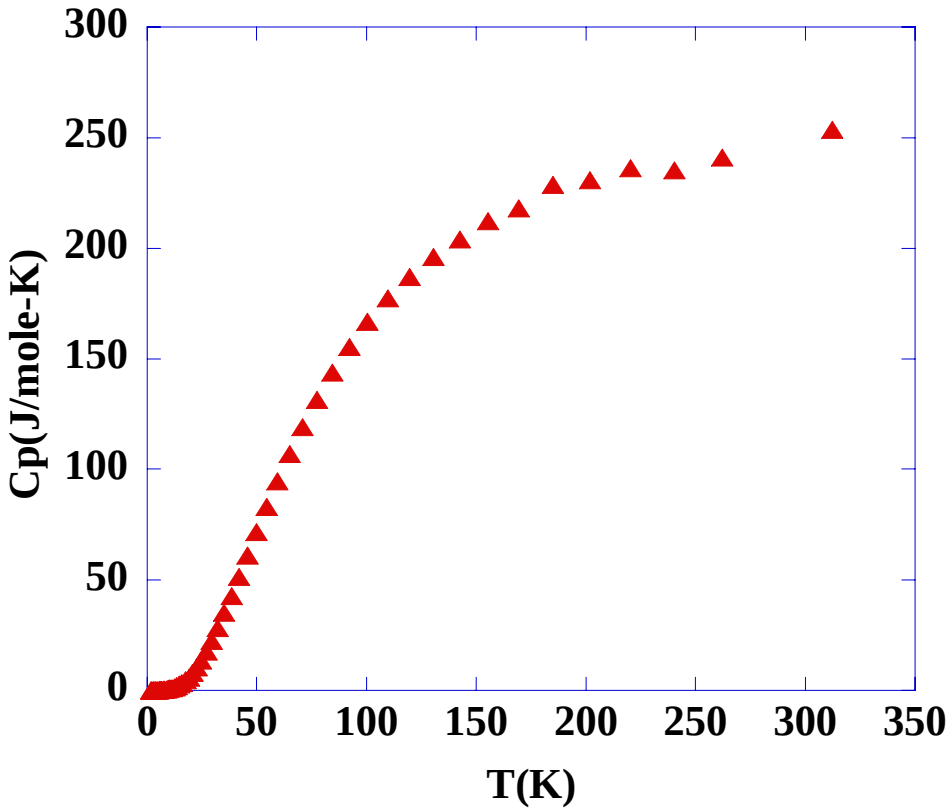


Figure 3.12: Specific Heat of $Mo_3Sb_{5.4}Te_{1.6}$

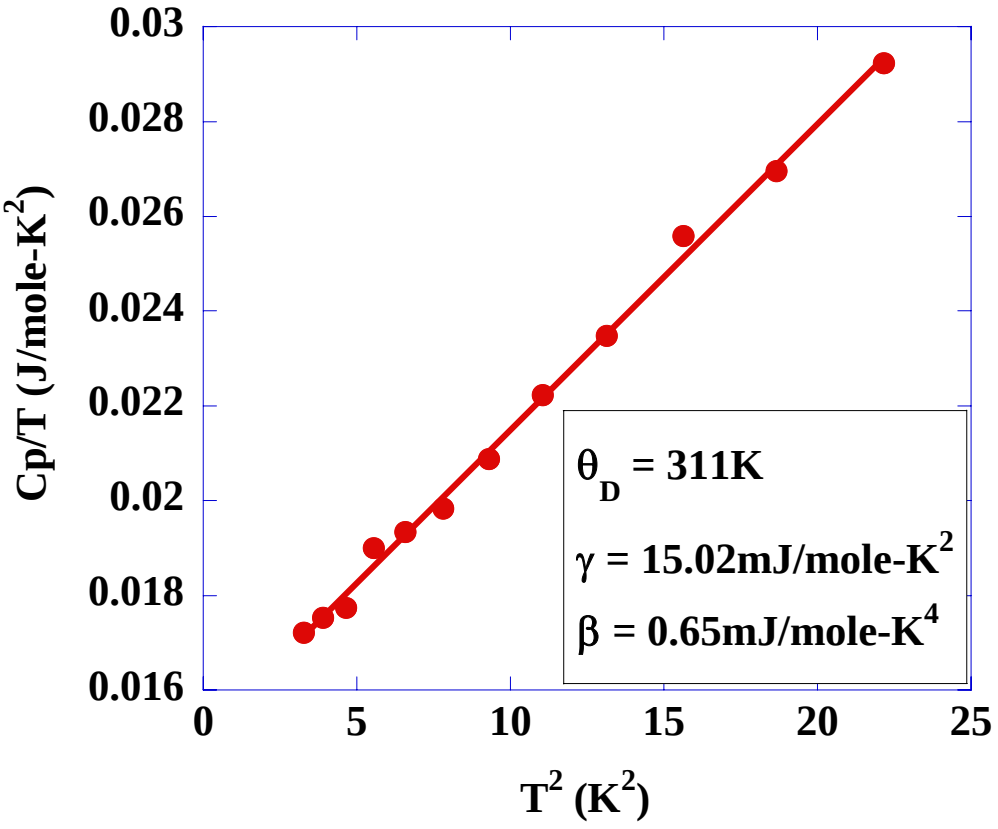


Figure 3.13: Debye Temperature of $Mo_3Sb_{5.4}Te_{1.6}$

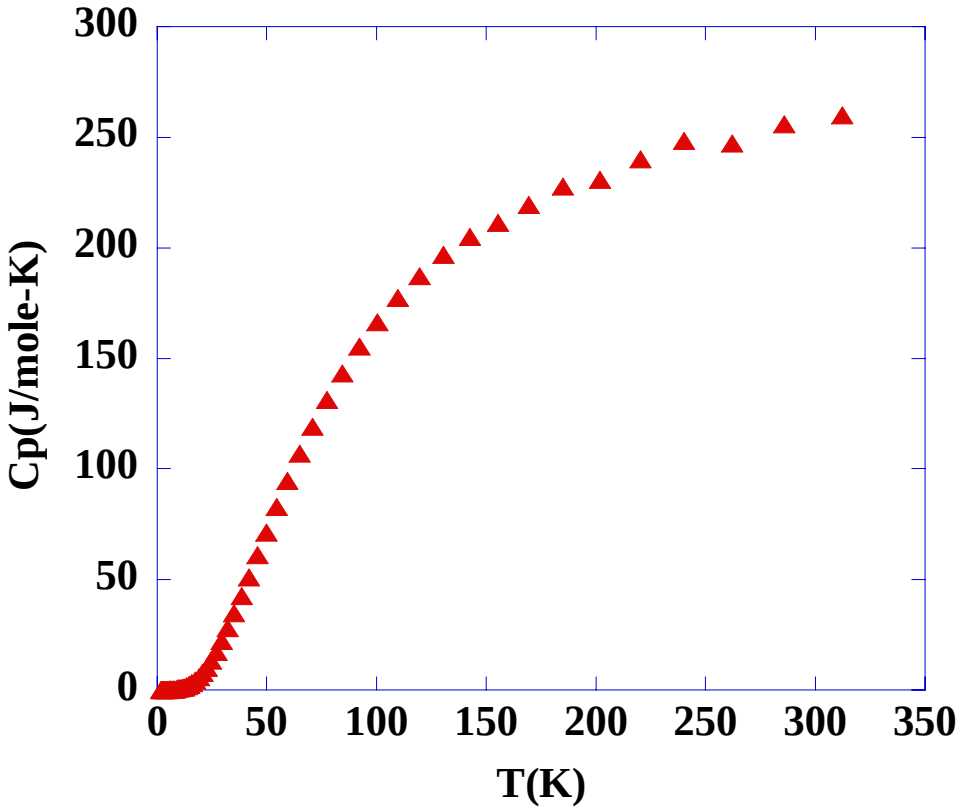


Figure 3.14: Specific Heat of $Ni_{0.06}Mo_3Sb_{5.4}Te_{1.6}$

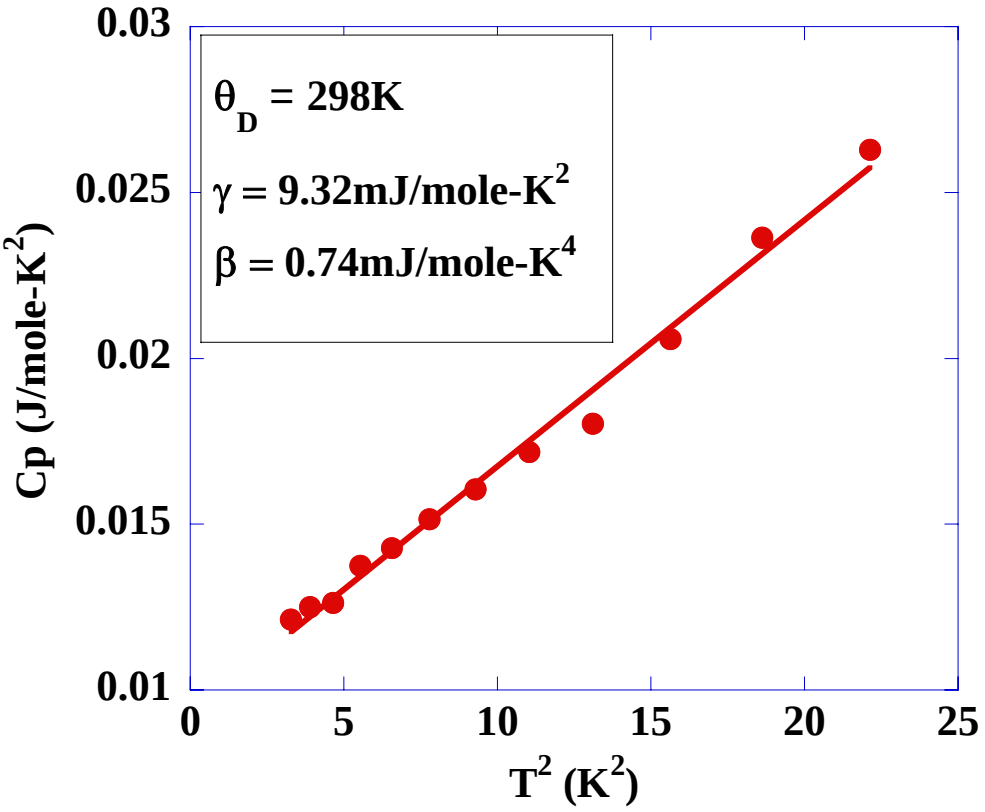


Figure 3.15: Debye Temperature of $Ni_{0.06}Mo_3Sb_{5.4}Te_{1.6}$

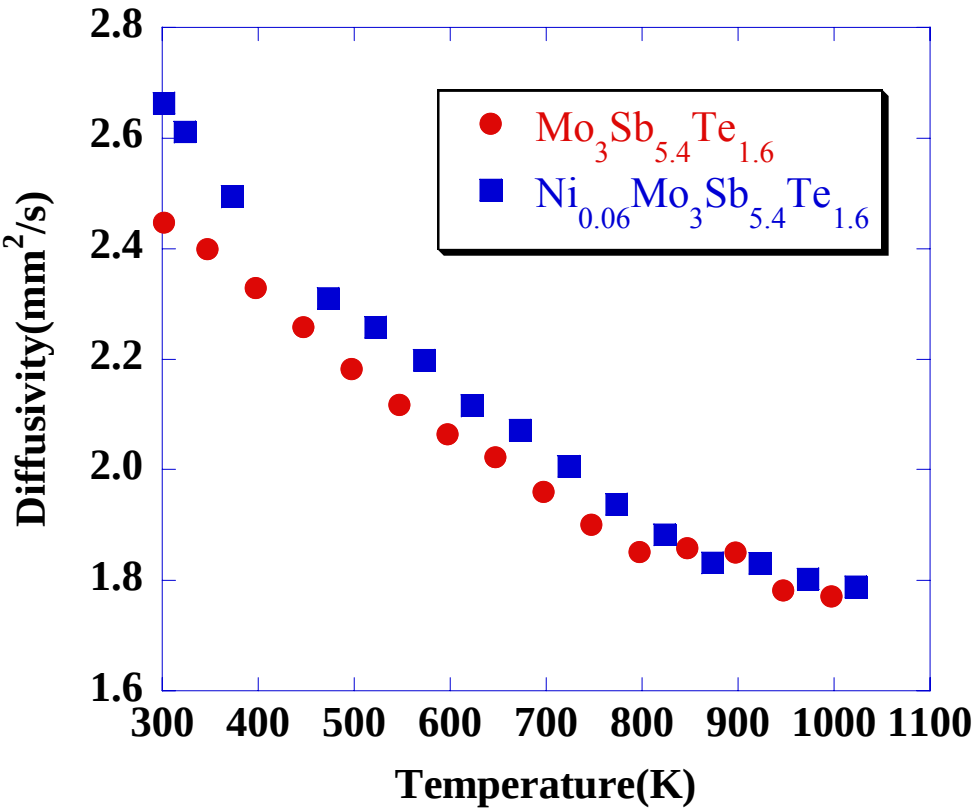


Figure 3.16: Diffusivity of $Mo_3Sb_{5.4}Te_{1.6}$ and $Ni_{0.06}Mo_3Sb_{5.4}Te_{1.6}$

## $Nb_3Sb_2Te_5$

### Band Structure and DOS

From the band structure and DOS (Figure 3.17)[13], the valence band is separated from the conduction band by a forbidden gap in $Nb_3Sb_2Te_5$. Because the lower point of the conduction band and the highest point of the valence band appear at P and H point, respectively, the material may be classified as an indirect semiconductor. The density of states reveals that Nb-d character contributes most to the region close to the gap. The band gap is about 0.9eV, much higher than 0.16-0.26eV (or 6-10kBT) for a thermoelectric material.

The Figure 3.18 shows the CHOP curves of the Nb-Nb and the various interactions between the main group elements.

### Low Temperature Resistivity and Thermopower

The resistivity data is shown is Figure 3.19. When it is converted into the electrical conductivity temperature dependence (Figure 3.20), the data show that the electrical conductivity is increasing with increasing temperature, reaching at $73.89\Omega^{-1}cm^{-1}$ at room temperature. Because the slope is not exponential, $Nb_3Sb_2Te_5$ can be classified as an extrinsic semiconductor. This is in agreement with the electronic structure calculation. [13] The thermopower is increasing with increasing temperature as well (Figure 3.21). From the sigh of the thermopower, the material is decided as n-type material. At 300K, the thermopower is about $29\mu VK^{-1}$, a rather small value for a semiconductor. This also supports that the material is an extrinsic semiconductor.

Carrier Concentration and Hall Mobility

The carrier concentration temperature dependence is shown in Figure 3.22. Comparing to $Mo_3Sb_{5.4}Te_{1.6}$ and $Ni_{0.06}Mo_3Sb_{5.4}Te_{1.6}$, the carrier concentration of $Nb_3Sb_2Te_5$ is lower. The former one is about a few $10^{21}cm^{-3}$, while the latter one is a few $10^{20}cm^{-3}$. This may part of reason of its low electrical conductivity. The mobility is also calculated as in Figure 3.23. It is increasing with decreasing temperature like $Mo_3Sb_{5.4}Te_{1.6}$ and $Ni_{0.06}Mo_3Sb_{5.4}Te_{1.6}$.

Low Temperature Thermal Conductivity

The thermal conductivity, $\kappa$, slowly decreases with increasing temperatures above 60 K, and reaches $5.7 Wm^{-1} K^{-1}$ at 300K (Figure 3.24). The thermoelectric figure-of-merit is defined as $ZT = \alpha^2\sigma T/\kappa$. Its small value of $0.4\times10^{-3}$ at 300K reveals that $Nb_3Sb_2Te_5$ is not a competitive material at any temperature, for at least $ZT$ values around 1 should be approached. For example, $Mo_3Sb_{5.4}Te_{1.6}$ exhibits $ZT = 0.8$ at 1050 K, with a room temperature value of 0.03, i.e. 75 times the value of $Nb_3Sb_2Te_5$.

Specific Heat

The specific heat is shown in Figure 3.25 and the Debye temperature is calculated in Figure 3.26.

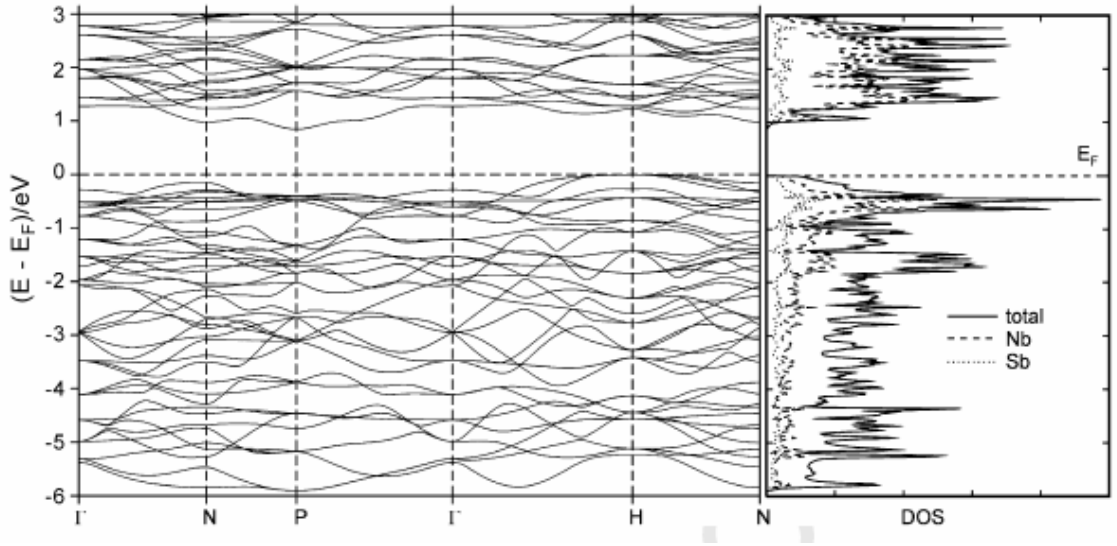


Figure 3.17: Band Structure and Density of States (DOS) of $Nb_3Sb_2Te_5$

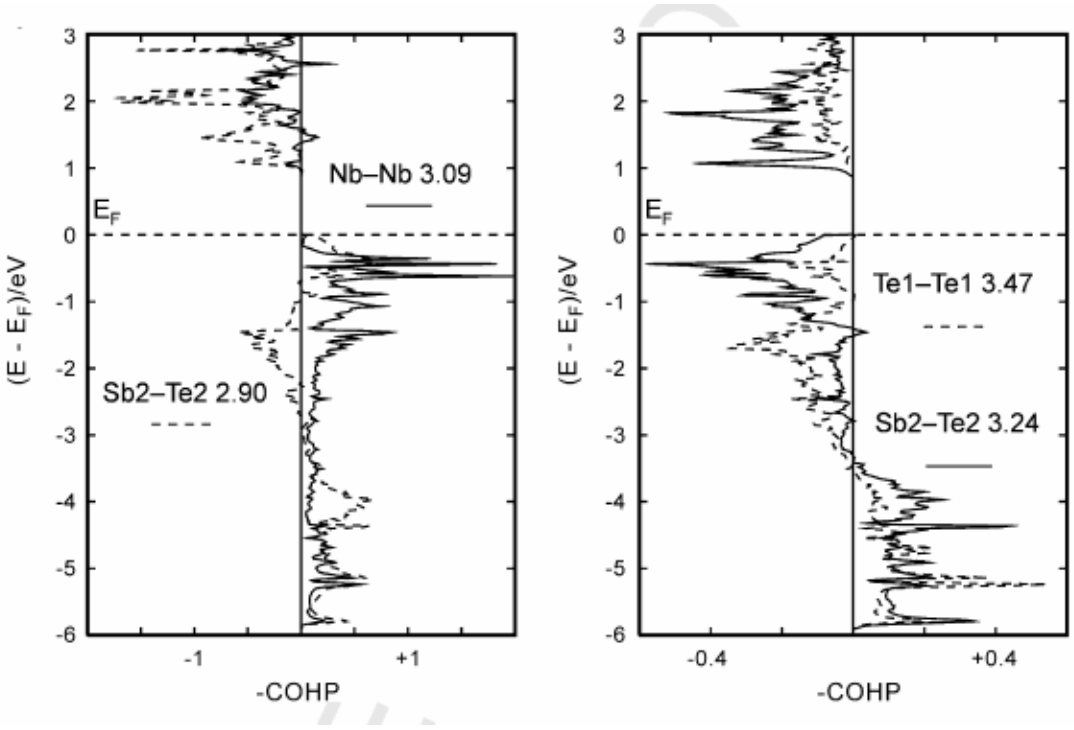


Figure 3.18: Selected Averaged Crystal Orbital Hamilton Population (COHP) Curves

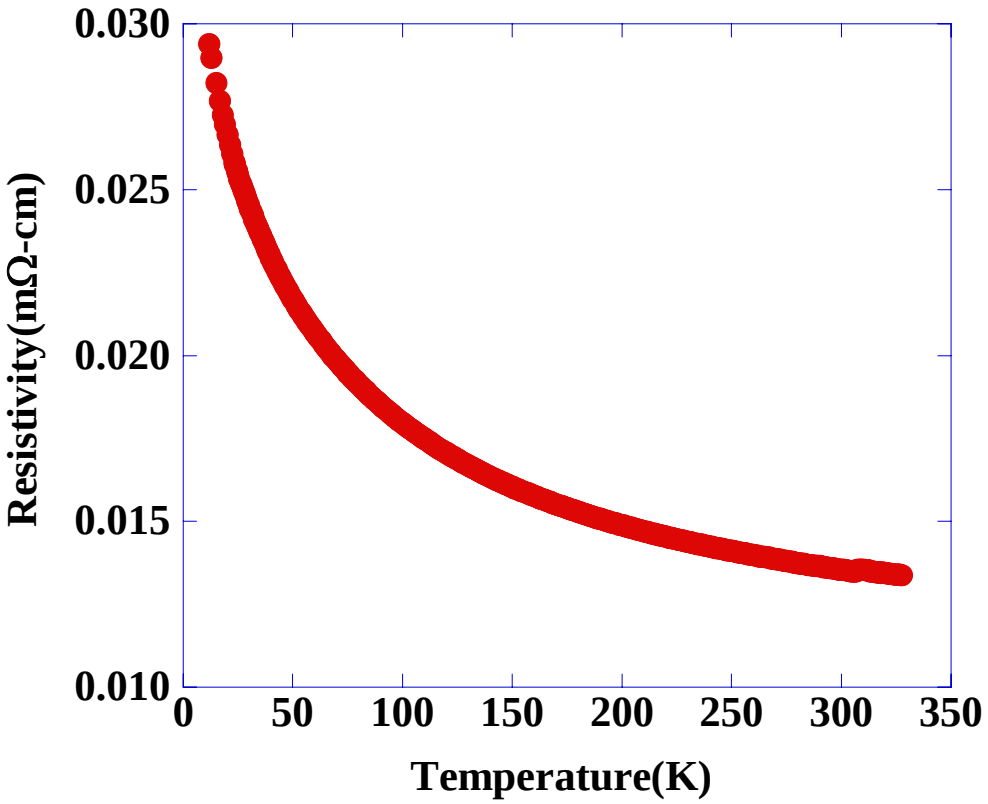


Figure 3.19: Low Temperature Resistivity of $Nb_3Sb_2Te_5$

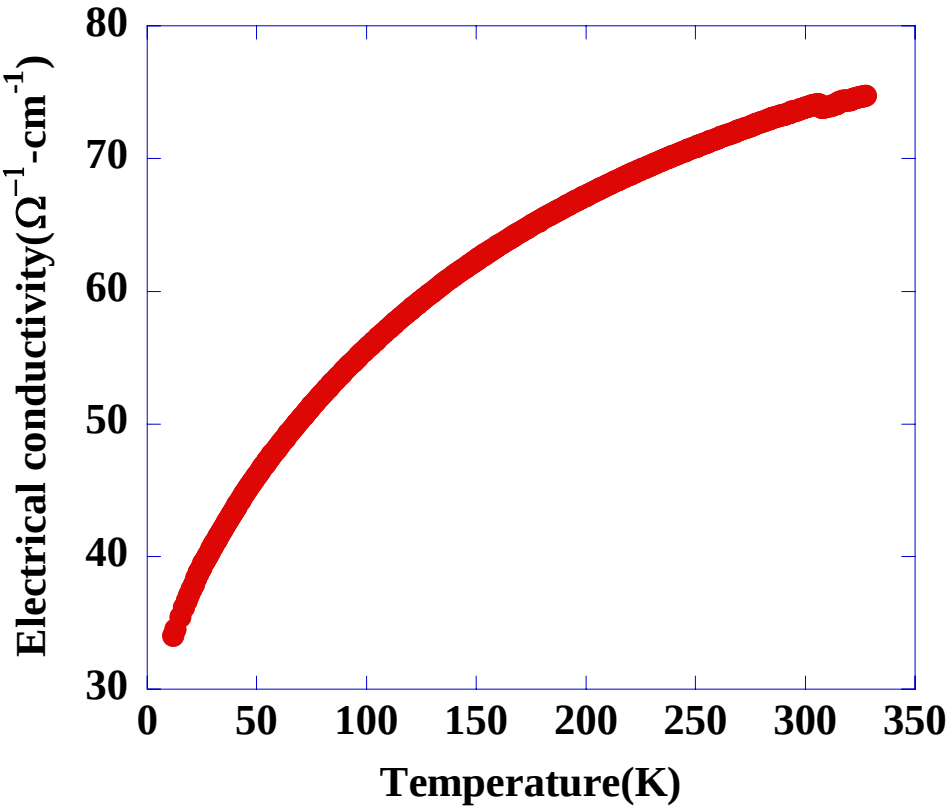


Figure 3.20: Low Temperature Electrical Conductivity of $Nb_3Sb_2Te_5$

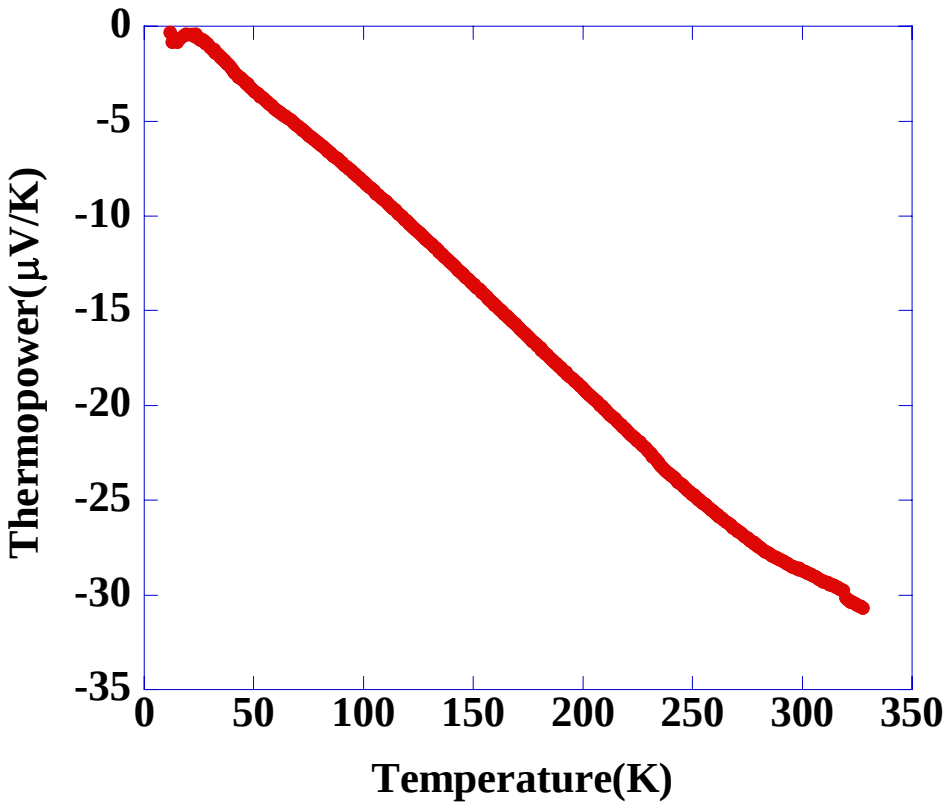


Figure 3.21: Low Temperature Thermopower of $Nb_3Sb_2Te_5$

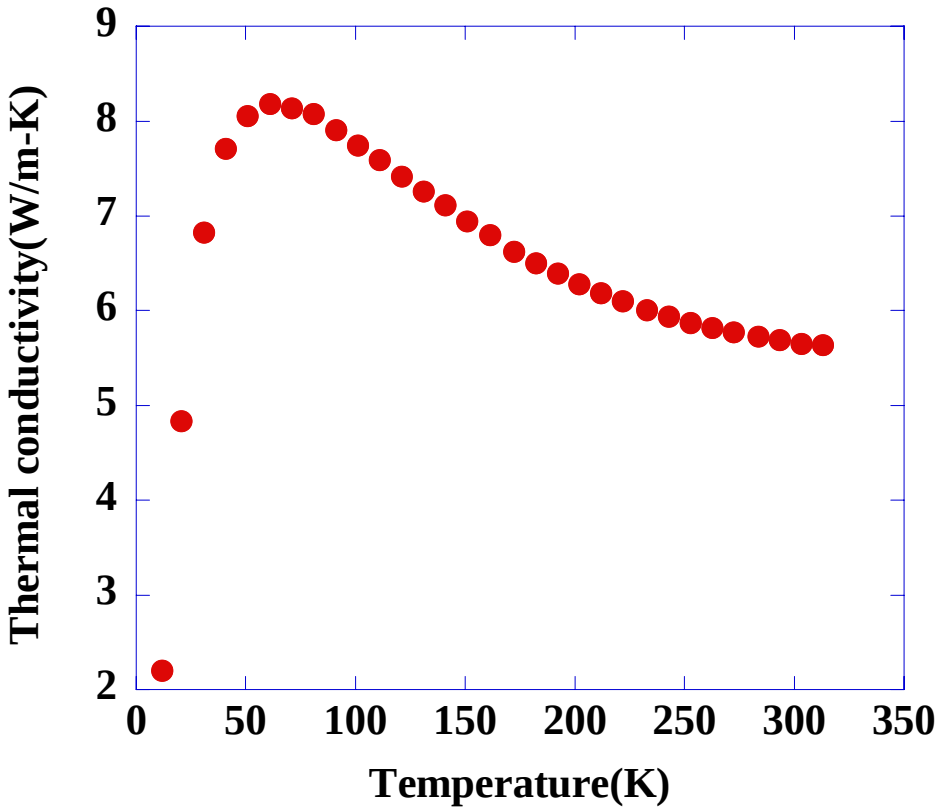


Figure 3.22: Thermal Conductivity of $Nb_3Sb_2Te_5$

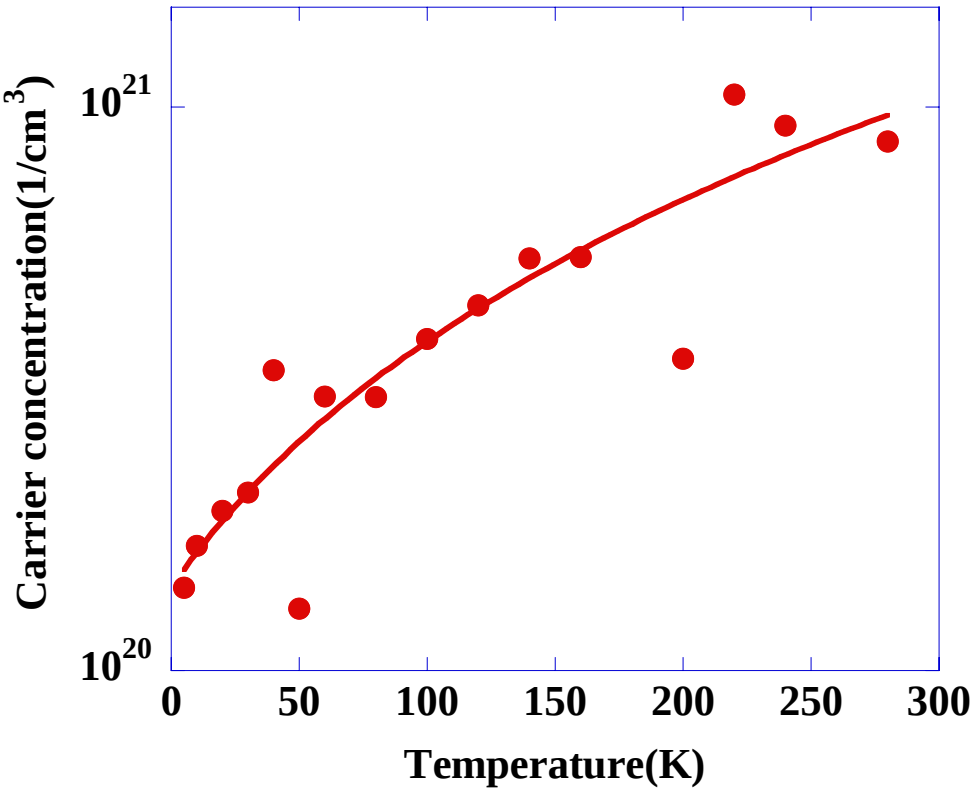


Figure 3.23: Carrier Concentration of $Nb_3Sb_2Te_5$

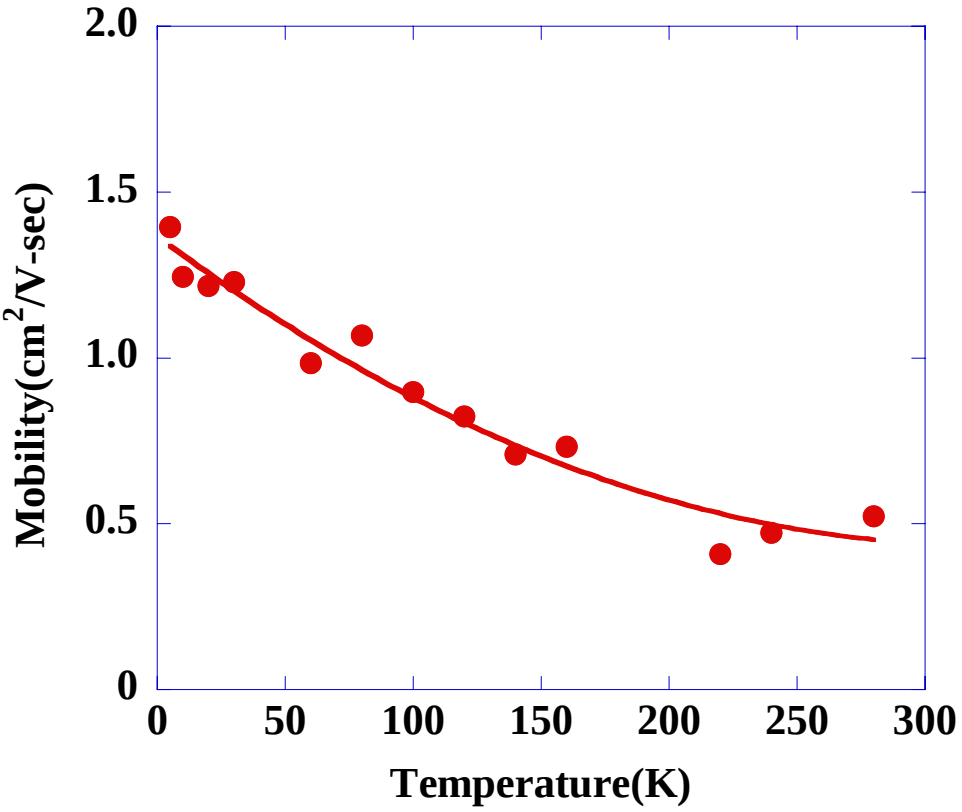


Figure 3.24: Mobility of $Nb_3Sb_2Te_5$

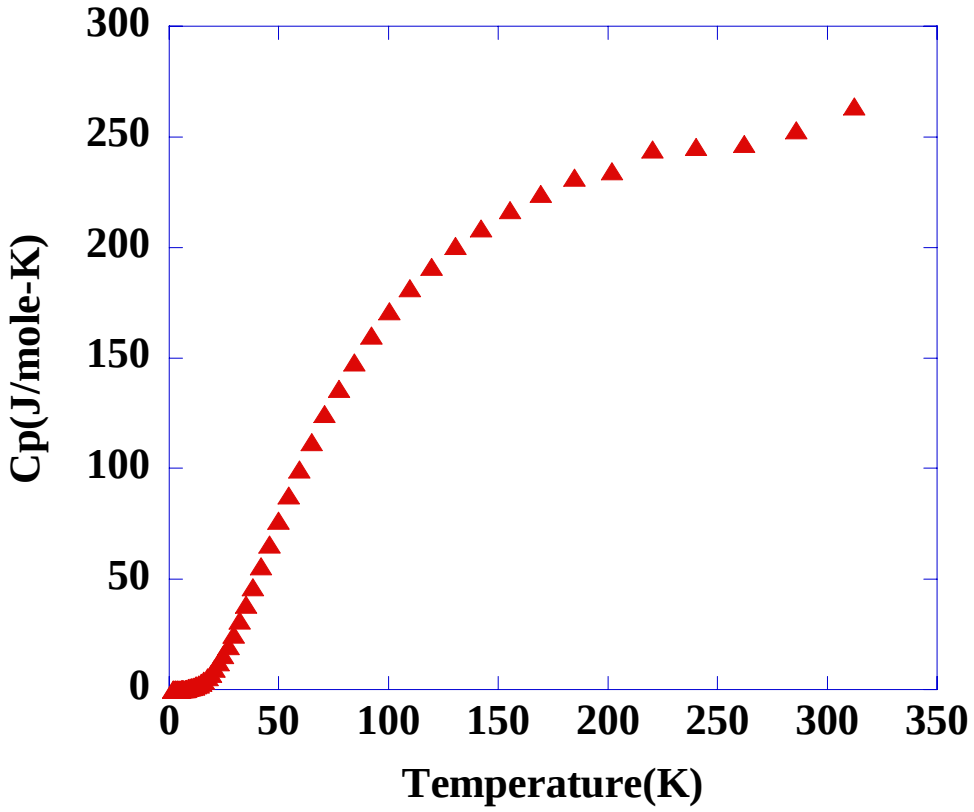


Figure 3.25: Specific Heat of $Nb_3Sb_2Te_5$

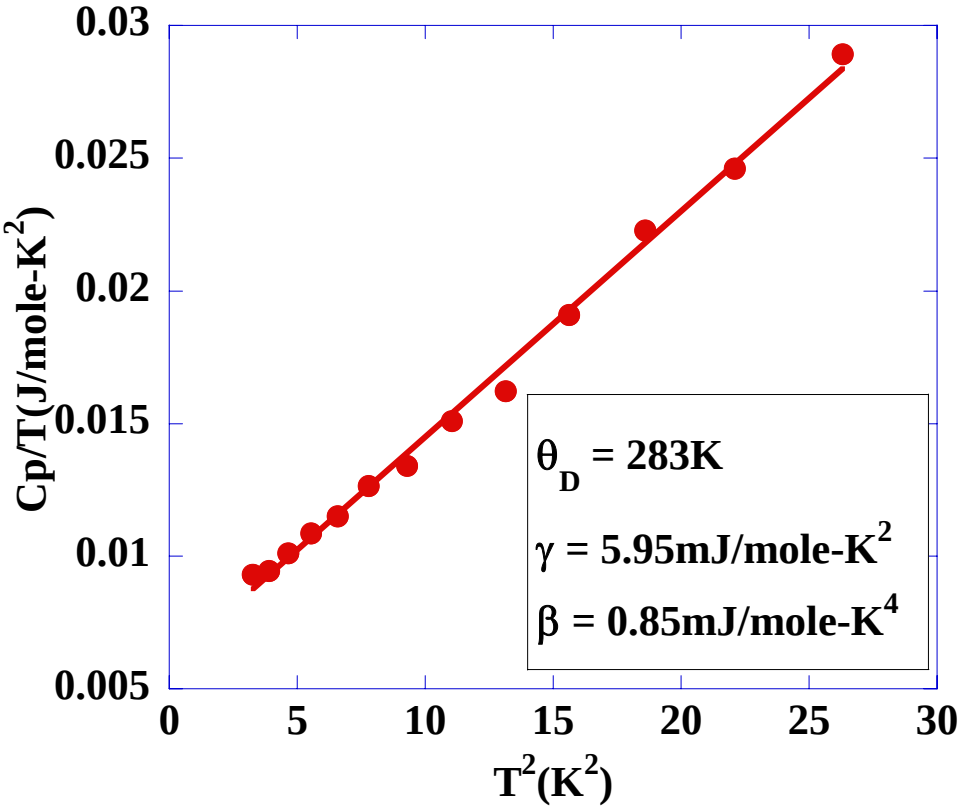


Figure 3.26: Debye Temperature of $Nb_3Sb_2Te_5$

$Re_3GeAs_6$, $Re_3Ge_{0.6}As_{6.4}$ and $Co_{0.05}Re_3Ge_{0.4}As_{6.6}$

X-ray Diffraction

X-ray diffraction was taken for each sample with Rigaku MiniFlex X-ray machine at Clemson. All three samples share the same diffraction patterns as in Figure 3.27, showing there is no secondary phase.

Density of States (DOS)

The density of states (DOS) of $Re_3GeAs_6$ is revealed in Figure 3.28[12]. Compared to the density of state of $Mo_3Sb_5Te_2$, both of them have a band gap at the Fermi level. It is significantly larger in $Re_3GeAs_6$ than that in $Mo_3Sb_5Te_2$. It should be expected to have a larger Seebeck coefficient in $Re_3GeAs_6$. The maximum ZT is expected to be reached at higher temperature, for the optimal temperature of the best thermoelectric efficiency is proportional to the band gap. Moreover, the spikes appear directly above or below the gap in both case, indicating they should have a large Seebeck coefficient, which is proportional to the first derivative of the DOS. This is from Mott equation:

$$S = \frac{\pi^2 {k_B}^2}{3e} T \frac{\partial[\ln \sigma(E)]}{\partial E}_{E=E_F} , \tag{3.5}$$

where, $k_B$ is Boltzmann constant, $e$ is charge of an electron, $E_F$ is Fermi energy, and $\sigma$ is electrical conductivity.

Low Temperature Resistivity and Thermopower

From the thermopower data in Figure 3.29, it is shown that all the materials, $Re_3GeAs_6$, $Re_3Ge_{0.6}As_{6.4}$ and $Co_{0.05}Re_3Ge_{0.4}As_{6.6}$ are *n*-type materials, in contrast to the *p*-type thermoelectric $Mo_3Sb_{5.4}Te_{1.6}$. In each case, the Seebeck coefficient increases steadily, approximately linearly with increasing temperatures, reaching $-67\mu VK^{-1}$, $-72\mu VK^{-1}$ and $-59\mu VK^{-1}$, respectively at 300 K. For comparison, we determined the thermopower of $Mo_3Sb_{5.4}Te_{1.6}$ at 300K $+49\mu VK^{-1}$. The larger Seebeck coefficient of the Re sample correlates nicely with the larger band gap. For $Re_3Ge_{0.6}As_{6.4}$ and $Mo_3Sb_{5.4}Te_{1.6}$, the observation of *n*- and *p*-type follows directly from electron counting, as the former exhibits more than 55 valence-electrons per formula unit, namely 55.4,and the latter less (54.6). Adding Co to the Re sample causes a decrease of the thermopower[12].

As expected from the density of states, $Re_3Ge_{0.6}As_{6.4}$ and $Re_3GeAs_6$ have significantly smaller electrical conductivity (1090 $\Omega^{-1}cm^{-1}$ and 760 $\Omega^{-1}cm^{-1}$ at 300 K) than $Mo_3Sb_{5.4}Te_{1.6}$, determined to be 1780 Ω–1cm–1 by us. In either case, the electrical resistivity increases slowly with increasing temperature (Figure 3.30), typical for degenerate semiconductors. The sample with Co has a higher electrical conductivity (1198 $\Omega^{-1}cm^{-1}$ at 300K). When it is normalized, the resistivity of the three materials shows the same temperature dependence.

Carrier Concentration and Hall Mobility

From the carrier concentration data (Figure 3.31), we see that the carrier concentration does not depend strongly on the temperature. The sample $Re_3GeAs_6$ has much higher carrier concentration than the sample $Re_3Ge_{0.6}As_{6.4}$.

$Re_3Ge_{0.6}As_{6.4}$ has 55.4 valence-electrons per formula unit, more than 55 of $Re_3GeAs_7$. Based on rigid band approximation, more electrons will raise the Fermi lever higher. In this case, since the Fermi level for $Re_3GeAs_6$ is at the top of the valence band, it will be lifted into the conduction band. In this way, we expect the carrier concentration would increase by $0.4/V[\mathring{A}^3] = 0.4/665.75\mathring{A}^3 = 6.01\times10^{20}/cm^3$. However from our experimental data, we find the carrier concentration is decreased from $Re_3GeAs_6$ to $Re_3Ge_{0.6}As_{6.4}$. This indicates that our assumption of a rigid band is wrong. Co doped sample has higher carrier concentration than that of both $Re_3GeAs_6$ and $Re_3Ge_{0.6}As_{6.4}$. If Co adopts 4+ valences, it will help to increase the carrier concentration $1.2\times10^{21}/cm^3$ from $Re_3Ge_{0.6}As_{6.4}$ to $Co_{0.05}Re_3Ge_{0.4}As_{6.6}$. The experimental increase is $1.4\times10^{21}/cm^3$ at 10K, which is close to the calculated one, indicating Co introduces more carriers to the material and help to increase the carrier concentration. This may be part of reason for the higher electrical conductivity of $Co_{0.05}Re_3Ge_{0.4}As_{6.6}$.

The mobility of the three samples are shown in Figure 3.32. Like the carrier concentration, the mobility does not strongly depend on temperature. However different from the carrier concentration, $Re_3Ge_{0.6}As_{6.4}$ has the highest mobility and $Co_{0.05}Re_3Ge_{0.4}As_{6.6}$ has the lowest one.

High Temperature Resistivity and Thermopower

Figure 3.33 shows the high temperature resistivity. The three samples share the same trend at higher temperature. The resistivity increases with increasing temperature until about 600K, and then decreases after that. Meanwhile, the thermopower increases with

increasing temperature over the entire range of temperature (Figure 3.34). So the power factor would keep increasing after 600K.

Low Temperature Thermal Conductivity

For the all three samples, the thermal conductivity, κ, increases from 20 K to about 100 K, and reaches a plateau above 100K (Figure 3.35). The temperature dependence is similar to that of $Mo_3Sb_{5.4}Te_{1.6}$. At 300K, the thermal conductivity values for $Re_3Ge_{0.6}As_{6.4}$, $Re_3GeAs_6$ and $Co_{0.05}Re_3Ge_{0.4}As_{6.6}$ are 4.2$Wm^{-1}K^{-1}$, 3.9$Wm^{-1}K^{-1}$ and 6.9$Wm^{-1}K^{-1}$ respectively. For $Mo_3Sb_{5.4}Te_{1.6}$, it has the value 4.4 $Wm^{-1}K^{-1}$, similar to the value of $Re_3Ge_{0.6}As_{6.4}$ and $Re_3GeAs_6$. $Co_{0.05}Re_3Ge_{0.4}As_{6.6}$ has a higher value than others. The thermal conductivity κ is comprised of the lattice thermal conductivity, $\kappa_L$, and the electronic thermal conductivity, $\kappa_E$. Via the Wiedemann-Franz relationship ($\kappa_E = L_0\sigma T$) we calculate $\kappa_E$, where the electrical conductivity, σ, can be derived as the reciprocal of the resistivity ρ, $L_0$ is the Lorentz number, $L_0 = 2.45 \cdot 10^{-8} V^2K^{-2}$. By subtracting the electronic contribution $\kappa_E$ from the thermal conductivity κ, we obtain very comparable lattice contribution for the three samples, namely 3.3 $Wm^{-1}K^{-1}$ for $Re_3GeAs_6$, 3.4 $Wm^{-1}K^{-1}$ for $Re_3Ge_{0.6}As_{6.4}$ (Figure 3.36), and 3.5 $Wm^{-1}K^{-1}$ for $Mo_3Sb_{5.4}Te_{1.6}$ and a much higher value 6.0 $Wm^{-1}K^{-1}$ for $Co_{0.05}Re_3Ge_{0.4}As_{6.6}$. In this way we can conclude that the differences in the thermal conductivity of $Re_3GeAs_6$, $Re_3Ge_{0.6}As_{6.4}$ and $Mo_3Sb_{5.4}Te_{1.6}$ largely stem from the different electronic contributions, not surprisingly, as the structures, bonding and molar masses of these materials are very similar. Sample $Co_{0.05}Re_3Ge_{0.4}As_{6.6}$ has a much higher value 6.0 $Wm^{-1}K^{-1}$, indicating Co failed to be a rattler. It is very possible for Co to form interstitial bonding with the parent material to help to densify the

material. In this way it helps to increase the lattice thermal conductivity like the Ni in $Ni_{0.06}Mo_3Sb_{5.4}Te_{1.6}$.

Specific Heat

The specific heat for $Re_3GeAs_6$, $Re_3Ge_{0.6}As_{6.4}$ and $Co_{0.05}Re_3Ge_{0.4}As_{6.6}$ are given in Figure 3.37, Figure 3.39 and Figure 3.41. The Debye temperature is calculated as in Figure 3.38, Figure 3.40 and Figure 3.42. The Debye temperature is corresponding to the highest frequency of phonon. Usually the higher Debye temperature, the higher lattice thermal conductivity is. Here we find the three samples follow the above statement. For $Re_3GeAs_6$: Debye temperature is 294K, the lattice thermal conductivity is 3.30 $Wm^{-1}K^{-1}$; For $Re_3Ge_{0.6}As_{6.4}$, Debye temperature is 319.02K, the lattice thermal conductivity is 3.38 $Wm^{-1}K^{-1}$; For $Co_{0.05}Re_3Ge_{0.4}As_{6.6}$, Debye temperature is 374K , the lattice thermal conductivity is 6.05$Wm^{-1}K^{-1}$ .

High Temperature Thermal Diffusivity

The thermal diffusivity of $Re_3GeAs_6$ and $Re_3Ge_{0.6}As_{6.4}$ and $Co_{0.05}Re_3Ge_{0.4}As_{6.6}$ is shown in Figure 3.43. Since the three samples have similar density and the specific heat is not strongly dependent on the temperature, the thermal diffusivity is the dominant factor which affects the high temperature thermal conductivity. Here we find there is not a significant difference among the three samples' thermal diffusivities, indicating at the high temperature they have similar thermal conductivity.

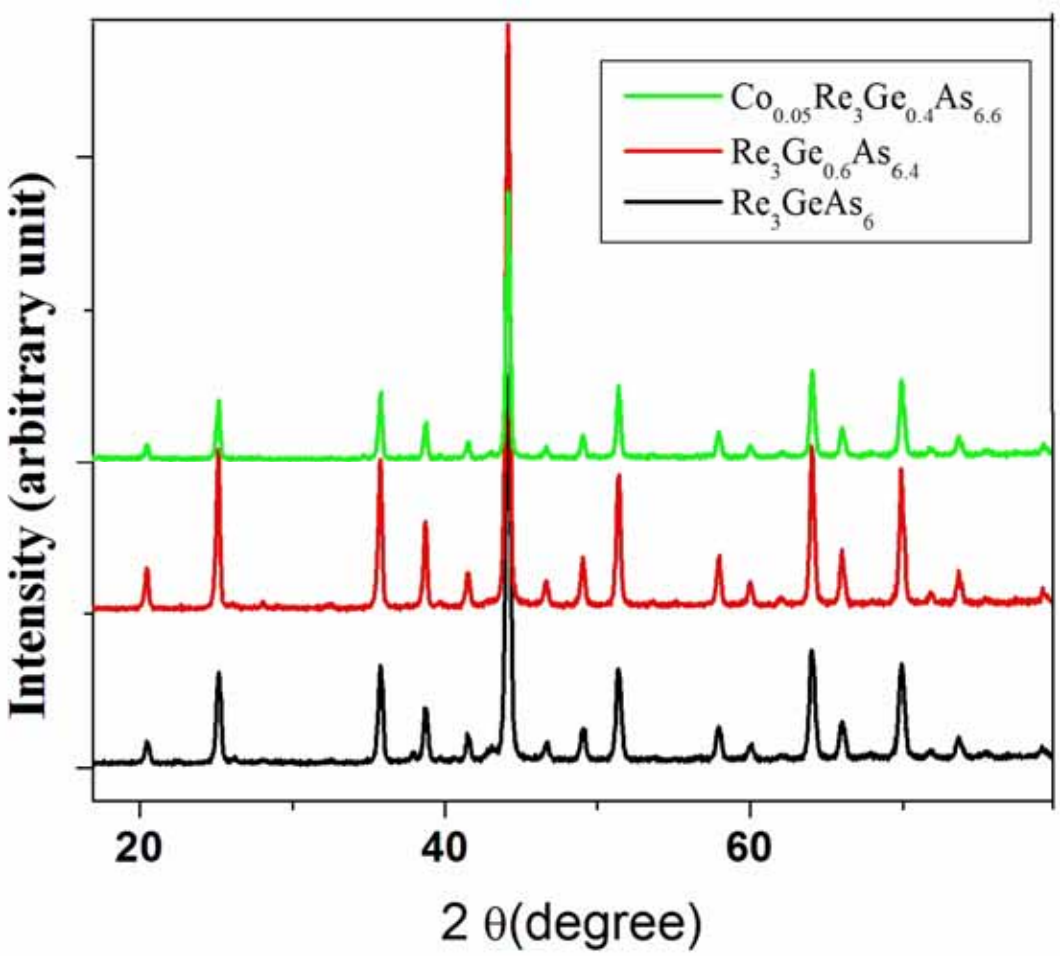


Figure 3.27: X-ray Pattern of $Re_3GeAs_6$, and $Re_3Ge_{0.6}As_{6.4}$ and $Co_{0.05}Re_3Ge_{0.4}As_{6.6}$

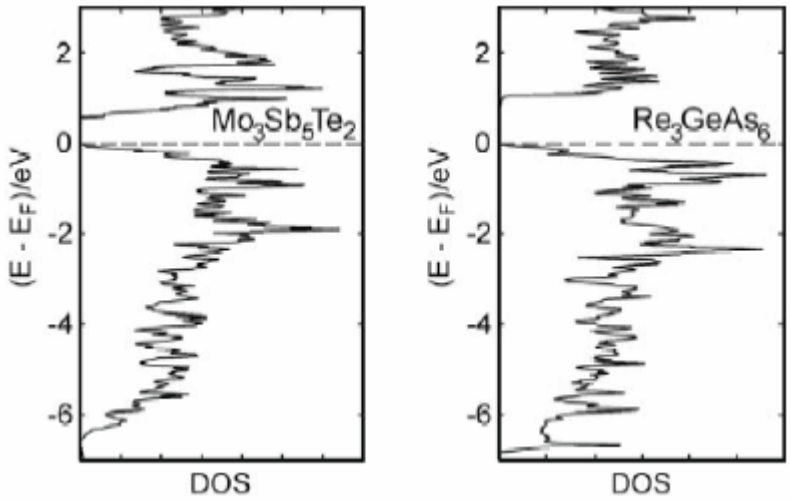


Figure 3.28: Density of States of $Re_3GeAs_6$ (Compared to the Density of State of $Mo_3Sb_5Te_2$)

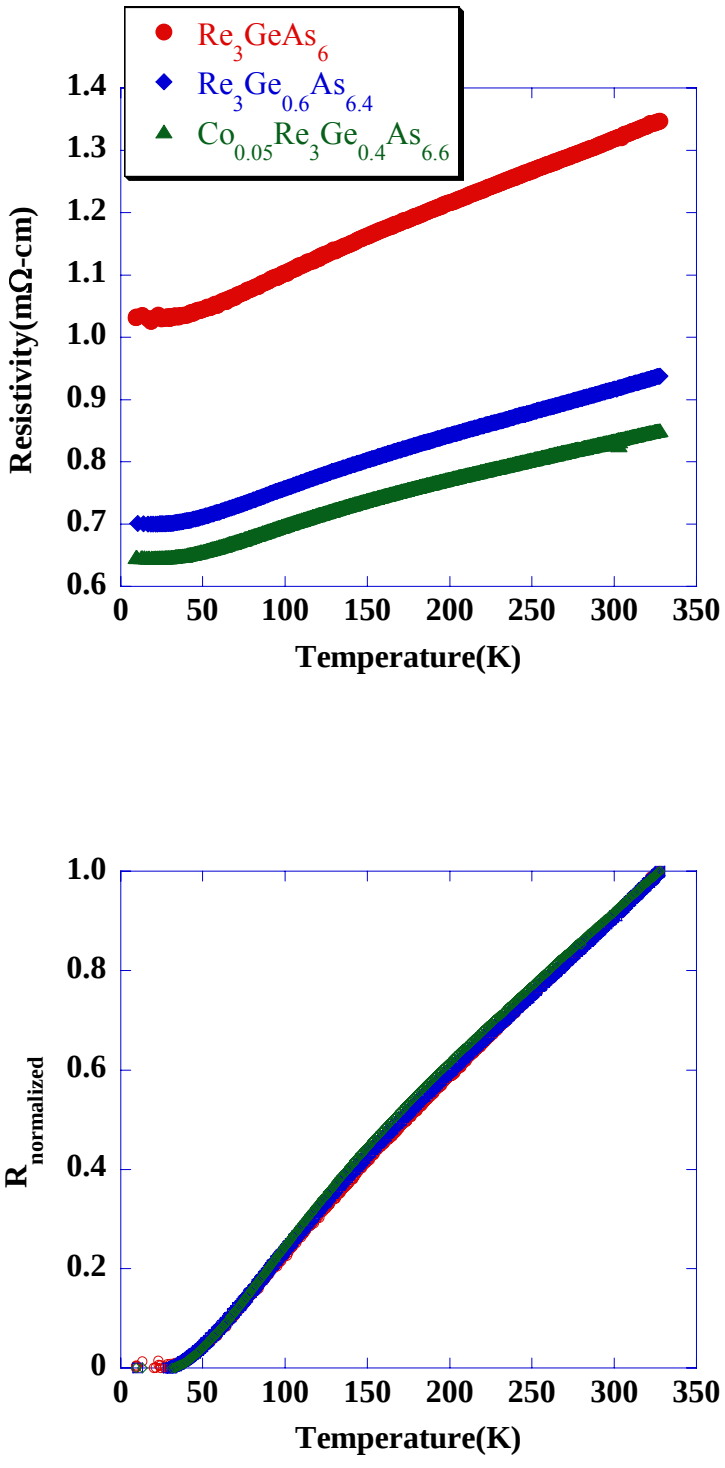


Figure 3.29: Low Temperature Resistivity of $Re_3GeAs_6$ and $Re_3Ge_{0.6}As_{6.4}$ and $Co_{0.05}Re_3Ge_{0.4}As_{6.6}$

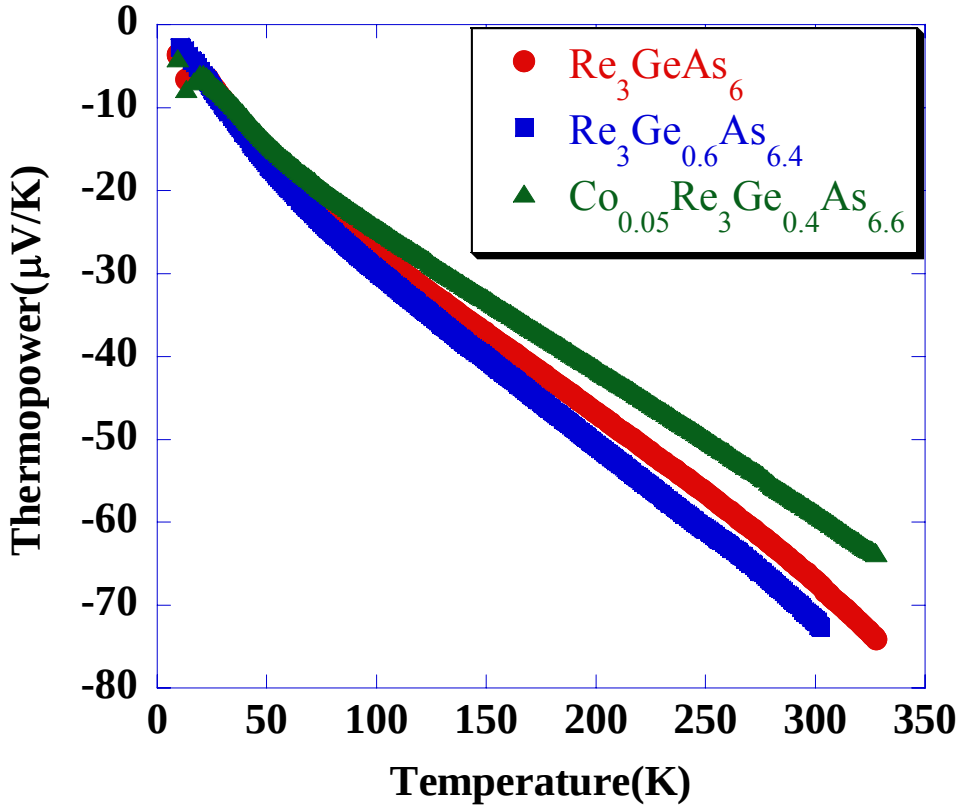


Figure 3.30: Low Temperature Thermopower of $Re_3GeAs_6$, $Re_3Ge_{0.6}As_{6.4}$ and $Co_{0.05}Re_3Ge_{0.4}As_{6.6}$

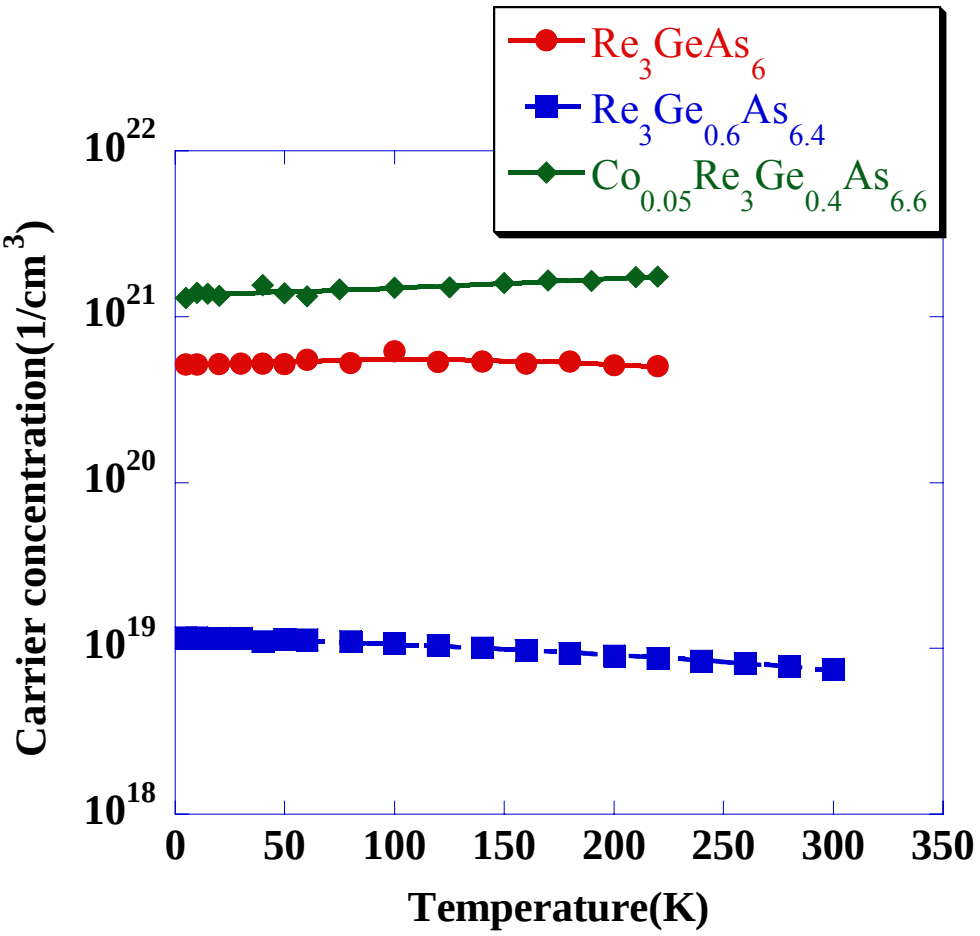


Figure 3.31: Carrier Concentration of $Re_3GeAs_6$, $Re_3Ge_{0.6}As_{6.4}$ and $Co_{0.05}Re_3Ge_{0.4}As_{6.6}$

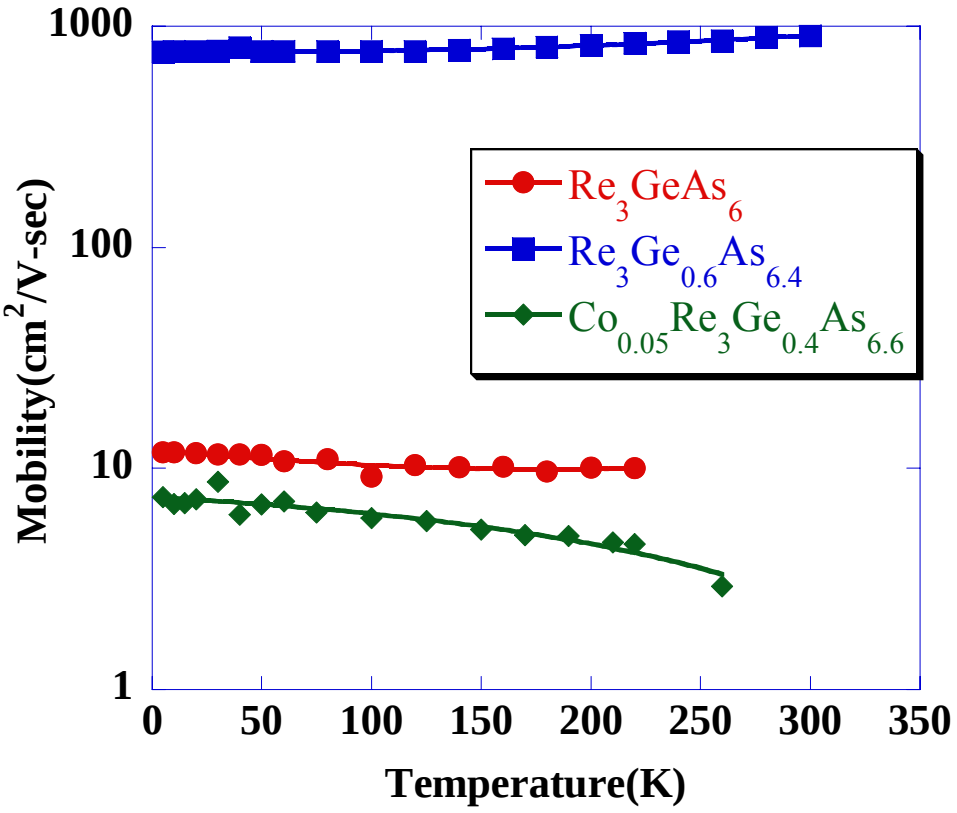


Figure 3.32: Mobility of $Re_3GeAs_6$, $Re_3Ge_{0.6}As_{6.4}$ and $Co_{0.05}Re_3Ge_{0.4}As_{6.6}$

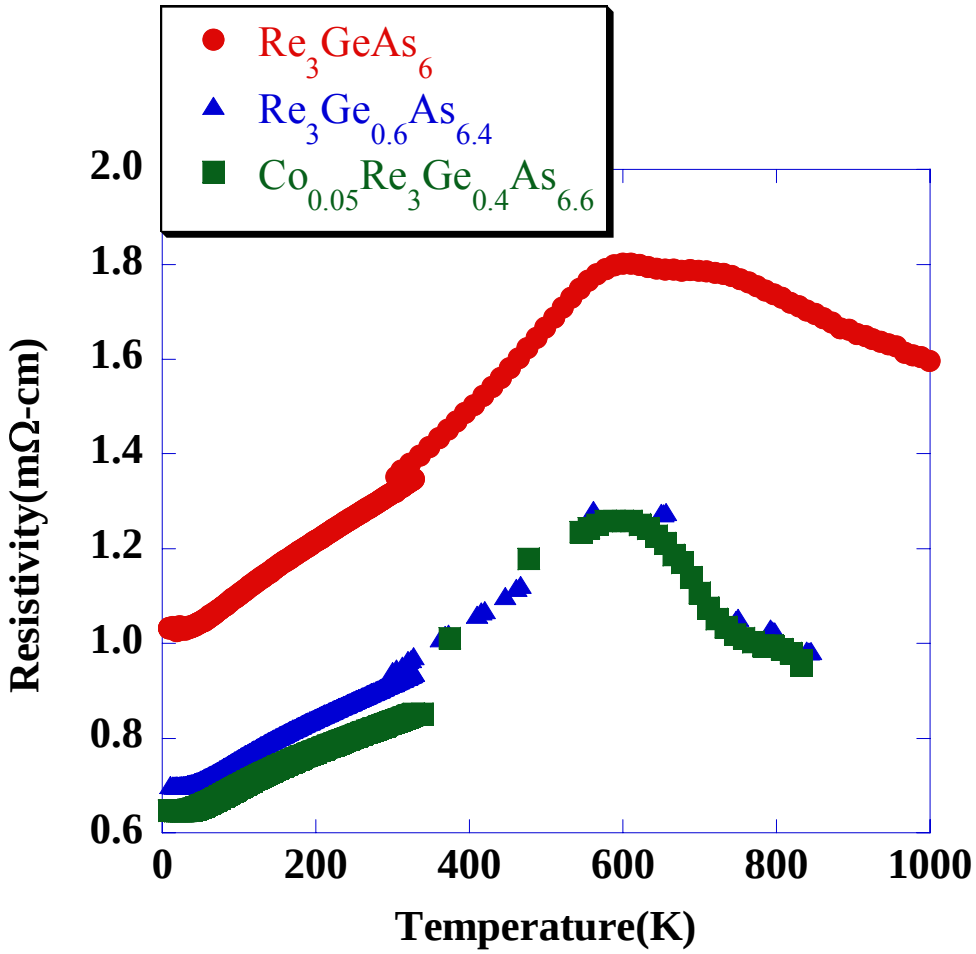


Figure 3.33: High Temperature Resistivity of $Re_3GeAs_6$, $Re_3Ge_{0.6}As_{6.4}$ and $Co_{0.05}Re_3Ge_{0.4}As_{6.6}$

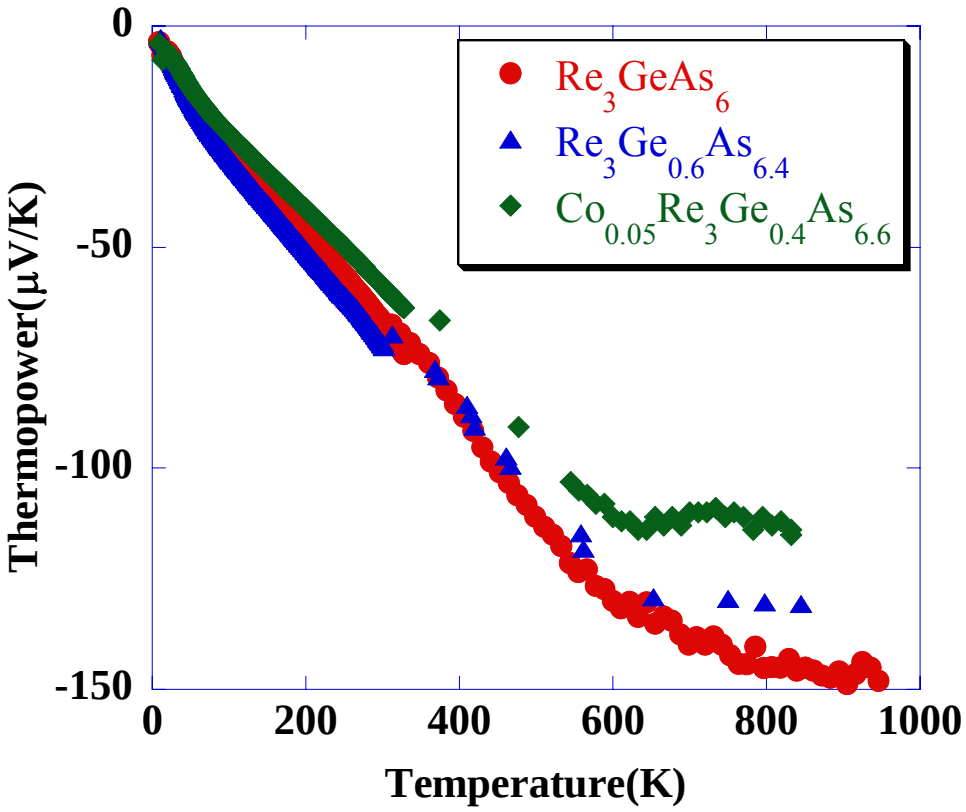


Figure 3.34: High Temperature Thermopower of $Re_3GeAs_6$, $Re_3Ge_{0.6}As_{6.4}$ and $Co_{0.05}Re_3Ge_{0.4}As_{6.6}$

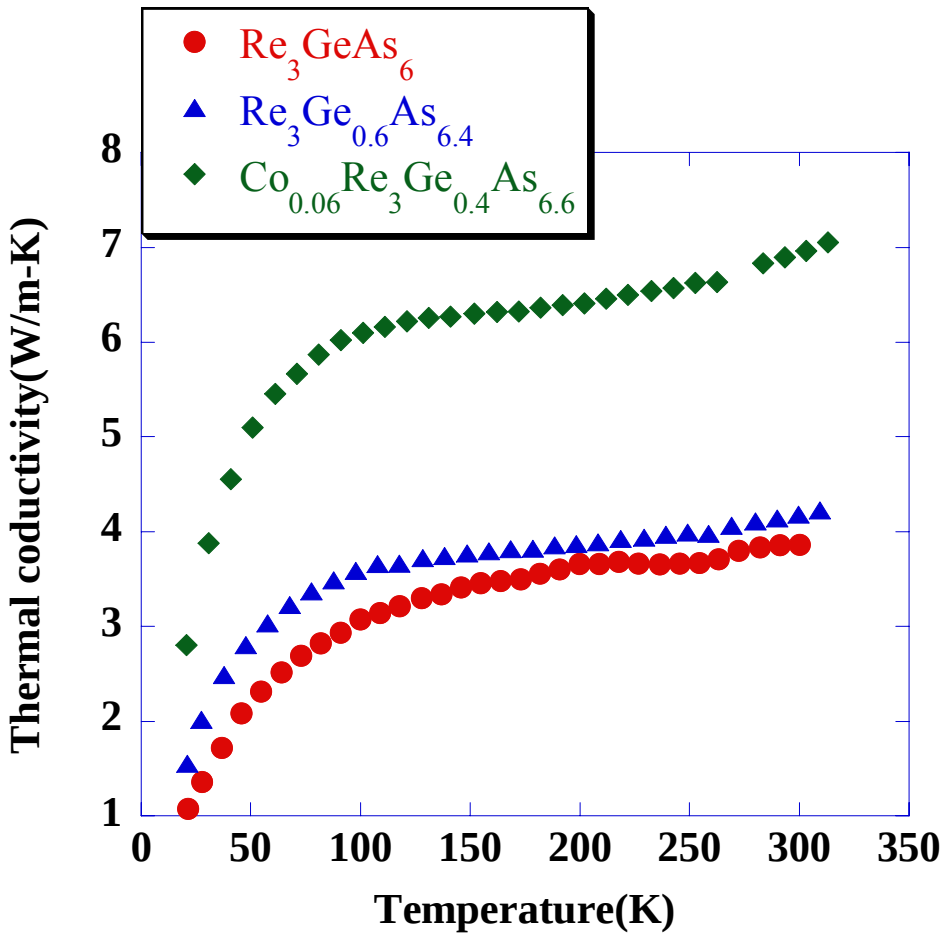


Figure 3.35: Thermal Conductivity of $Re_3GeAs_6$, $Re_3Ge_{0.6}As_{6.4}$ and $Co_{0.05}Re_3Ge_{0.4}As_{6.6}$

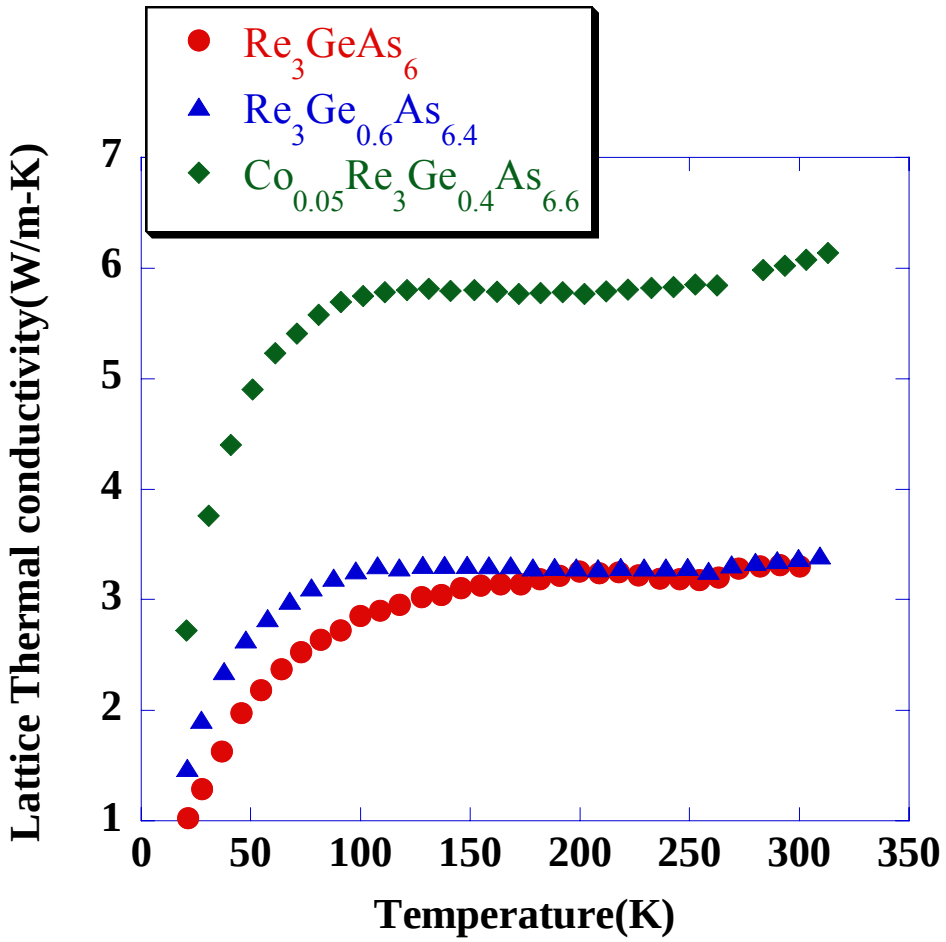


Figure 3.36: Lattice Thermal Conductivity of $Re_3GeAs_6$, $Re_3Ge_{0.6}As_{6.4}$ and $Co_{0.05}Re_3Ge_{0.4}As_{6.6}$

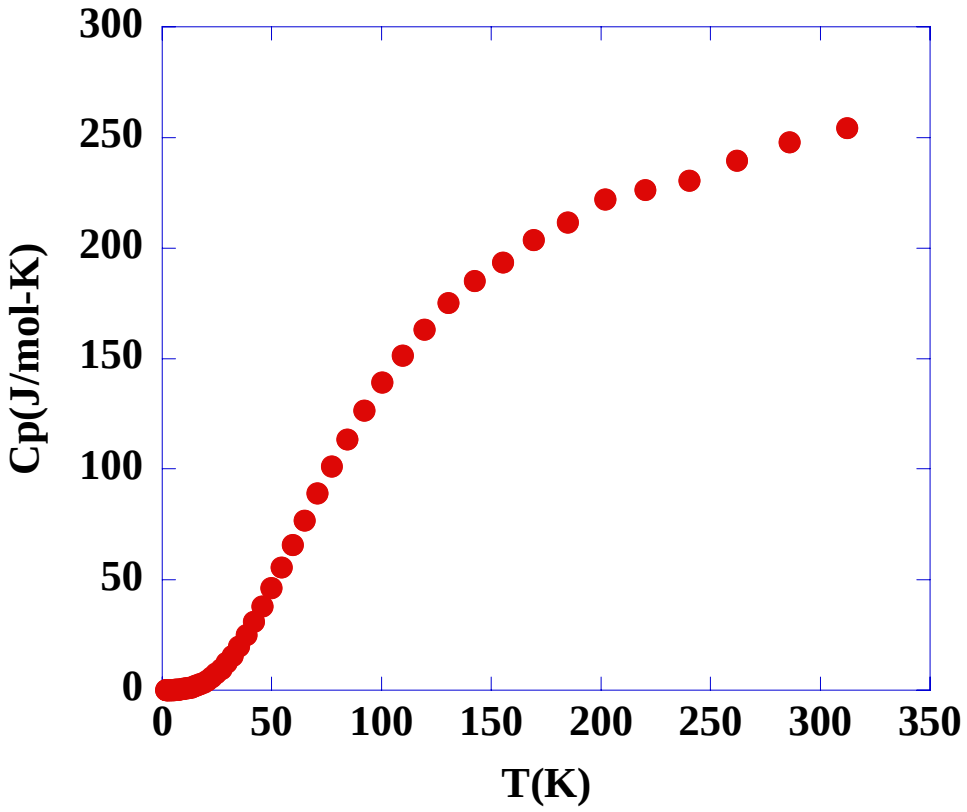


Figure 3.37: Specific Heat of $Re_3GeAs_6$

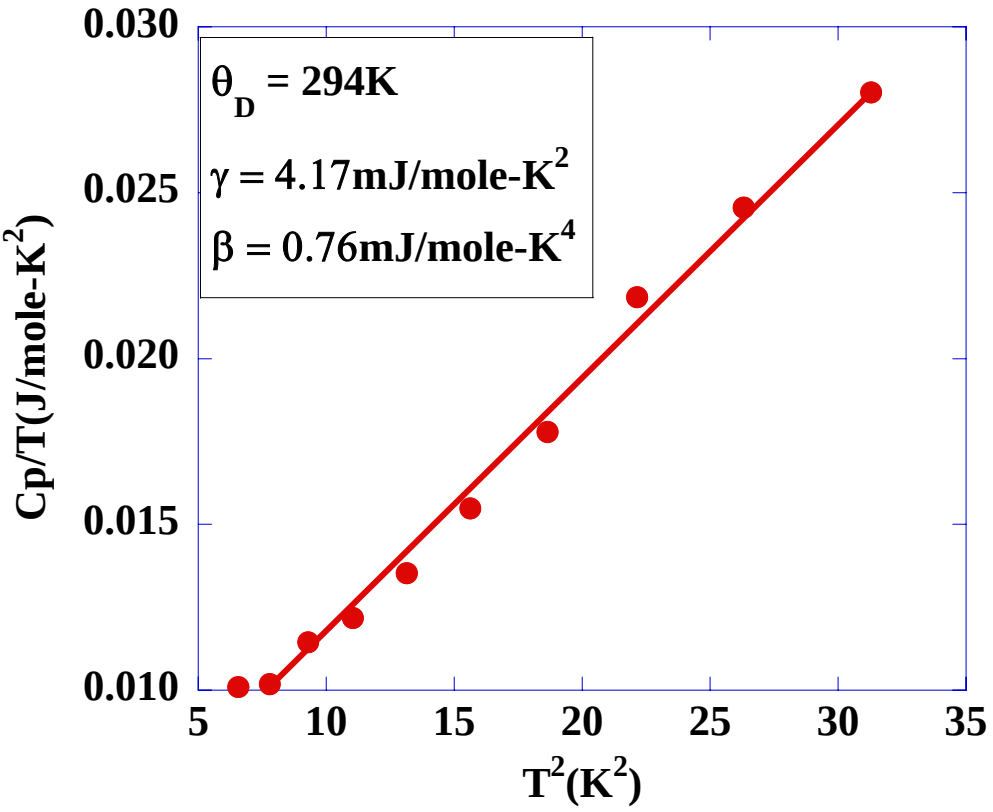


Figure 3.38: Debye Temperature of $Re_3GeAs_6$

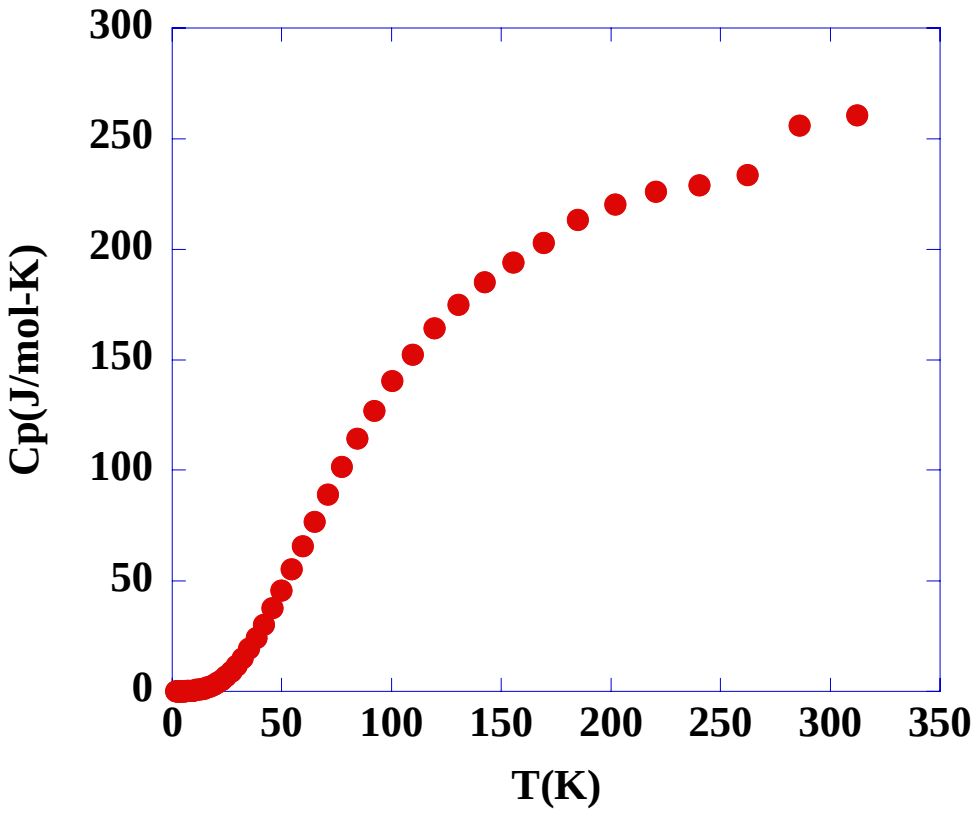


Figure 3.39: Specific Heat of $Re_3Ge_{0.6}As_{6.4}$

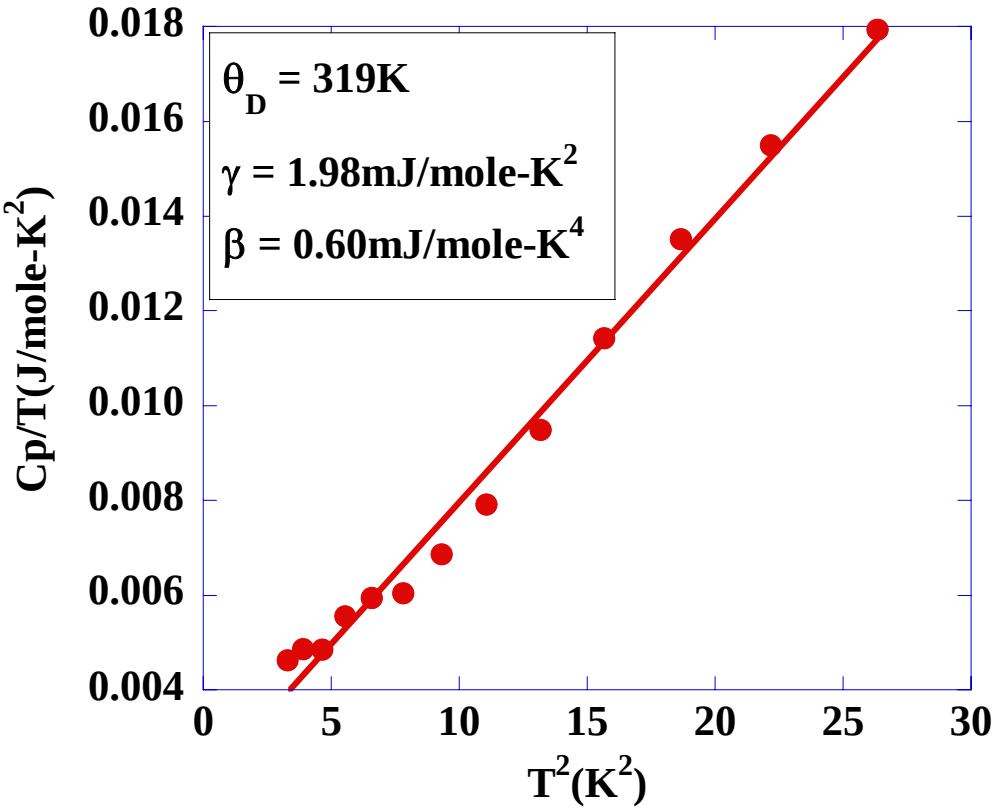


Figure 3.40: Debye Temperature of $Re_3Ge_{0.6}As_{6.4}$

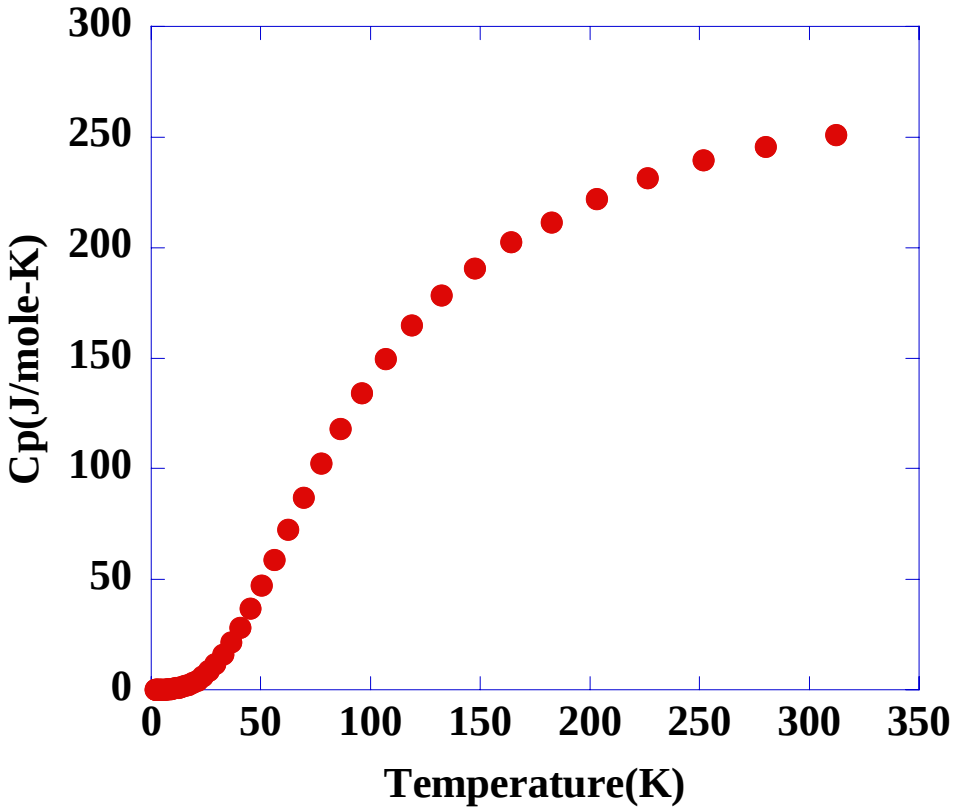


Figure 3.41: Specific Heat of $Co_{0.05}Re_3Ge_{0.4}As_{6.6}$

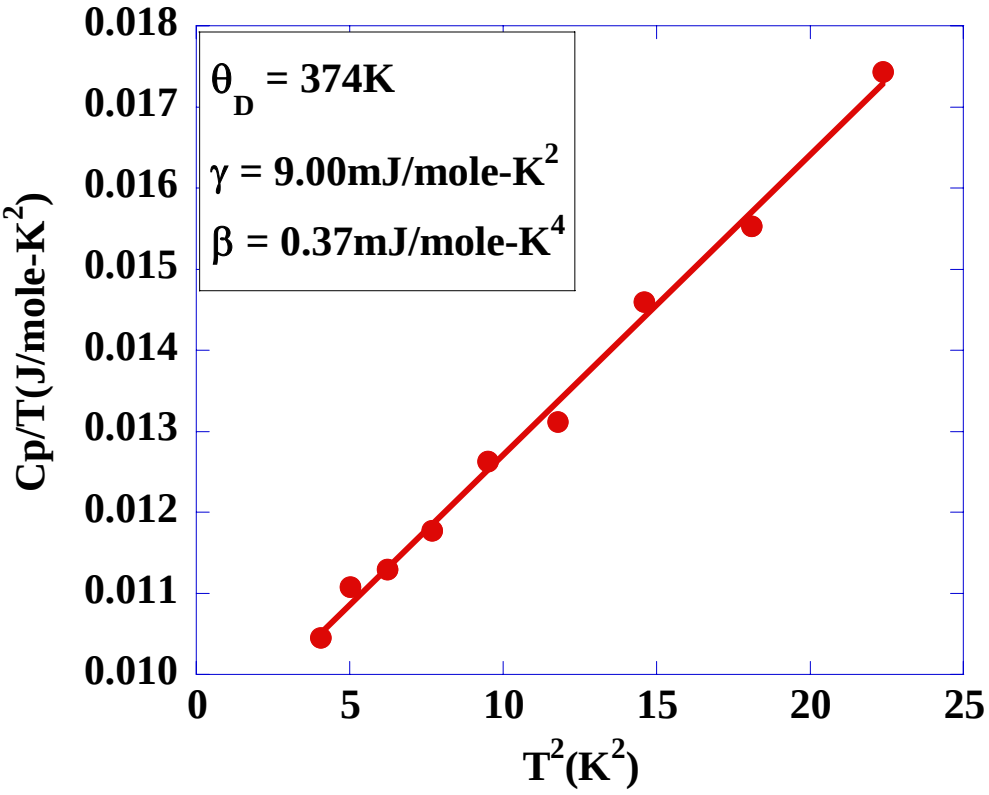


Figure 3.42: Debye Temperature of $Co_{0.05}Re_3Ge_{0.4}As_{6.6}$

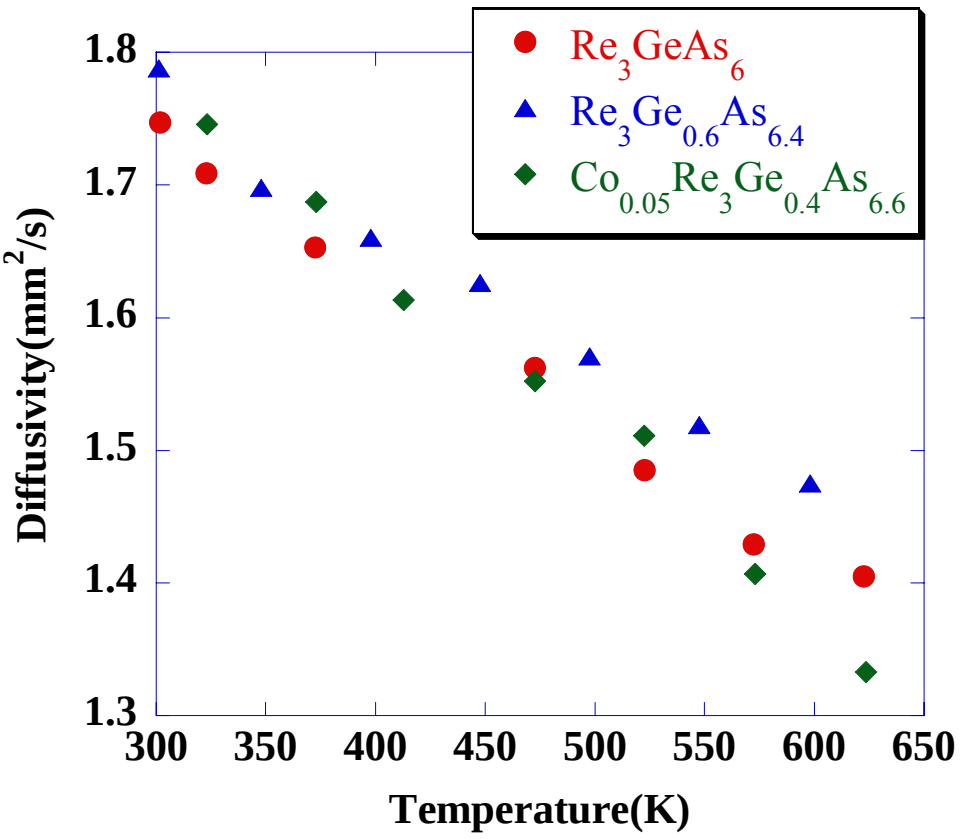


Figure 3.43: Thermal Diffusivity of $Re_3GeAs_6$, $Re_3Ge_{0.6}As_{6.4}$ and $Co_{0.05}Re_3Ge_{0.4}As_{6.6}$

# IV SUMMARY

We studied the thermoelectric properties of several $Ir_3Ge_7$ typed materials. $Mo_3Sb_{5.4}Te_{1.6}$ shows a p-type degenerate semiconductor behavior. In an attempt to use Ni as a rattler in order to improve the thermoelectric *figure-of-merit*, ZT failed, due to an increased thermal conductivity, contrary to what was expected. However Ni-doping increased the power factor from $0.13 Wm^{-1}K^{-1}$ to $0.23\ Wm^{-1}K^{-1}$ at 300K. Though the thermal conductivity is increased, the ZT is improved from 0.03 to 0.04. $Nb_3Sb_5Te_2$ is a n-type material. Because of its very low electrical conductivity and thermopower, it is not a competitive thermoelectric material. $Re_3GeAs_6$ and $Re_3Ge_{0.6}As_{6.4}$ have similar properties. Both of them are n- type. The ZT value of $Re_3Ge_{0.6}As_{6.4}$ is significantly larger than determined for $Mo_3Sb_{5.4}Te_{1.6}$, e.g. ZT(300 K) = 0.041 vs. 0.029. Co doping does not help to reduce thermal conductivity. Although adding Co causes the resistivity to decrease, the thermopower is also decreased. As a result, the ZT is decreased. Moreover, the *n*-type material $Re_3Ge_{0.6}As_{6.4}$ may constitute the ideal counterpart to the *p*-type $Mo_3Sb_{5.4}Te_{1.6}$. The thermoelectric properties of all the materials here at 300K are summarized in Table 1.

Table 1. Thermoelectric Properties Summary at 300K

| Composition | ρ(mΩ-cm) | α(μV/K) | κ($Wm^{-1}K^{-1}$) | P.F.( $Wm^{-1}K^{-1}$) | ZT |
|---|---|---|---|---|---|
| $Mo_3Sb_{5.4}Te_{1.6}$ | 0.56 | 49 | 4.4 | 0.13 | 0.029 |
| $Ni_{0.06}Mo_3Sb_{5.4}Te_{1.6}$ | 0.54 | 65 | 5.67 | 0.23 | 0.041 |
| $Nb_3Sb_2Te_5$ | 13.5 | -29 | 5.65 | 0.0018 | 0.0003 |
| $Re_3GeAs_6$ | 1.32 | -67 | 3.85 | 0.10 | 0.027 |
| $Re_3Ge_{0.6}As_{6.4}$ | 0.92 | -72 | 4.18 | 0.17 | 0.041 |
| $Co_{0.05}Re_3Ge_{0.4}As_{6.6}$ | 0.83 | -59 | 6.9 | 0.13 | 0.018 |

Table 2. The Summary of β, γ and Debey Temperature

| Composition | β($mJmol^{-1}K^{-4}$) | γ($mJmol^{-1}K^{-2}$) | $\theta_D$(K) |
|---|---|---|---|
| $Mo_3Sb_{5.4}Te_{1.6}$ | 0.65 | 15.0 | 311 |
| $Ni_{0.06}Mo_3Sb_{5.4}Te_{1.6}$ | 0.74 | 9.32 | 298 |
| $Nb_3Sb_2Te_5$ | 0.85 | 5.95 | 283 |
| $Re_3GeAs_6$ | 0.76 | 4.17 | 294 |
| $Re_3Ge_{0.6}As_{6.4}$ | 0.60 | 1.98 | 319 |
| $Co_{0.05}Re_3Ge_{0.4}As_{6.6}$ | 0.37 | 9.00 | 374 |

Table 3. The Summary of Hot-press

| Composition | Temperature (°C) | Pressure (ton) | Duration (hr) | Density ($g/cm^3$) | % of Theoretical Density |
|---|---|---|---|---|---|
| $Mo_3Sb_{5.4}Te_{1.6}$ | 720 | 1.8 | 1.0 | 8.54 | 96% |
| $Ni_{0.06}Mo_3Sb_{5.4}Te_{1.6}$ | 720 | 1.8 | 1.0 | 8.71 | 98% |
| $Nb_3Sb_2Te_5$ | 650 | 1.4 | 1.0 | 7.65 | 94% |
| $Re_3GeAs_6$ | 720 | 2.3 | 1.5 | 9.57 | 90% |
| $Re_3Ge_{0.6}As_{6.4}$ | 720 | 2.3 | 1.5 | 10.0 | 93% |
| $Co_{0.05}Re_3Ge_{0.4}As_{6.6}$ | 720 | 2.3 | 1.5 | 9.62 | 89% |

# APPENDIX

Table A.1. Crystallographic Data for $Mo_3Sb_7$ and $Mo_3Sb_5Te_2$

| Formula | a/pm | x(Mo) | x(Sb(2)) | Method | *R(F)* |
|---|---|---|---|---|---|
| $Mo_3Sb_7$ | 957.13(8) | 0.3425(13) | 0.1624(4) | Weissenberg | 0.094 |
| $Mo_3Sb_7$ | 955.9(3) | 0.3432(2) | 0.1620(8) | CCD | 0.033 |
| $Mo_3Sb_7$ | 956.1(1) | 0.3451(8) | 0.1633(3) | D500 | 0.055 |
| $Mo_3Sb_5Te_2$ | 956.3(1) | 0.3407(5) | 0.1634(2) | D500 | 0.037 |

Space group $Im\bar{3}m$, Mo on x, 0, 0; Sb(1) on ¼, 0, ½; Sb(2) on x, x, x.

Table A.2. Crystallographic Data for $Nb_3Sb_2Te_5$

| | |
|---|---|
| Empirical formula | $Nb_3Sb_5Te_2$ |
| Formula weight (g/mol) | 1160.23 |
| Temperature (K) | 298 |
| Wavelength (Å) | 0.71073 |
| Space group | *I*43-*m* |
| Cell dimensions, *a* (Å) | 9.8180(4) |
| *V* (Å$^3$) | 946.39(7) |
| Number of formula units per cell | 4 |
| Calculated density (g/cm$^3$) | 8.143 |
| Absorption Coefficient (mm$^{-1}$) | 24.189 |
| *F* (0 0 0) | 1940 |
| Crystal size (μm) | 25 × 21 × 20 |
| 2Theta range (°) | 5-70 |
| Reflections collected | 2376 |
| Independent reflections ($R_{int}$) | 367 (0.036) |
| Observed data (2σ), parameter | 332.15 |
| Absorption correction | Empirical |
| Minimum, maximum transmission | 0.52, 0.74 |
| Goodness-of-fit on $F^2$ | 1.101 |
| $R(F)$, $R_W(F^2)$ ($I$>2σ($I$)) | 0.025, 0.046 |
| $R(F)$, $R_W(F^2)$ (all data) | 0.029, 0.048 |
| Extinction coefficient | 0.00072(5) |
| Maximum diffraction peak, hole (e/ Å$^3$) | +1.28, -1.24 |

Table A.3. Atomic Positions and Displacement Parameters of $Nb_3Sb_2Te_5$

| Atom | Site | $x$ | $y$ | $Z$ | $U_{eq}$ (Å$^2$) |
|---|---|---|---|---|---|
| Nb | 12e | 0.34267(9) | 0 | 0 | 0.0046(2) |
| Te1 | 12d | 1/4 | 1/2 | 0 | 0.0060(2) |
| Te2 | 8c | 0.16615(9) | 0.16615(9) | 0.16615(9) | 0.0058(4) |
| Sb2 | 8c | 0.83657(11) | 0.83657(11) | 0.83657(11) | 0.0070(4) |

Table A.4. Crystallographic Data for $Re_3GeAs_6$

| | | |
|---|---|---|
| Empirical formula | | $Re_3GeAs_6$ |
| Formula weight [g/mol] | | 1080.75 |
| Temperature [K] | | 298 |
| Wavelength [Å] | | 1.3302 |
| Space group | | $Im\bar{3}m$ |
| Cell dimensions, | $a$ [Å] | 8.73180(7) |
| | $V$ [Å$^3$] | 665.75(2) |
| No. of formula units per cell | | 4 |
| Calculated density [g/cm$^3$] | | 10.78 |
| 2theta range [°] | | 4.9 – 115.1 |
| $R_P$, $R_{wP}$ | | 0.0358, 0.0482 |

Table A.5. Atomic Positions and Displacement Parameters of $Re_3GeAs_6$.

| Atom | site | *x* | *y* | *z* | $U_{eq}/Å^2$ | occupancy |
|---|---|---|---|---|---|---|
| Re | 12e | 0.3413(2) | 0 | 0 | 0.0017(3) | 1 Re |
| As1 | 12d | ¼ | 0 | ½ | 0.0054(5) | 1 As |
| E2 | 16f | 0.1663(2) | 0.1663(2) | 0.1663(2) | 0.0073(4) | 0.25 Ge, 0.75 As |

REFERENCES

1 Thermoelectrics.com, http://www.thermoelectrics.com/introduction.htm.

2 Seebeck, T.J., 1822, *Magnetische Polarisation der Metalle und Erzedurch Temperatur-Differenz.* Abhand Deut. Akad. Wiss. Berlin, 265-373.

3 D.M. Rowe, Thermoelectrics Handbook:macro to nano. Page **1**-2

4 Peltier, J.C., *1834, Nouvelles experiences sur la caloriecete des courans electriques.* Ann. Chem., LVI, 371-387.

5 Thomson, W., *1851, On a mechanical theory of thermoelectric currents,* Proc.Roy.Soc.Edinburgh, 91-98.

6 D.M. Rowe, *Thermoelectrics Handbook:macro to nano.* Page **1**-3

7 D.M. Rowe, *Thermoelectrics Handbook:macro to nano.* Page from **1**-3 to **1**-4

8 D.M. Rowe, *Thermoelectrics Handbook:macro to nano.* Page from **1**-4 to **1**-7

9 D.M. Rowe, *Thermoelectrics Handbook:macro to nano.* Page from **1**-7 to **1**-8

10 E. Dashjav, A. Szczepenowska, H. Kleinke, *J. Mater. Chem.*, 2002, 12, 345-349.

11 E. Dashjav, H. Kleinke, *Mat. Res. Soc. Symp.* Proc. Vol. 793. Page 149-154.

12 N. Soheilnia, A. Assoud, H. Zhang, T. M. Tritt, I. Swainson, H. Kleinke, *Chem. Mater.* , in press

13 N. Soheilnia, J. Giraldi, A. Assoud, H. Zhang, T. M. Tritt, H. Kleinke, *J. Alloys and Compd. (2006)*.

14 A. L. Pope, R. T. Littleton IV, T. M. Tritt, *Rev. Sci. Instrum*. 72 (2001) 3129-3131.

15 *Model ZEM-2 Seebeck Coefficient Measuring SystemInstruction Manual*

16 *Physical Properties Measurement System: AC Transport Option User's Manual. San Diego: Qu antum Design (1998).*

17 A. L. Pope, B. Zawilski, T. M. Tritt, *Cryogenics 41 (2001) 725-731.*

18 S. O. Kasap, *Electrical and Thermal Conduction in Solids*

19 *Operating Instructions Micro-Flash-Apparatus LFA 457.*

20 *Basics of the Methods of Thermal Analysis.*

21 J. Electron. Mater., in press.

22 Solid State Physics, Neil W. Ashcroft/*N. David Mermin, Cornell University.*